An Open-well Organs-on-chips Device for Engineering the Blood-Brain-Barrier

by

Wei Liao

Bachelor of Engineering, Tsinghua University (2018)

Submitted to the
Department of Electrical Engineering and Computer Science
in partial fulfillment of the requirements for the degree of

Master of Science

at the

MASSACHUSETTS INSTITUTE OF TECHNOLOGY

September 2020

Author . . . .
Wei Liao
Department of Electrical Engineering and Computer Science
August 28, 2020

Certified by. . . . .
Joel Voldman
Professor of Electrical Engineering and Computer Science
Thesis Supervisor

Accepted by . . . .
Leslie A. Kolodziejski
Professor of Electrical Engineering and Computer Science
Chair, Department Committee on Graduate Students

An Open-well Organs-on-chips Device for Engineering the Blood-Brain-Barrier

by

Wei Liao

Submitted to the
Department of Electrical Engineering and Computer Science
on August 28, 2020, in partial fulfillment of the
requirements for the degree of
Master of Science

Abstract

Microfluidic Organs-on-chips (OOC) technology hold great promise for advancing the understanding of blood-brain-barrier (BBB) physiology and investigating BBB dysfunction in central nervous system diseases. It can provide high physiological relevance through engineering a range of system parameters. However, the resulting system can be hard to operate, have inadequate robustness and limited throughput, which is a major challenge that must be overcome before its widespread acceptance by both basic and applied research area.

This thesis proposed a system which is aimed at solving this particular challenge of microfluidic OOC systems by having the open-well design to ease the process of liquid handling and allows facile assay while maintaining the high biological sophistication it can model for the BBB (microarchitecture, vascular perfusion etc.). A simulation model was developed to optimize the device design and predict the distribution of one vital chemical stimulating signal for vasculogenesis—Vascular Endothelial Growth Factor (VEGF), where distinctive isoform-specific transport profiles were found due to the binding reaction with the extracellular matrix (ECM). Experimental validation was performed to examine the ECM-binding capability for a specific isoform, which yielded consistent results with the simulation.

Next, preliminary experiments for the proposed system were conducted, which include the vasculogenesis assay using brain endothelial cells derived from induced pluripotent stem cells (iPSCs) and the APTES-mediated polystyrene-PDMS bonding. These two aspects are integral for the next-stage development of the proposed system and the implementation of a multicellular BBB model on this platform. It is anticipated that the proposed system will realize facile, robust and high-throughput assays thus wider adoption in biology research area.

Thesis Supervisor: Joel Voldman
Title: Professor of Electrical Engineering and Computer Science

Acknowledgments

I would like to express my deepest gratitude to my thesis supervisor Prof. Joel Voldman, for his continuous support, invaluable advising, professional insight throughout my master studies.

My appreciation also extends to all my past teachers and advisors who imparted me knowledge and provided me with broadminded academic guidance and exciting inspirations, which lead me to where I am now.

I am grateful to all members in the Voldman Lab, not only for their expert instructions in the lab, but also for their kind encouragement and help in many aspects of my life.

I would like to express my sincere gratitude to all my friends, who are my listeners and also my role models. I cherish every moment spent with you.

Nobody has been more important to me in the pursuit of my graduate studies than my parents, who are always supportive for my decisions and always available to me no matter how far we are physically apart from each other.

Contents

List of Figures

List of Tables

Chapter 1

Introduction

Microfluidic organs-on-chips (OOC) systems have been used to model the blood-brain-barrier (BBB) and these systems have started to manifest physiological or pathological properties akin to *in vivo* findings [1, 2]. Taking the next step of investigating pathological mechanisms and pinpointing causal cell types in complex tissues will require reproducible, biologically relevant models with sufficient throughput to iterate across many experimental conditions while minimizing experimental complexity at the same time. Importantly, careful examination of the physical behavior and biochemical interactions in the OOC system through simulation and experimental validation are an integral process for reevaluating the device design, optimizing experiment protocol and achieving unbiased experimental outcome. In this chapter, we will first discuss the existing compelling research work in the microfluidic OOC field as well as its applications for modeling the BBB. Then we will introduce our proposed system which is intended for solving one main challenge in this area. An overview of this thesis is presented at the end of this chapter.

1.1 Microfluidic Organs-on-Chips Systems

Understanding human physiology and pathophysiology requires investigation of how living cells and tissues function, how they interact with its microenvironment (other cells/tissues, mechanical forces, chemical signals, extracellular matrix etc.) and how

they generate organ-level functions. Conventional static 2D and 3D culture often fail to reproduce the dynamic 3D microenvironment and this limitation provides an impetus for the development of *in vitro* models which integrate the technology from both microengineering and tissue engineering to generate microengineered physiological models, also known as organs-on-chips (OOC). Microfluidic OOC systems use microfabrication techniques to construct organ-specific cell culture microenvironment, which facilitates the study of a broad array of physiological phenomena.

Reconstituting relevant chemical and mechanical microenvironment in such OOC systems has proved to be enormously beneficial in mimicking *in vivo* conditions and recapitulating organ normal functions. Esch et al. [3] reported a liver-on-a-chip model comprised of primary liver cell cultures that increased their metabolic activity in response to fluid flow. In a human kidney proximal tubule-on-a-chip model [4], exposure of the epithelial monolayer to fluid shear stress resulted in enhanced epithelial cell polarization and primary cilia formation. In addition to the flow-induced shear stress, cells and tissues in the human body continuously experience organ-specific tensile and compression forces. A human gut-on-a-chip [5] model applied both a low shear stress and a cyclic strain to the human intestinal epithelial cells to mimic its microenvironment and the resulting epithelium formed a high integrity barrier to small molecules which better mimicked the intestine than cells in static transwell models. Critical chemical signals can also be delivered in OOC systems to improve organ-specific functions, study molecular transport across barriers and investigate drug efficacy or perform toxicity testing. For instance, a BBB chip has been used to assess the capability of a peptide to transport a cargo across the BBB and they found that decoration with the peptide enhanced the adhesion of nanoparticles to the endothelial layer and the BBB crossing under flow conditions, which indicated the possible efficacy of the peptide as a delivery platform to the brain [6]. Shin et al. [7] applied a precisely orchestrated gradient of soluble angiogenic factors, VEGF and ANG-1, and investigated both the chemotactic response of tip cells attracted by the VEGF gradient and the stabilizing role of ANG-1 (Figure 1-1C). There are a broad range of applications that OOC systems are enabling, while in the traditional 2D/3D

culture assays, a dynamic and precisely-controlled chemical or chemical gradient is usually hard to realize [8].
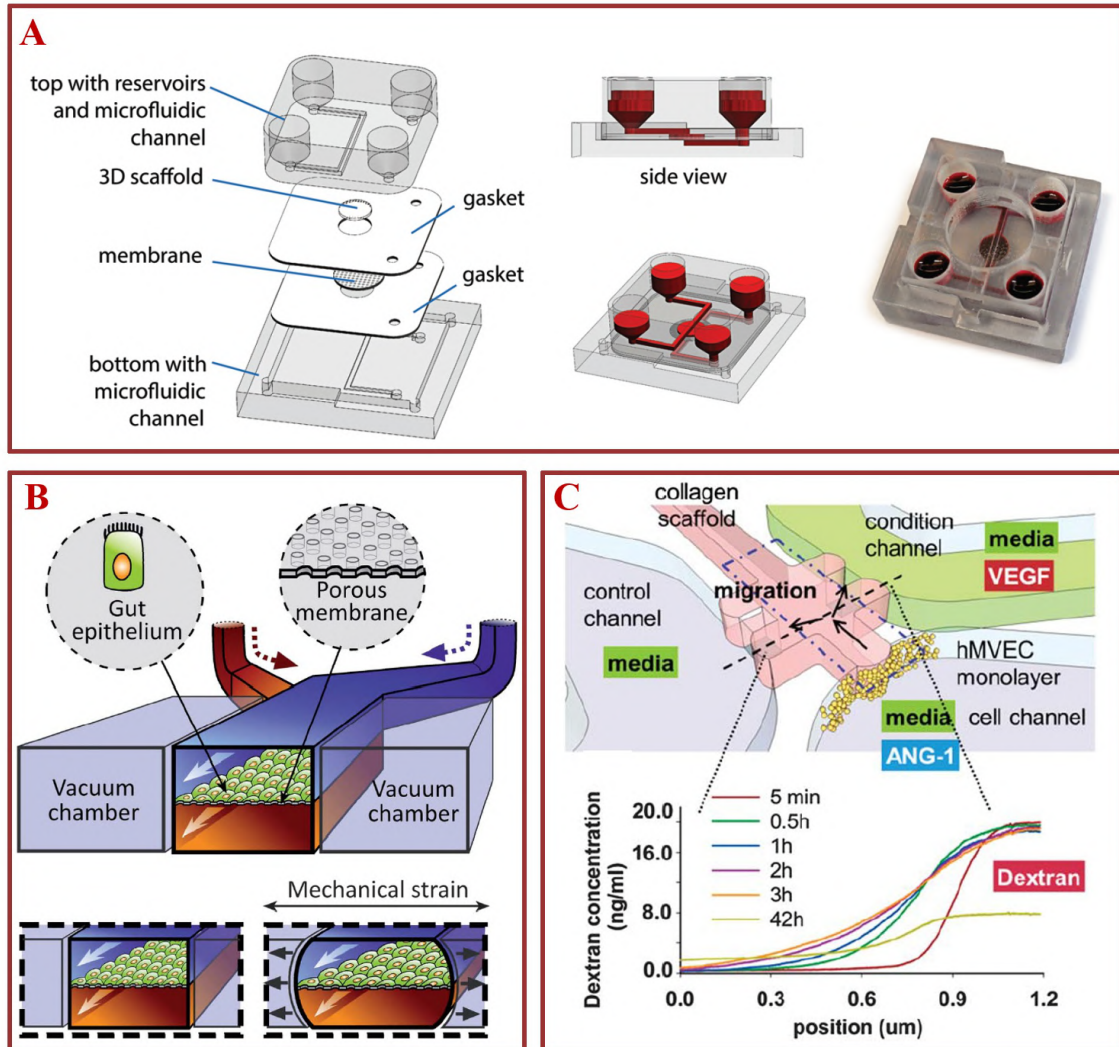
Figure 1-1: Reconstitute relevant chemical and mechanical microenvironment in different OOC systems. A) Gravity-driven flow is enabled in a primary liver cell culture platform and elevated metabolic activity under flow condition was observed. Reproduced with permission from [3]. B) Cyclic strain can be applied via suction to the vacuum chambers thus providing physiologically-relevant mechanical cues. Reproduced with permission from [5]. C) A platform used to provide orchestrated gradient of soluble angiogenic factors and to study angiogenesis. Reproduced with permission from [7].
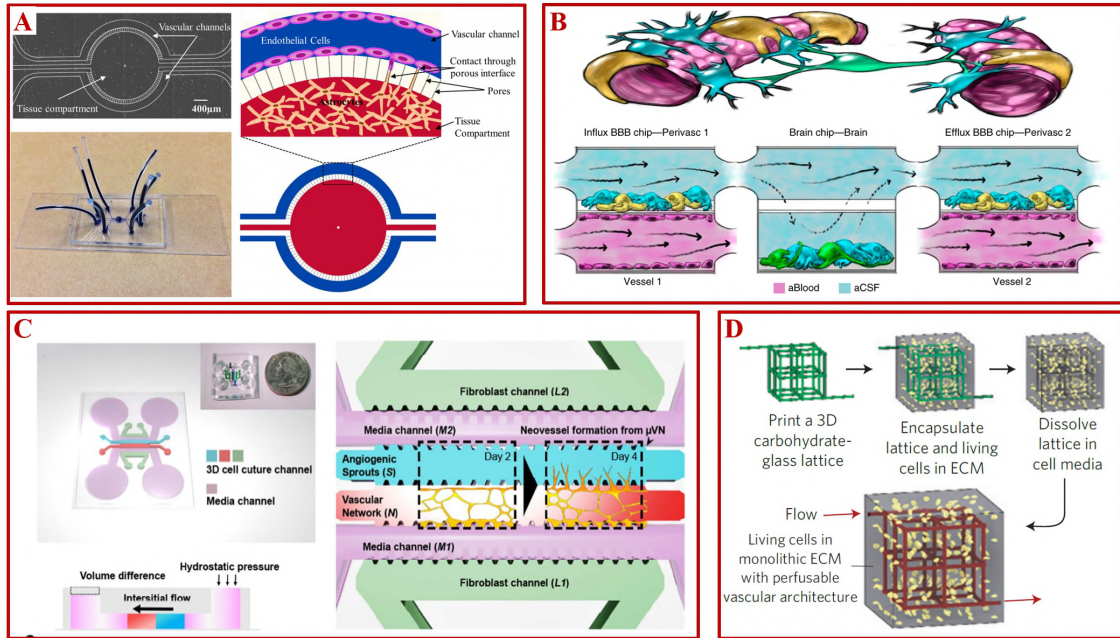
Figure 1-2: Various ways to control cell patterning in OOC systems. A) The center tissue compartment containing astrocytes is surrounded by 2 independent vascular channels with flow access openings. A series of porous interface facilitates the cellular communications between 2 compartments. Reproduced with permission from [9]. B) Top and bottom channels are seperated by a polycarbonate membrane and 3 coupled chips are designed to model the influx across BBB, the brain parenchymal compartment and the efflux across the BBB by designing specific cellullar locations and fluidic coupling. Reproduced with permission from [1]. C) An widely used device format to form 3D microvascular networks. Reproduced with permission from [10]. D) An interconnected carbohydrate-glass lattice was printed and later sacrificed after encaptulated in ECM. Reproduced with permission from [11].

The ability to control cell patterning in OOC systems is another favorable feature. Different cell types can be plated in neighboring channels/compartments on the same planar substrate with custom-designed microstructures facilitating cell-cell communication [9, 12]. Porous membranes are often integrated to separate two parallel microchannels with two different cell types adhering on opposite sides (Figure 1-2B). This format has been used to successfully construct the minimal function unit of human lung [13], gut [5] and kidney proximal tubule [4] and BBB [1] on a chip. Besides, cells can be pre-encapsulated in the 3D ECM gel and then injected into the chip, where the relatively low stiffness of the environment is closer to that of the real tissues and the cells are free to self-organize in 3D and generate the apical-

basal polarity on their own [10, 14]. Technical advances in material science have also brought numerous innovative ways to define cell spatial location. For instance, a bio-compatible carbohydrate glass lattice can be 3D-printed and then be encapsulated in cell-laded ECM (Figure 1-2D). The lattice would eventually be dissolved to generate desirable network geometry for endothelialization and perfusion [11].
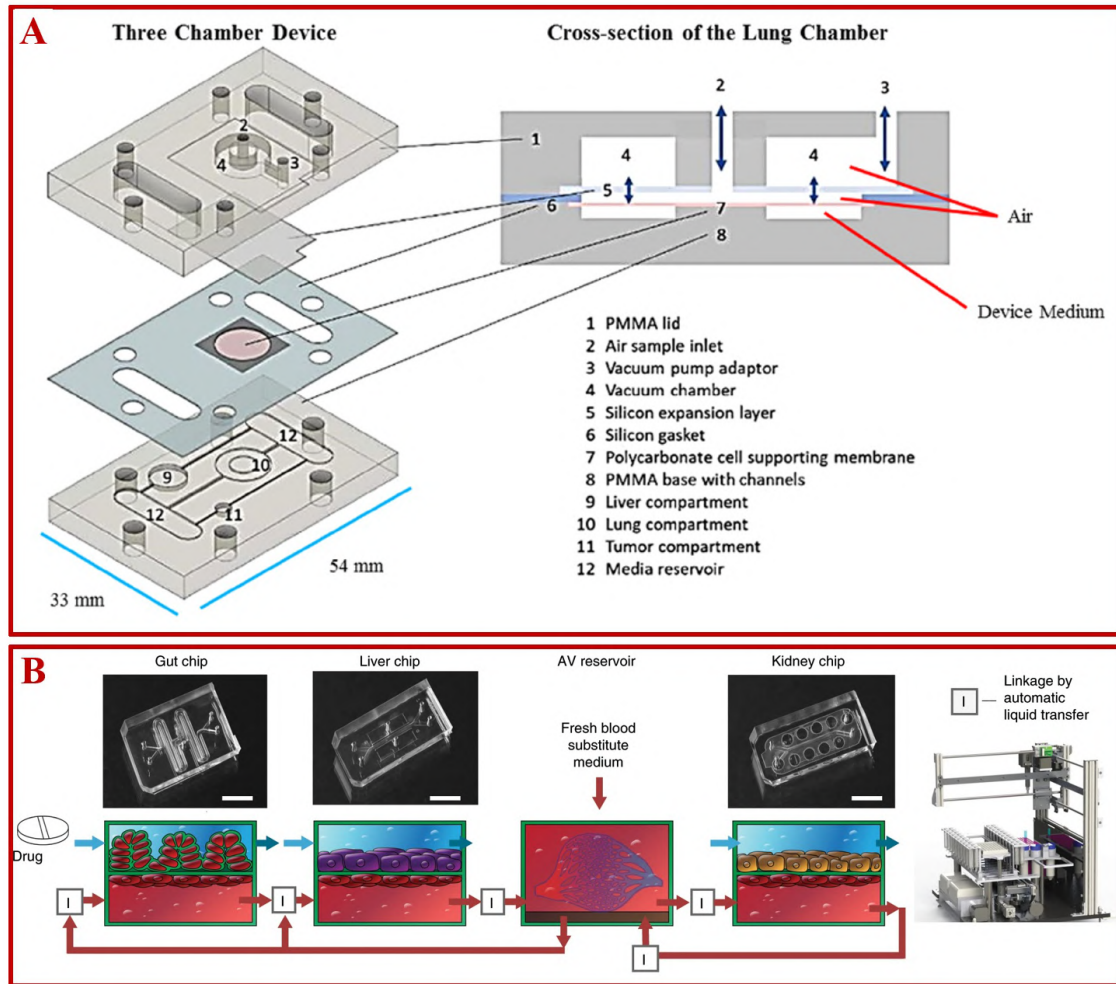
Figure 1-3: Multi-organ OOC systems. A) A multiorgan microfluidic device with liver, lung, and tumor compartment. Gravity-driven bidirectional flow was maintained to perfuse each compartment. The air sample inlet (2) was used to model inhalation therapy. Reproduced with permission from [15]. B) A multiorgan chips consisting of gut, liver and kidney chips. A specific fluid linking scheme was designed to link these organ chips and the AV reservoir. Reproduced with permission from [16].

There have also been tremendous efforts in integrating multiple organ chips in one platform as many biological questions involve coordinated function of different

organs. A multiorgan microphysiological system including lung, liver, and breast cancer models was designed to compare the cytotoxic effects of curcumin via different delivery methods—inhalation versus intravenous administration under recirculating flow [15]. Inhalation method was modeled via delivering drugs to the lung chamber while intravenous administration was mimicked through the media reservoir (Figure 1-3A). Another multiple two-channel human organ chips were fluidically coupled by transferring a universal blood substitute between endothelium-lined vascular channels using a robotic interrogator (Figure 1-3B) [16, 17]. This model has predicted quantitative human PK parameters of nicotine and cisplatin *in vitro* that are highly similar to those obtained in human clinical studies. All these pioneering works indicate that OOC systems could be of great value for the pharmaceutical industries and biotechnology.

The biological complexity it can model through various engineering innovation is truly impressive and promising. However, high biological complexity is commonly associated with complex operation, inadequate robustness and reproducibility, and limited throughput. This is understandable giving that the initial focus of these OOC systems is primarily to demonstrate the physiological characteristics and the predictive value of the OOC systems. To enable the adoption of OOC systems by a wider research community such as pharmaceuticals and biology, high throughput experimentation is an essential feature besides a high physiological relevance [18]. A small number of OOC systems have already been taken to the next level in terms of parallelization to increase the number of replicates per chip. For instance, OrganoPlate ® provides a 96 two-lane system on a 384-well plate for individual loading of cell-laden hydrogels and has been used in a brain-on-chip model to evaluate the neurotoxicity of organophosphates [19] and a glomerulus-on-a-chip to recapitulate the human glomerular filtration barrier [20]. Phan et al. [21] have demonstrated a platform capable of culturing 12 independent vascularized micro-organs on a 96-well plate with flow driven by hydrostatic pressure, thus eliminating the requirement for external pumps or valves (Figure 1-4B). Another 96-element microfluidic array (PREDICT-96) has been equipped with a re-circulating pumping system to realized long-term (10 days)

22

perfused culture of primary human hepatocyte and to capture cellular responses to chronic stimuli [22]. However, among these systems, new questions can be raised such as the difficulty in imaging, the compatibility with the 3D culture method, the low throughout manner of cell loading, the constant changing perfusion direction etc.
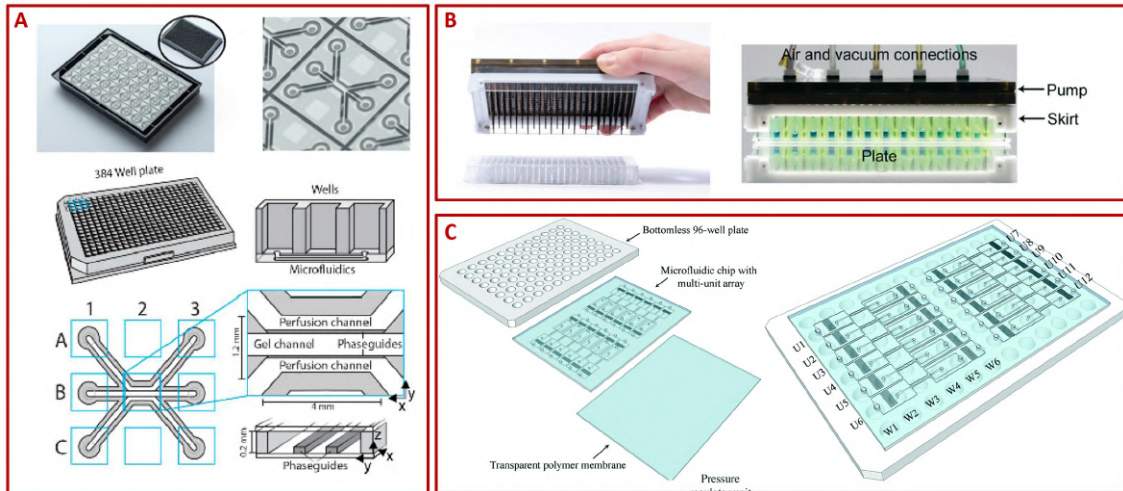
Figure 1-4: Existing high throughput OOC platforms. A) The OrganoPlate can either provide 48 three-lane systems or 96 two-lane systems (not shown). Image Reproduced with permission from [23]. B) The Predict-96 platform can realize long term primary human hepatocyte culture with a lid capable of recirculating flow. Reproduced with permission [22]. C) 12 independent vascularized micro-organs on a 96-well plate with flow driven by hydrostatic pressure. Reproduced with permission from [21].

In addition, OOC systems that incorporate ideas from open microfluidics have been gaining traction. Open microfluidics provides improved accessibility (due to the partially open layout) [24] and ease of fabrication (due to the elimination of the irreversible bonding step) [25]. Open microfluidics typically doesn't require external tubings or pumps. External tubings or pumps can hinder the realization of high throughput assays as they are labor-intensive elements in microfluidic assays and they can often cause failures due to bubble introduction in the devices [26]. Therefore, the resulting open microfluidic systems usually facilitate high-throughput experimentation and allow for ease-of-use operation [27, 28]. However, these systems does not provide enough physiological features for modeling sophisticated tissues/organs which require other critical features such as vascular perfusion (Figure 1-5).

Despite the fact that there is a myriad of evolving OOC systems with either
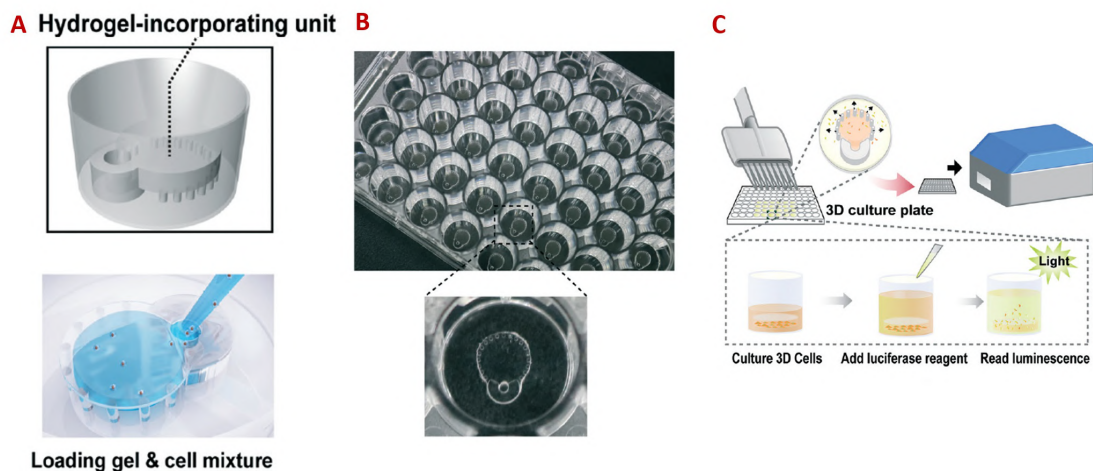
Figure 1-5: An open-well system for high-throughput analysis. A) One single hydrogel incorporating unit utilizing a 48 wellplate and its gel loading strategy.The gel could be pinned at the post-array structure. B) Multiple units can be assembled in the 48 wellplate. C) High-throughput biochemical assays can be realized using this platform. Reproduced with permission form [27].

optimized functionality, increased throughput or enhanced end-point analysis, the development of a system that allows for ease-of-use, reasonable throughput and facile assay while maintaining biological sophistication and high model tractability at the same time is still a challenging task.

1.2   Organ-on-Chips Platforms for Modeling the Blood Brain Barrier

Globally, in 2016, neurological disorders were the second leading cause of death (9.0 million) [29] while therapeutic options for neurological disorders currently remain limited. New FDA-approved drugs for neurological disorders has barely exceeded 2 per decade in the last 50 years [30]. One of the biggest challenges in the development of therapeutics for central nervous system (CNS) disorders is to achieve sufficient blood–brain barrier (BBB) penetration [31]. BBB is a microvessel network in the human CNS. Anatomically, it is comprised of a single layer of nonfenestrated endothelial cells separating the blood from the brain extracellular fluid. The abluminal

surface of the endothelial cells are surrounded by the basement membrane, pericytes, and astrocyte endfeet as shown in Figure 1-6A [32]. Functionally, it tightly regulates the exchange of substances between the CNS and the blood and It is a complex, dynamic, adaptable interface controlling and responding to pathological conditions, and participates the onset, maintenance or progression of many CNS diseases [31]. For instance, it was reported that individuals with early cognitive dysfunction develop brain capillary damage and BBB breakdown in the hippocampus irrespective of $A\beta$ and/or tau biomarker changes [33], which is the prime suspect of Alzheimer's disease pathogenesis [34].

Owing to its complex structure and unique role in regulating brain homeostasis, it is of vital importance to establish suitable BBB models which can provide in-depth understanding of the BBB function, predict the permeability of promising therapeutics, and gain insight of the relationship between BBB dysfunction and CNS disease. Although animal models are the gold standard, the lack of translation between animal models and human studies due to cross-species difference [35] has been reported and human-origin cell models have the promising perspective to bridge the gap between preclinical predictions based on animal studies and the actual outcomes of clinical trials [36]. This has resulted in the development of more human-centric approaches like *in vitro* human cell-derived assays.

The maintenance of BBB function requires constant interaction with its microenvironment, which includes the basement membrane, pericytes, and astrocyte end-feet [32]. Transwell BBB models are able to realize tri-culture of brain EC, astrocytes and pericytes and establish proper cellular communication [38] through carefully arranging cell positions relative to the permeable membrane of the insert (Figure 1-6B). Nonetheless, transwell assays suffer from a major drawback—lack of physiological relevance. Microfluidic OOC systems can provide a highly controlled cellular microenvironment and can be engineered to possess various critical physiological features depending on the problem under investigation. For instance, shear stress can be applied to the cells through fluid flow and abundant research reports have found that shear stress is conducive to a 3x to 20x higher transendothelial electrical resis-
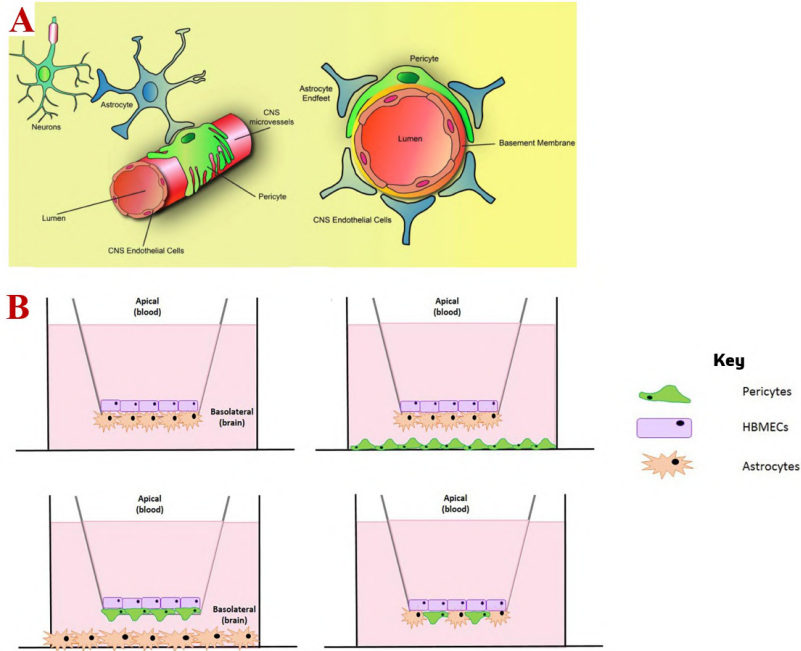
Figure 1-6: A) BBB microstructure *in vivo*. The BBB is comprised of a single layer of nonfenestrated endothelial cells with the aluminal surface of the CNS endothelial cells surrounded by the basement membrane, pericytes, and astrocyte endfeet. Reproduced with permission from [32]. B) Transwell cell culture strategies to model the BBB. Reproduced with permission from [37].

tance (TEER) compared with the static culture [39, 40, 41]. TEER is a quantitative technique to measure the electrical impedance in *in vitro* endothelial and epithelial culture models. The electrical impedance obtained is an assessment of both transcellular resistance (due to cellular membrane) and paracellular resistance (due to cell-cell contact) [42]. Therefore, high TEER value indicates a high paracellular resistance, which further represents a high level of tight junction integrity. At the BBB, specialized tight junction complexes between endothelial cells prevent paracellular flux, which is believed to be one of the fundamental barrier properties that contribute to BBB function and integrity [32].
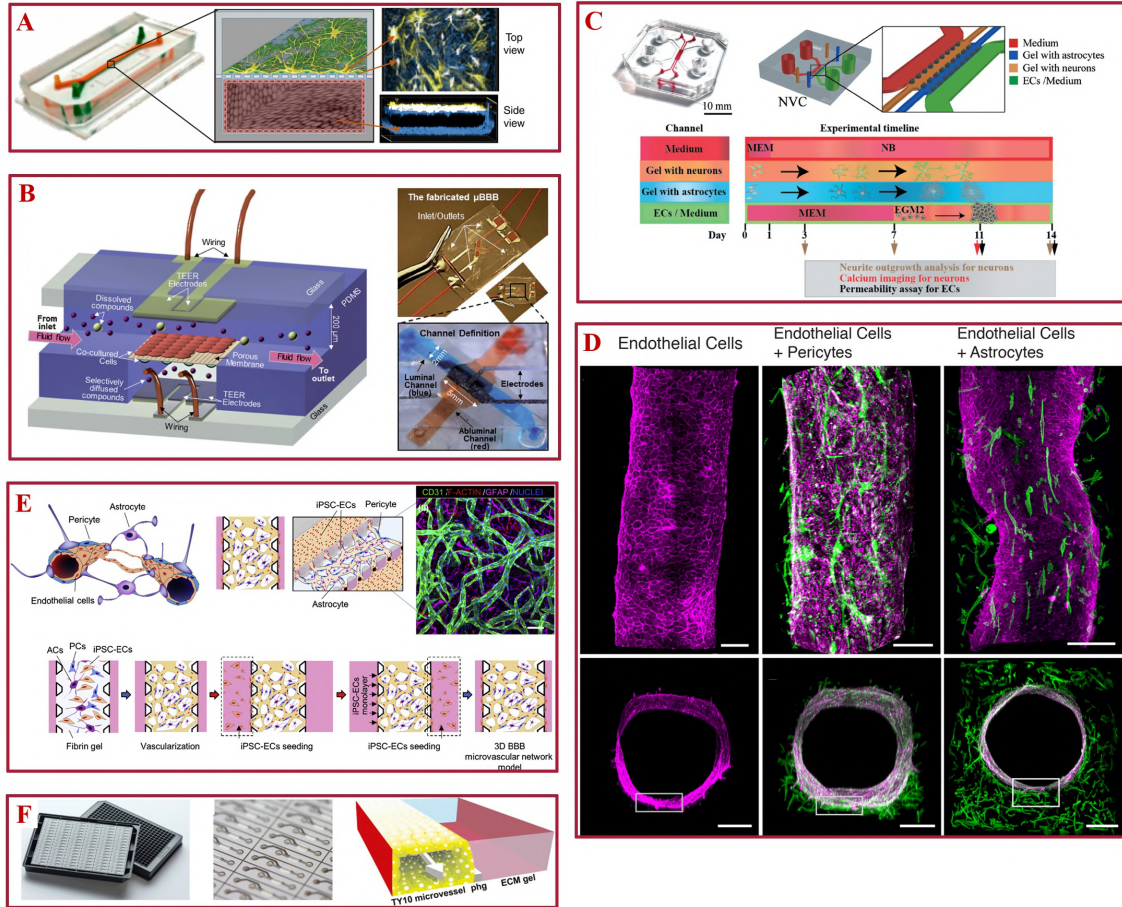
Figure 1-7: A variety of existing OOC models for the BBB. A) A 2-channel microfluidic organ chip with iPS-BMVECs cultured on all surfaces of the basal vascular channel, and primary human brain astrocytes and pericytes on the upper surface of the central horizontal membrane, Which was coated on both sides with collagen type IV and fibronectin. Image reproduced with permission from [43]. B) Shear stress can be applied to the endothelial monolayer in the OOC system to allow dynamic microenvironment and improved analysis of test compounds and controlled delivery compared to static models. Image reproduced with permission from [44]. C) Precise cellular spatial location defined by microfluidic channels. Two central hydrogel regions for co-culturing astrocytes (blue) and neurons (orange) and two side channels for hosting endothelial cells and media (green and red, respectively). Image reproduced with permission from [45]. D) A cylindrical hollow structure can be created for endothelial cells lining. The surrounding gel can be embedded with astrocytes or lined with pericytes on the surface. The microstructure created in this model resembles *in vivo* organizations. Image reproduced with permission from [46]. E) A BBB model created using iPSC-ECs, pericytes and astrocytes in a 3D gel environment. EC self-assembled into microvascular network. Image reproduced with permission from [47]. F) The two-lane OrganoPlate® which is consist of 96 tissue culture chips. ECM gel is added to the gel channel and a phaseguide prevents it from flowing into the adjacent microvessel channel. The microvessel lined by TY10 cells has a lumen that is perfused. Image reproduced with permission from [48].

Although 2D cell co-culture is a popular approach [40, 43, 44], physiological 3D spatial arrangement of BBB cell types has also been engineered in OOC systems [45, 47, 49]. Herland et al. [46] demonstrated a strategy to create a cylindrical collagen gel containing a central hollow lumen inside a microchannel, which could be further lined by primary microvascular endothelial cells to closely mimic the cellular microarchitecture *in vivo* (Figure 1-7D). Furthermore, the innate property of mature cells to self-assemble into complex 3D tissues have been widely exploited by pre-embedding BBB cells in a suitable 3D ECM scaffold. BBB models utilizing this strategy have exhibited 3D perfusable and selective microvasculature (Figure 1-7E), with permeability similar to *in vivo* measurements in the rat brain [47].

Moving beyond focusing solely on physiological engineering of the platform, BBB models have also started to manifest pathological properties akin to *in vivo* findings or even reveal novel discoveries. Shin et al. [2] demonstrated a physiologically relevant 3D human neural cell culture microfluidic model and recapitulated several key aspects of BBB dysfunction observed in patients with Alzheimer's disease including deposition of amyloid-β peptides at the vascular endothelium. Maoz et al. [1] identified previously unknown metabolic coupling between the BBB and neurons using three fluidically linked microfluidic chips to model the influx across the BBB, the brain parenchymal compartment and the efflux across the BBB. All these emerging techniques and platforms manifest the amazing potential of the OOC chips in elucidating mechanisms underlying the role of BBB in disease and uncovering new therapeutic opportunities for mitigating neurodegeneration.

The initial focus of these BBB models is primarily functionality, which is certainly an important and necessary step in the advancement of this field. However, the resulting systems can be complicated to operate even for one or a few culture units, which further hinders the development of a high throughput platform. Only a small number of research works have realized high throughput BBB-on-a-chip models. For instance, Wevers et al. [48] have developed a perfused human BBB-on-a-chip in a high-throughput manner in a high-throughput manner using the OrganoPlate ® (Figure 1-7F). However, there is still lacking flexibility to assay the tissue culture.

28

Many of these challenges arise from the same cause: chips are comprised of many enclosed layers [15] and/or are connected to external support systems via bubble-prone tubings [1], making it technically challenging to instantiate, maintain and assay the (typically gel-laden) OOC. Therefore, besides incorporating essential physiological features such 3D co-culture, vasculature perfusion, a microfluidic BBB model that can incorporate diverse variations and sufficient throughput in experimental conditions (e.g. cell types/ratios, genotypes, chemical treatment dose/duration) and provides easy operation and ready access to cells to deeply phenotype the model is still a challenging work.

1.3 Proposed System

The proposed device is aimed at solving the current challenges mentioned in the previous sections. It will provide the necessary biological model sophistication, reasonable experimental throughput while minimizing the operational complexity. It can also enable ready access to the cell and tissue being cultured on the platform. Specifically, the platform has several characteristics which will be introduced below.

First of all, it conforms to a microtiter plate format with cell-laden gels loaded directly from the open top (Figure 1-8C), which eases the process of liquid handling (such as for gel/cell addition to instantiate the model). We also designed a resealable lid allows sealing of the system (Figure 1-8F) and access to cells for assay such as microscopy, flow cytometry, sequencing, etc.). Efforts at incorporating open-well designs into microfluidics have been previously introduced to make microfluidic systems compatible with automatic pipetting or liquid dispensing equipment [26]. However, most of prior systems fall short of integrating the full capability of microfluidic OOC systems and lack a critical feature—media perfusion [24, 27, 50]. When media perfusion is designed via an micropump lid, the phase contrast imaging capability could be compromised [22]. However, phase contrast imaging is an indispensable feature in our proposed system to assess the cell states (Figure 1-8D).

Secondly, each unit has two perfusion channels that can operate at different flow
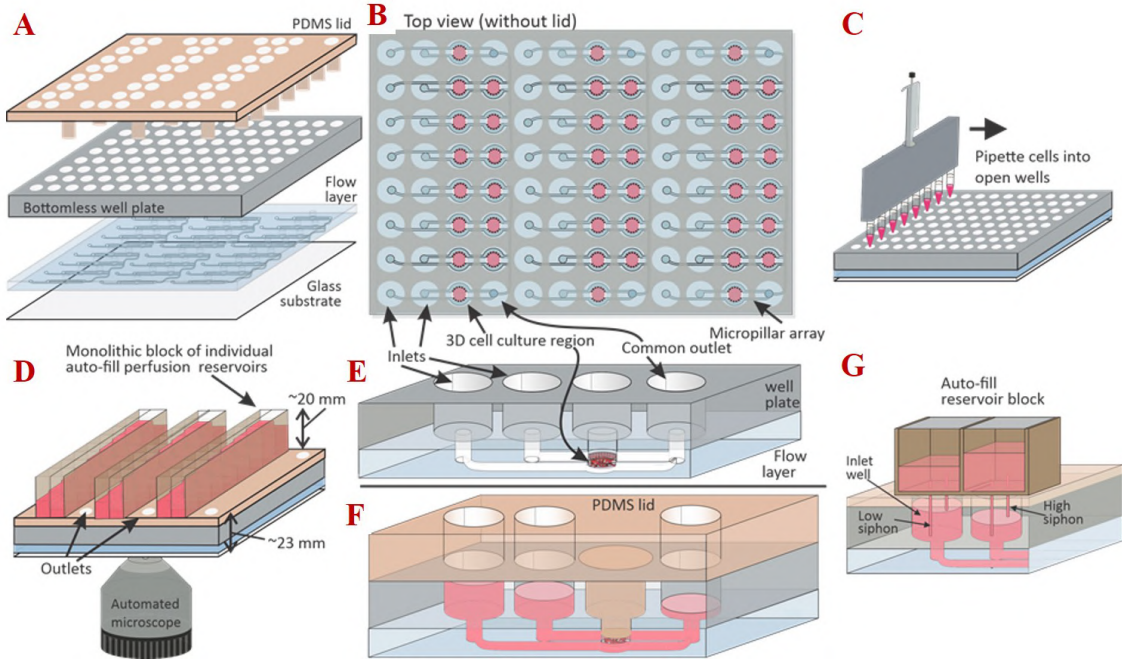
Figure 1-8: Schematic of the proposed system. A) Bottom 4 layers of device (reservoir block not shown). B) Top-view schematic of the device, showing 24 units with 96 chambers, of which 42 are cell culture regions, 48 are individually controllable perfusion inlets, 6 are common outlets). C) Open top allows easy introduction of cell-laden gel media, as well as access to cells for assay. D) After PDMS lid is applied, the three media reservoir blocks for refilling are placed on top. E) Closeup of two layers after cell loading. F) Closeup of 3 layers after lid attachment. G) Auto-fill reservoir block. When media in the inlet well drops below the high siphon, the media will be automatically refilled until it reaches the high siphon. This process will repeat itself to maintain the liquid level in each inlet well.

rates, thus enabling physiological interstitial flow in the 3D culture region (Figure 1-8E). Flow is driven by a hydrostatic pressure difference between the inlets and outlets to eliminate the use of bubble-prone tubing connections and pumps, which is a major failure mode that leads to reduced robustness reproducibility. Gravity-driven flow has been demonstrated in a variety of OOC systems [23, 51, 52].]. It is friendly to non-expert users as compared to other on-chip or off-chip pumping techniques that require extra instrumentation and/or tubing. We address the main limitation of gravity-driven flow—non-constant perfusion rates—by adopting the idea of a siphon-based auto-filling system [53] developed earlier (Figure 1-8G).

Finally, the key challenge is to introduce these simplifications while maintaining

the desired biological model microarchitecture and vascular perfusion. We will establish a BBB model using this device, incorporating iPSC-derived endothelial cells, astrocytes, pericytes (kindly provided by the Tsai Lab from MIT Department of Brain and Cognitive Science). We make use of the innate property of mature cells to self-assemble into complex 3D tissues and initiate physiological capillary flow in our multicellular BBB model. We will demonstrate our BBB model is highly reproducible and can be advanced further in terms of model sophistication to recapitulate diverse cellular interactions in human nervous system.

Careful design of the system parameters is a prerequisite to realize the designed function. Such parameters include the channel dimensions of the device. For instance, we want the perfusion channel to provide a physiological shear stress as observed in human arterial system. We also need to have physiological interstitial flow across both culture units on the same branch. In addition, the dimension of the 3D cell culture region is not only limited by the size of a single well from the microtiter plate, it's also restricted by the chemical profile we want to achieve (Imagine a case where we are applying certain chemical cue in the perfusion channels and try to establish a chemical gradient within several hours). All these need detailed characterization so we took finite element analysis as the first step moving towards the proposed system.

1.4   Thesis Overview

In order to pursue developing an open-well organs-on-chips device for engineering the blood-brain-barrier, the main objectives of this thesis are:

1. Analyzing important physical parameters to optimize the device dimension design. Evaluating possible biochemical reactions in the proposed system. (Chapter 2).

2. Experimental validation of the key aspect from the modeling work (Chapter 3).

3. Initial vasculogenesis study in a traditional enclosed microfluidic platform and device fabrication study for the proposed open-well system (Chapter 4).

The main conclusions, contributions and future prospects of this thesis work will be provided in Chapter 5.

Chapter 2

Finite Element Analysis of the Proposed System

2.1 Introduction

Microfluidic Organ-on-Chips can provide control over many system parameters that are not easily controlled in 3D static cultures, such as fluid flow, cell patterning, mechanical stress, etc. Better micro-engineering of these system parameters improves OOC function [8]. In our proposed device, one key step is to embed the cell/tissue in proper ECM as ECM is known to play an important role in numerous decisions that direct cell fate and behavior including cell maintenance, proliferation, migration and differentiation [54]. Another key parameter is to provide a gradient of Vascular Endothelial Growth Factor (VEGF) as VEGF gradient is a key sprouting-promoting signal [55]. In this chapter, we will model possible interactions between VEGF and the matrix as well as other important biochemical/biophysical factors that will affect the VEGF distribution in our system.

2.1.1 Finite element modeling

To properly design the channel dimensions for our proposed device, we need to have a comprehensive understanding of the fluid flow and molecular transport under dif-

ferent experimental conditions. First of all, visualizing the velocity field in our media channels through simulation will help us estimate the amount of media needed when setting up the perfusion experiment. It will also be utilized to estimate the interstitial flow field across each culture unit of our system. In addition, we also want to get the pressure distribution information in the system, as that is a parameter that we can control and tune manually.

The Navier-Stokes equation and the Continuity equation govern the motion of fluids and is at the heart of fluid flow modeling. Solving them, for a set of boundary conditions (such as at inlets, outlets, and walls) and initial conditions, predicts the fluid velocity and its pressure in a given geometry. For a free channel, these equations are already sufficient. However, in our application, we also need to consider the existence of a porous material region designed for our 3D tissue culture. Based on the hypothesis that in a porous medium, the global transport of momentum by shear stress in the fluid is often negligible [56], Darcy' law gives a simple proportionality relationship between the instantaneous flow rate through a porous medium u, the permeability of the medium K_{gel}, the dynamic viscosity of the fluid μ, and the pressure drop ∇P by :

$$\nabla P = -\frac{\mu}{K_{gel}}u \tag{2.1}$$

A common way to deal with the coupled free and porous media flow problem is to incorporate Darcy's law adjacent to the Navier-Stokes equations, which is also numerically easy to solve. However, this approach does not account for viscous effects arising from the free media flow, which might still be important in the interface region between the free flow and the porous media.

The Brinkman equation is an extension of Darcy's law and it accounts for momentum transport by viscous effects [57]. There are two cases where the Brinkman equation is preferred over Darcy's law. The first case is when there is a single porous media domain with fast moving fluids, and thus the dissipation of the kinetic energy by viscous shear is non-negligible [58]. The second case, which is also the reason why we are applying this equation, is when there is a transition between fast flow

34

in channels described by the Navier-Stokes equations and slow flow in porous media governed by Darcy's law[59]. The Brinkman equation states that

$$\nabla P = -\frac{\mu}{K_{gel}}u + \frac{\beta\mu}{K_{gel}}\nabla^2 u \qquad (2.2)$$

Where β is given by [60]

$$\beta = \frac{c_F}{\sqrt{K_{gel}}} \qquad (2.3)$$

and c_F is called the frictional coefficient and it can be estimated from the porosity of the gel ε_{gel} [60]

$$c_F = \frac{1.75}{\sqrt{150\varepsilon_{gel}^3}} \qquad (2.4)$$

We use COMSOL Multiphysics® to solve the equations mentioned above combined with other boundary and initial conditions to get the pressure and velocity solutions in both the free channels and the porous region. COMSOL® offers a convenient module interface for our application, which is called the Porous Media Flow module. It has a number of physics interfaces under it which pre-defines sets of equations adapted to mass, momentum and energy transport in porous media, as shown in Figure 2-3 , to solve a transport problem. As we discussed above, we have two distinct domains. One will be governed by the Navier-Stokes equations, and the other will be governed by the Brinkman equation. It's suggested that using Free and Porous Media Flow interface for modeling a problem in our case, where the free flow is connected to the porous media. The physics interface also adds functionality that allows the equations to be optimized according to the flow properties of relevant domains. Besides, it supports both stationary and time-dependent solutions, which is also a desirable feature in our modeling problem.

2.1.2 Vascular Endothelial Growth Factor A

Vascular Endothelial Growth Factor (VEGF) is a family of important signaling proteins involved in a variety of vasculature activities, such as endothelial proliferation, migration, invasion and survival, as well as vascular permeability and vasodilation [61]. It is classified into 5 members, of which VEGF-A has been mostly studied for its role in endothelial cell vasculogenesis and angiogenesis [62]. The presence of VEGF gradient has been shown to be a key signal regulating sprout formation of endothelial cells. The VEGF gradient activates the endothelium and a VEGF/notch-dependent regulatory mechanism, which selects a limited number of tip cells and promotes tip cell sprouting towards the VEGF gradient. Adjacent stalk cells follow the guiding tip cell and proliferate to support sprout elongation [55].

Therefore, VEGF-A gradients have been widely exploited in *in vitro* angiogenesis and vasculogenesis models on microfluidic platform, for instance, to study the paracrine interactions of the endothelial cells with the VEGF gradient or to induce stable sprout formation [7, 63, 64]. One common strategy (which is also what we will adopt) is to provide a high concentration of VEGF-A and a zero-concentration respectively in 2 channels separated by a cell culture channel. In theory, a linear gradient will form within certain time window depending on the diffusion coefficient and the width of the channel ($\tau \approx \frac{\text{L}^2}{\text{D}}$). However, this is only valid when there is no reaction between the growth factor and the medium it is going through. The medium can contain molecules that will bind to VEGF-A. Furthermore, in a cellular system, other complex biochemical reactions, such as proteases and/or cell secretion, will also arise and regulate the distribution/gradient of the growth factor.

Importantly, there are multiple isoforms of VEGF-A which result from alternative splicing of mRNA from the VEGF-A gene (8 exons) as shown in Figure 2-1. Splicing alters its biochemical properties. For example, alternative splicing of exon 6 and 7 mediates their interactions with heparan sulfate proteoglycans (HSPG), while the binding sites for VEGF receptors (VEGFR1 and VEGFR2) are encoded by exon 3 and exon 4, respectively [62].
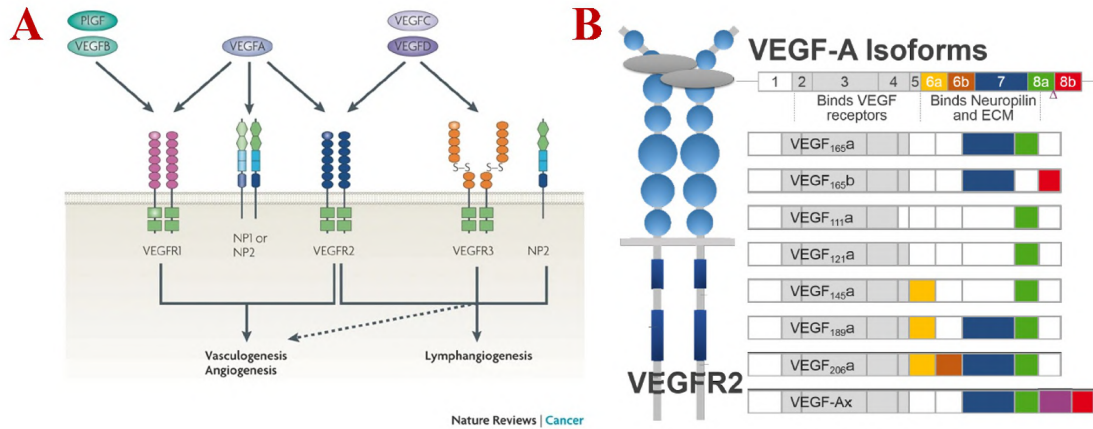
Figure 2-1: A) VEGF family of which VEGF-A can act on VEGFR1, VEGFR2 and NP receptors. VEGF-A has been mostly studied on its role in vasculogenesis and angiogenesis. Reproduced with permission from [65]. B) VEGF-A isoforms generated by alternative spicing, which alters its biochemical properties. Reproduced with permission from [66].

VEGF121, VEGF165 and VEGF189 are the most frequently occurring isoforms of human VEGF-A (murine isoforms are 1 amino acid shorter). These 3 isoforms differ greatly in their HSPG-binding affinity, with longer isoforms display stronger HSPG binding [67]. The restriction of the rate of diffusion by ECM sequestration is a contributor to gradient formation. VEGF isoforms that bind strongly to the ECM, such as VEGF165 and VEGF189, were found to have a steep gradient and tight pericellular sequestration *in vivo* [68]. These monotonic relationships in amino acid length, HSPG binding ability, steepness of the gradient, also correlate with the patterning behavior of these 3 isoforms. Mice expressing only VEGF120 showed poor branching, tortuous and leaky vessels, while VEGF188-only mice also displayed abnormalities in vessel branching in the opposite direction from those expressing only VEGF120, with an excess of thin and disorganized branches. Remarkably, mice expressing only VEGF164 displayed normal vascularization [69]. Therefore, the isoform-specific ECM-binding behavior and spatial distribution need to be taken into account in our system as they have distinct profiles and induce remarkably different patterning behavior.

37
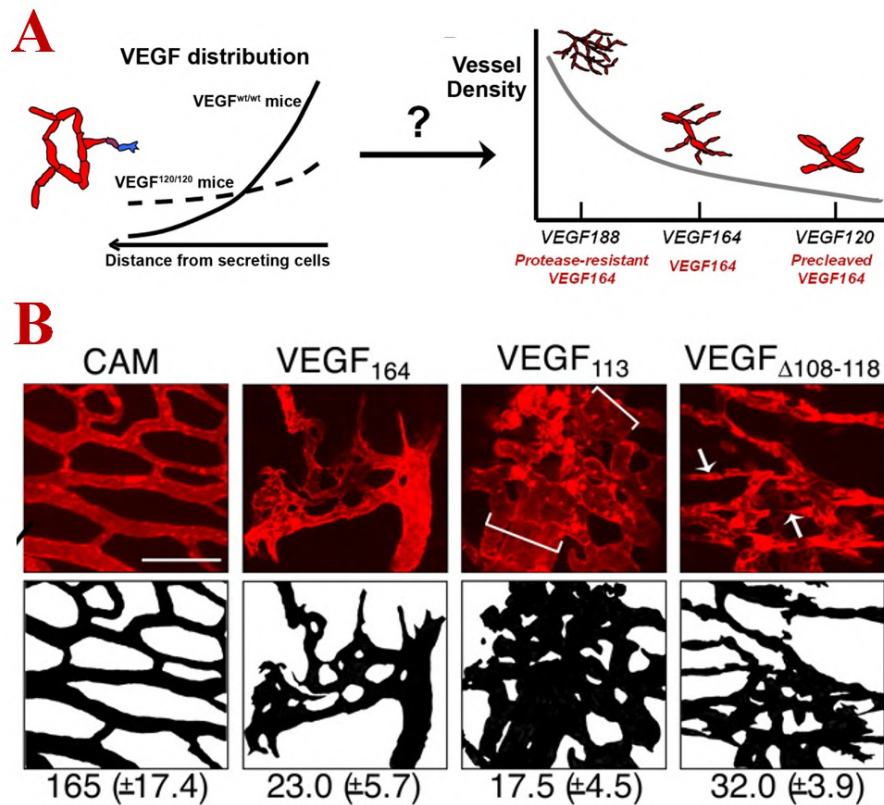
Figure 2-2: A) Mice engineered to express only VEGF120 developed a distinct VEGF distribution compared with the wild-type mice, which expressed predominantly VEGF164. Different isoforms also induced different vascular patterning behavior. Reproduced with permission from [70]. B) VEGF availability can be regulated extracellularly by MMPs. The cleaved form VEGF113 induced large, dilated vessel compared with the predominant form VEGF164 in the wide-type mice. Reproduced with permission from [71].

Another important mechanism in regulating VEGF distribution and action is proteolytic processing. The best-studied VEGF proteases are plasmin and the matrix metalloproteinases (MMPs) [61]. Lee et al. reported [71] that various MMPs, especially MMP-3, can cleave VEGF165 to generate diffusible, non-heparin-binding fragments. These fragments resulted in poor vascular density and vessels that were larger than their wild-type counterparts (Figure 2-2B). Therefore, proteolytic processing is also an important factor that affects the local availability of VEGF and VEGF distribution as a whole. Further more, in our device, there is always interstitial flow driven by the pressure difference. Studies have shown that interstitial flow

can regulate the sprouting performance in different ways. Interstitial flow can alter the proteases distribution [72], or endothelial cells can integrate signals from both the interstitial flow and local VEGF gradients [73].

Different isoforms give rise to a spectrum of angiogenesis patterns marked by differences in branching. Proteolysis by enzymes and enzyme transport by interstitial flow also regulate VEGF gradient. Therefore, a transport model for VEGF which considers not only diffusion but also these crucial biochemical/biophysical interactions in a microfluidic system will be able to better capture the true VEGF spatial distribution and dynamics. More importantly, a valid VEGF transport model will help us re-design device features, assess the effect of control parameters over the system (the concentration of the growth factor, the applied pressure, different dilution factor to the Matrigel $^{®}$ etc.). It will also be beneficial in interpreting our future capillary morphogenesis data. The Transport of Diluted Species in Porous Media interface within COMSOL$^{®}$ is tailored to model solute transport in saturated and even partially saturated porous media. It not only characterizes the rate and transport of individual but also multiple interacting chemical species by coupling it to a chemical physics. Besides, the velocity can be further coupled to the velocity can be further coupled to the Free and Porous Media Flow physics. In this chapter, we will set up the model using different combinations of these three sets of physics depending on our problems of interest.

2.2   Modeling Set-up

2.2.1   Free flow and Porous media flow

The COMSOL$^{®}$ Free and Porous Media Flow interface can be found under the Porous Media and Subsurface Flow branch when adding a physics interface. The dependent variables in this physics are flow velocity and pressure, which will be later coupled to other physics of interest. For the free flow in our channel, the governing equations are the Navier–Stokes equations and since we mostly solve for the time-dependent

solutions, the default time-dependent equations displayed in this domain are:

$$\rho\frac{\partial \mathbf{u}}{\partial t} + \rho(\mathbf{u} \cdot \nabla)\mathbf{u} = \nabla \cdot [-P\mathbf{I} + \mathbf{K}] + F$$

$$\rho\nabla \cdot \mathbf{u} = 0 \tag{2.5}$$

$$\mathbf{K} = \mu(\nabla\mathbf{u} + (\nabla\mathbf{u})^T)$$

For the porous media, the equations are:

$$\frac{1}{\varepsilon_{gel}}\rho\frac{\partial \mathbf{u}}{\partial t} + \frac{1}{\varepsilon_{gel}}\rho(\mathbf{u} \cdot \nabla)\mathbf{u}\frac{1}{\varepsilon_{gel}} = \nabla \cdot [-P\mathbf{I} + \mathbf{K}] + \left(\frac{\mu}{K_{gel}} + \beta\varepsilon_{gel}\rho|\mathbf{u}| + \frac{Q_m}{\varepsilon_{gel}^2}\right)\mathbf{u} + F$$

$$\rho\nabla \cdot \mathbf{u} = Q_m$$

$$\mathbf{K} = \mu(\nabla\mathbf{u} + (\nabla\mathbf{u})^T) - \frac{2}{3}\mu\frac{1}{\varepsilon_{gel}}(\nabla \cdot \mathbf{u})\mathbf{I}$$

$$\tag{2.6}$$

Where ε_{gel} and K_{gel} are the porosity and permeability, respectively. β is given in the equation 2.3. The $\mathbf{I}$ is the identity matrix. There can be some simplification to the equation that you can specify. We are using 2D simulation because we assume in z direction all the physical properties (velocity, pressure and concentration) stay homogeneous. In addition, 2D model also reduces the computation time significantly. In our case, the mass source/sink Q_m and the volume force F are both zero. Other important modeling settings are shown in Figure 2-3.

Based on equation 2.6, we need to figure out 2 effective macroscopic properties for Matrigel®, which are the permeability (used in equation 2.3 along with the frictional coefficient to estimate β) and the porosity.

Fiber matrix model is usually used to estimate the permeability of porous media [74]. In this theory, a typical particle in the porous medium is modeled within a unit cell. A boundary condition is applied (typically zero shear) At the border of the unit cell to account for the viscous effects of the other fibers. The permeability is determined by solving the Stokes equations within this space and then generalizing to the entire porous space. However, this model is only suitable for single-component porous media. For a porous media which is composed of fibers of different radii,
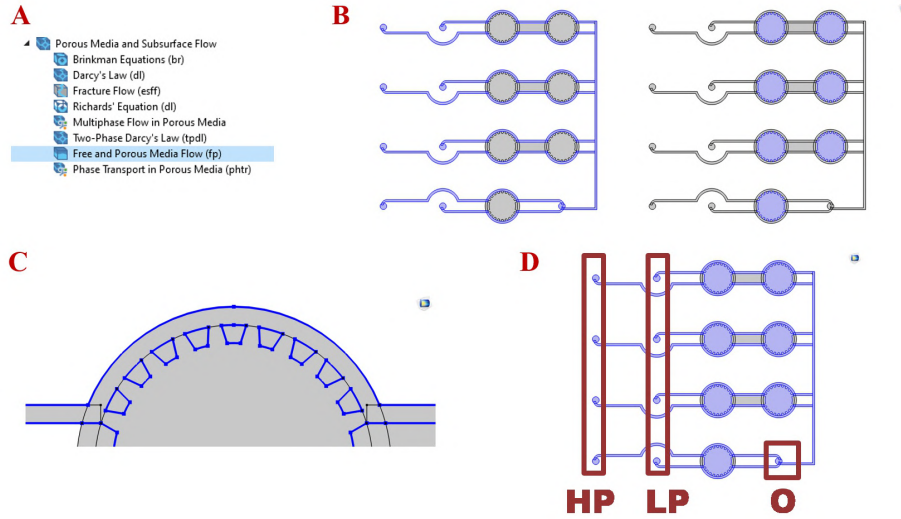
Figure 2-3: Free and Porous Media Flow physics. A) Physics used here is highlighted. B) 2 separate domains in our device with the left panel showing the free flow region and the right showing the porous media region. C) A no-slip condition is applied to the highlighted walls. D) HP: high-pressure inlets, pressure set to 120 Pa. LP: low-pressure inlets, pressure set to 20 Pa. O: outlet, pressure set to 10 Pa.
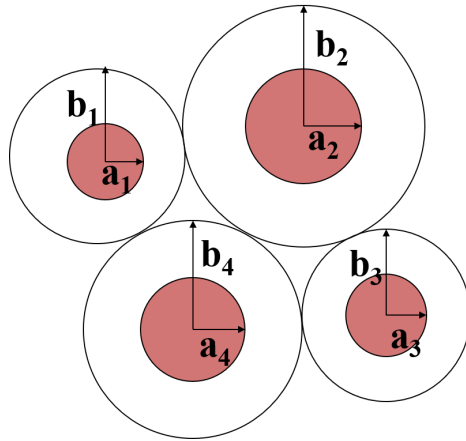
Figure 2-4: Method used to calculate the cell size in the fiber matrix model where $b_i - a_i = \lambda$.

Mccarty and Johnson proposed a way to estimate the permeability [75] based on the volume fraction of each component and experimentally validated the model. We took this approach and also took into account of our own experimental conditions such as dilution factor used and slightly different compositions of Matrigel® coming from a different manufacturer. The model calculates the permeability as follows. As shown in Figure 2-4, we considered the 4 main components of Matrigel®. a_i is the fiber radii

41

of each individual fiber, b_i is the radii of the unit cell. The distance $b_i - a_i = \lambda$ is a constant for all fiber types. The number density of each fiber n_i (which means the fraction of the total number of fibers in a random cross-section) is

$$n_i = \frac{\phi_i/\pi a_i^2}{\sum_i \frac{\phi_i}{a_i^2}} \tag{2.7}$$

where ϕ_i is the volume fraction of each fiber type. The constraint is

$$\frac{\sum n_i \pi a_i^2}{\sum n_i \pi b_i^2} = \sum \phi_i = \phi \tag{2.8}$$

Replacing b_i with $a_i = \lambda$ we have

$$\lambda^2 \left[\sum_i \frac{\phi_i}{a_i^2} \right] + 2\lambda \left[\sum_i \frac{\phi_i}{a_i} \right] + \left[\sum_i \phi_i \right] - 1 = 0 \tag{2.9}$$

For each fiber type, the permeability $K_i(b_i, a_i)$ of a network for a random fibrous porous medium composed of a single type fiber was found using [76]

$$K_i = \frac{b_i^2}{a_i^2} \left[ln \frac{b_i}{a_i} - \frac{1}{2} \left(\frac{b_i^4 - a_i^4}{b_i^4 + a_i^4} \right) \right] \tag{2.10}$$

Parameters used in this estimation are listed below:

Fiber type	Fiber Radii a_i (nm)	Ref
Collagen IV	0.7	[75]
Laminin	0.6	[75]
Entactin	0.8	[75]
HSPG	0.5	[77]

Table 2.1: Fiber radii chart

Then, the permeability of the network is calculated as

$$K = \left[\sum_{i=1}^{N} \frac{n_i}{K_i(b_i, a_i))} \right]^{-1} \tag{2.11}$$

The composition by weight given by the manufacturer is 60% collagen type IV,

30% laminin, 8% entactin and roughly 2% HSPG [78]. But It is generally assumed that the spatial average of the density of proteins is equal especially for proteins with MW larger than 50 kDa [79], which is the case for all these four main components of Matrigel®. As a result, it is a reasonable assumption that the volume fraction is the same as the weight fraction. After we account for the dilution we normally do (which reduces the volume fraction of each type of fiber by half), the calculated permeability is K = 4.28 $\times 10^{-17}$ m^2. In the reference [75], people found that the permeability of 1% Matrigel (BD biosciences) was measured to be 2×10^{-17} m^2 under zero pressure, which is one the same order of our calculation result.

Scanning electron microscopy demonstrated that Matrigel® presents a much denser and constrained matrix compared to other commonly used matrix such as collagen I [80, 81]. One quantitative number for the porosity of the mixture of 4 mg/mL Matrigel with 2 mg/mL collagen I was reported to be 0.4 [82]. We believe our gel (4mg/mL - 5 mg/mL due to the dilution from 10mg/mL - 12 mg/mL given by the manufacturer) acts between the pure Matrigel® (panel 1 in Figure 2-5) and panel 7 (reported to be 0.4 in [82]) . Therefore, the porosity used in our simulation is 0.2.
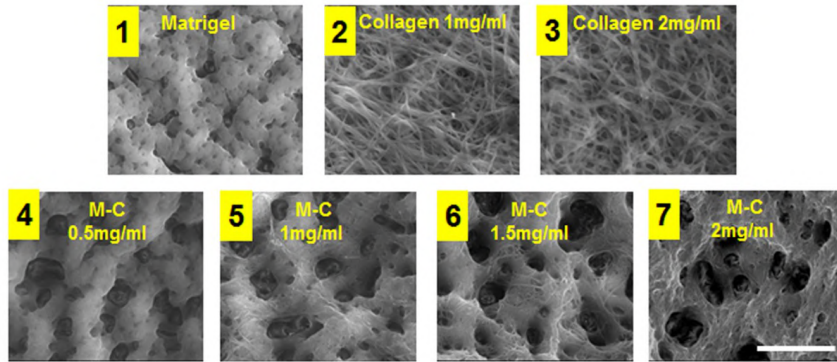
Figure 2-5: Porosity estimation from panel 1 and panel 7. Reproduced with permission from [81].

2.2.2 Transport of diluted species in porous media

The dependent variables in this physics are concentration profiles of species of interest. Similarly, the free flow region and the porous material region utilize different equations

to give out the solutions. For the free channel region, the equation is a well-known diffusion-convection-reaction equation in its time-dependant form.

$$\frac{\partial c_i}{\partial t} + \nabla \cdot \mathbf{J_i} + \mathbf{u} \cdot \nabla c_i = R_i$$
$$\mathbf{J_i} = -D_i \nabla c_i$$

(2.12)

In which the C_i is the concentration of the species, J_i is the diffusive flux, R_i is the reaction rate and Di is the diffusivity. Whereas for the porous media,

$$\frac{\partial(\epsilon_{gel} c_i)}{\partial t} + \frac{\partial(\rho c_i)}{\partial t} + \nabla \cdot \mathbf{J_i} + \mathbf{u} \cdot \nabla c_i = R_i + S_i$$
$$\mathbf{J_i} = -D_{e,i} \nabla c_i$$

(2.13)

The $D_{e,i}$ is the effective diffusivity and the interface provides pre-defined expressions to compute it by

$$D_{e,i} = \frac{\varepsilon_{gel}}{\tau_i} D_i$$
$$\tau_i = \varepsilon_{gel}^{-1/3}$$

(2.14)

The S_i needs to be specified if it is a partially saturated material. We assume saturated porous media in our case so it is set to 0. This physics is coupled to the Free and Porous Media Flow physics to derive the velocity as the input in this physics. Other details in this physics are shown in Figure 2-6.

2.2.3 Biochemical reactions

A Chemical physics is set up to account for the HSPG binding reaction and the proteolysis reaction. In Transport of Diluted Species in Porous Media, a node will be set up to get reaction rate of individual species from this physics. The reaction parameters used are shown in the table 2.2 and 2.3.

Other modeling parameters are summarized in table 2.4.
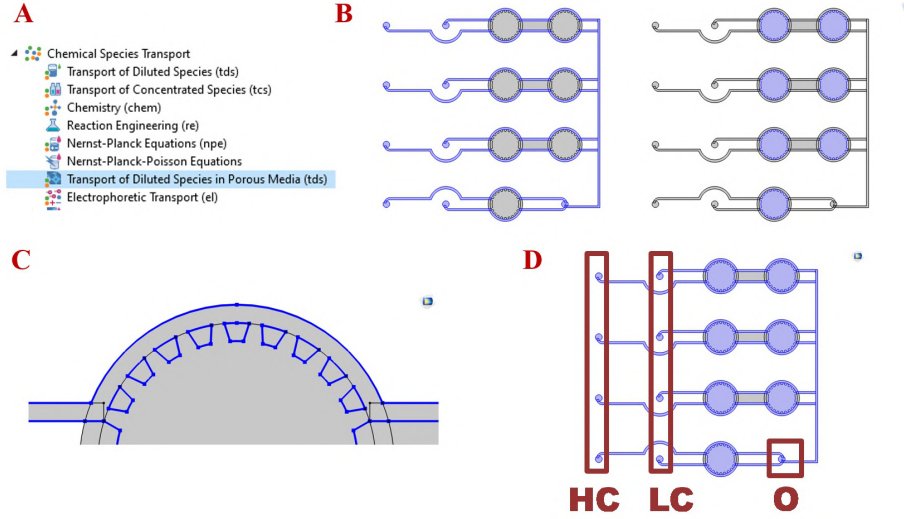
Figure 2-6: The Transport of Diluted Species in Porous Media physics. A) Physics used here is highlighted. B) 2 separate domains in our device with the left panel showing the free flow region and the right showing the porous media region. C) A no-flux condition was applied to the highlighted walls. D) HC: high VEGF concentration inlets, concentration set to 0.5 nM. LC: low VEGF concentration inlets, concentration set to 0. O: outlet. The initial VEGF concentration for the whole device is 0.

Parameter	Value	Source
HSPG initial concentration in the ECM	0.75 μM	Calculated
k_{on} of VEGF165 to HSPG	6.06×10^4 M^{-1}s^{-1}	[70]
k_{off} of VEGF165 to HSPG	0.01 s^{-1}	[70]
k_{on} of VEGF189 to HSPG	1.18×10^6 M^{-1}s^{-1}	[70]
k_{off} of VEGF189 to HSPG	0.01 s^{-1}	[70]

Table 2.2: HSPG binding related parameters for the reaction: VEGF + HSPG $\underset{k_{off}}{\overset{k_{on}}{\rightleftharpoons}}$ [VEGF · HSPG].

Parameter	Value	Source
k_{pro} for medium proteolysis	631 M^{-1}s^{-1}	[83]
k_{pro} for strong proteolysis	6310 M^{-1}s^{-1}	assumed
Proteases concentration in steady-state (without convection)	10 nM	[83]

Table 2.3: Proteases degradation related parameters for the reactions: VEGF + Proteases $\xrightarrow{k_{pro}}$ VEGF$_c$ + Proteases and [VEGF · HSPG] + Proteases $\xrightarrow{k_{pro}}$ VEGF$_c$ + Proteases, where VEGF$_c$ is a cleaved product.

Description	Value
Diffusion coefficient for all 3 isoforms	$6.56e^{-11}m^2/s$
Permeability of the gel	$4.28 \times 10^{-17}m^2$
Porosity of the gel	0.2
Pressure of the HP inlets	120 Pa
Pressure of the LP inlets	20 Pa
Pressure of outlet	10 Pa
VEGF Concentration of the HC inlets	0.5 nM
VEGF Concentration of the LC inlets	0

Table 2.4: Other parameters used in the simulation.

2.3   Results

2.3.1   Device dimension optimization

To visualize the velocity field and pressure field of the device and perform further geometry optimization to get our desired velocity and pressure profiles, we first performed simulation using only the Free and Porous Media Flow physics. We imported the geometry as shown in Figure 2-7A and solved for the steady-state pressure solutions. The pressure difference was designed to be 100 Pa, while the result shows that the difference becomes 53.0 Pa and 20.3 Pa for the two culture units on the same branch, which indicates they can not be viewed as repeats as we designed since pressure acts as the driving force for interstitial flow. Ideally, we want the difference of these two pressure driving forces to be within 5%. In addition, the velocity profile suggests that there is significant backflow, which also indicates malfunction of the device. We re-designed the device channels by adding a series of high resistance channel and a low resistance channel as shown in Figure 2-8B (to make the pressure drop mainly occur in the high resistance channel).

We then seek to do a more comprehensive analysis of the channel dimensions by setting these 3 dimensions as variables and the rest device layout is set up using these 3 parameters. We ran a parametric sweep in 3 practical ranges and obtained the flow direction as the readout. The results (Figure 2-9) suggests that, there is a range of combinations of parameters (red region) that we can choose from. The results indicated that a wider flow channel (var1), a narrower high-resistance channel (var2)
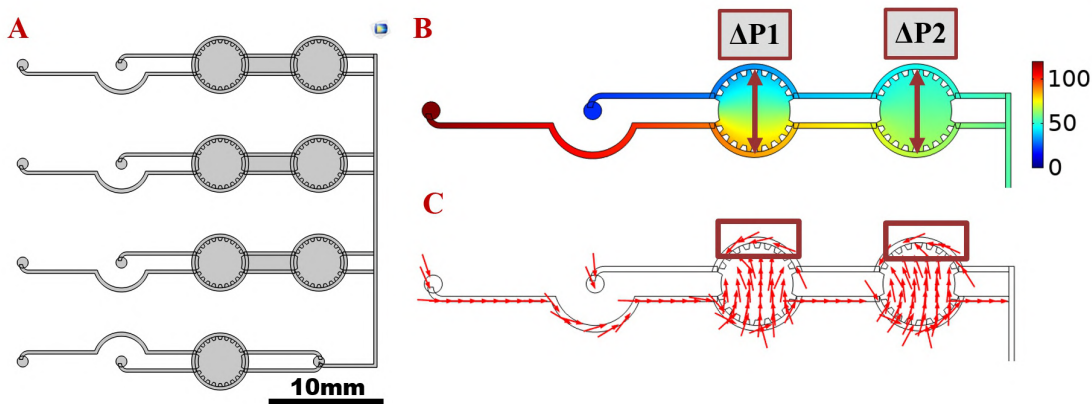
Figure 2-7: A) Original geometry used in the simulation. B) Pressure profile. ΔP1 = 53.0 Pa and ΔP2 = 20.3 Pa. C) Velocity profile with the backflow outlined in the red boxes.
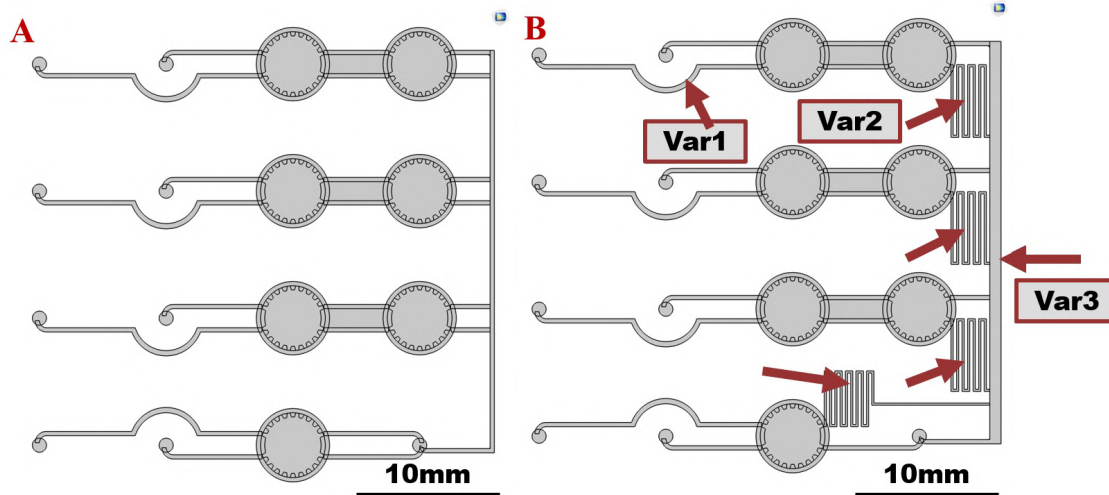
Figure 2-8: A) Original geometry B) Updated geometry with 3 channel dimensions as 3 variables.

and a wider low-resistance channel (var3) are all conducive to eliminating the backflow problem. The plausible choices for these parameters are understandable given that we want most of pressure drop occurs in the high-resistance channel (var2) in order to get rid of the backflow. We can again look at the pressure and velocity profile, which is shown in Figure 2-10. Now the pressure difference is within 5% (ΔP1 = 93.3 Pa and ΔP2 = 89.7 Pa) and the flow is correctly pointing to the outlet direction.

By coupling the Free and Porous Media Flow physics with the Transport of Diluted Species in Porous Media, we are able to see the process of VEGF gradient establish-
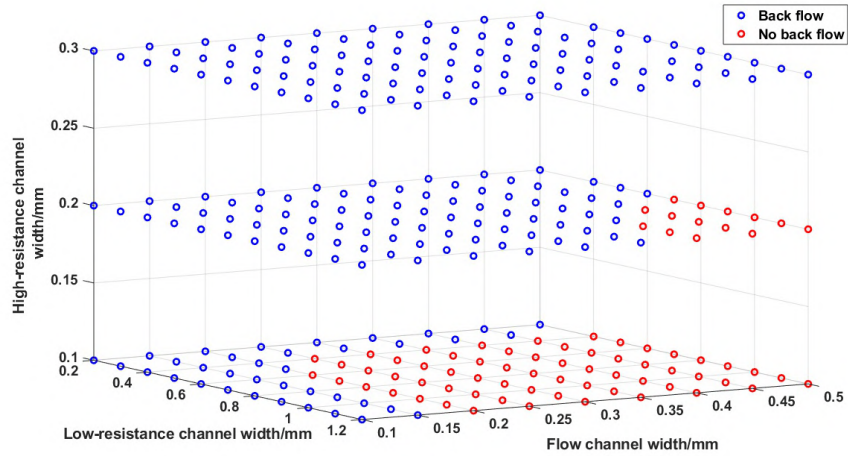
Figure 2-9: Channel dimension design to prevent back flow with working parameters highlighted in red.
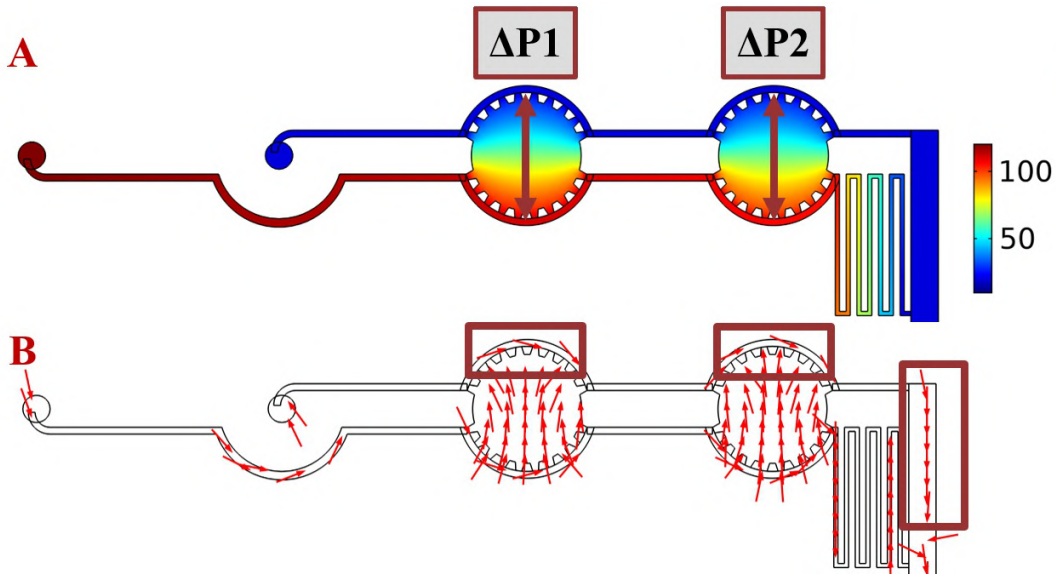
Figure 2-10: A) Pressure profile. ΔP1=93.3 Pa and ΔP2=89.7 Pa. B) Velocity profile with the correct floe direction outlined in the red boxes.

ment without considering any reaction here (without considering any reaction first which is the case for VEGF121). When we plotted the VEGF121 concentration along with the specified line in Figure 2-11A, we observed that the concentration line rises sharply from a zero-line due to the preset zero initial conditions (blue) to the green line (6 h) and then it slowly advances to the steady state which takes approximately 48 h (Figure 2-11C). When we later want to validate the model experimentally, we

want fast dynamics (such as 12 h) because it will require less reagent consumption, less frequency imaging etc., which we will discuss in section 3.3.2. As a result, we reduced the characteristic length of the 3D culture region in the direction which is perpendicular to the free flow channels (from L1=4.7 mm to L2=2 mm). After that, we observed approximately 5 times faster gradient establishment as shown in 2-11D (consistent with the $\tau \approx \frac{L^2}{D}$ estimation). What should also be noted is that in both Figure 2-11C and Figure 2-11D, the final profile is not completely linear (the gradient is not a constant value). We believe this is due to the strategy of the concentration evaluation. The profiles are evaluated at a line which is slightly offer-center due to the existence of the posts, which means the velocity on the line is not consistent with direction the specified line therefore a straight concentration profile is not expected. We will keep using this geometry in later sections of this chapter.
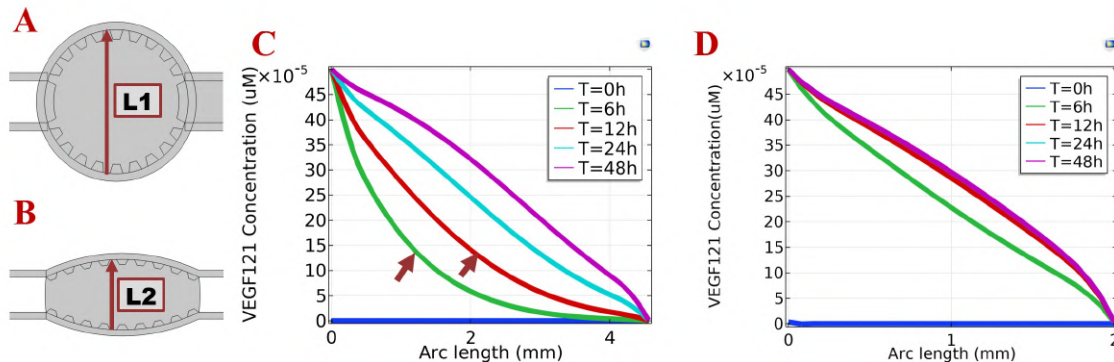
Figure 2-11: Further optimization on the characteristic length to establish the gradient quicker. A) Original 3D cell culture unit. B) After reducing the characteristic length (L1=4.7 mm and L2=2 mm). The red arrow line shows the location and the direction for the concentration evaluation in C) before geometry optimization and D) after geometry optimization. We will keep using the same evaluation line unless specified otherwise.

2.3.2 Matrix binding of Vascular Endothelial Growth Factor

The transport dynamics in Figure 2-11 do not account for any possible reactions during the transport process. However, as we discussed in section 2.1.2, VEGF-A contains different isoforms and these isoforms differ in their ECM-binding ability,

which will lead to isoform-specific concentration gradient throughout the device. So here we will discuss mainly isoform-specific transport characteristics.
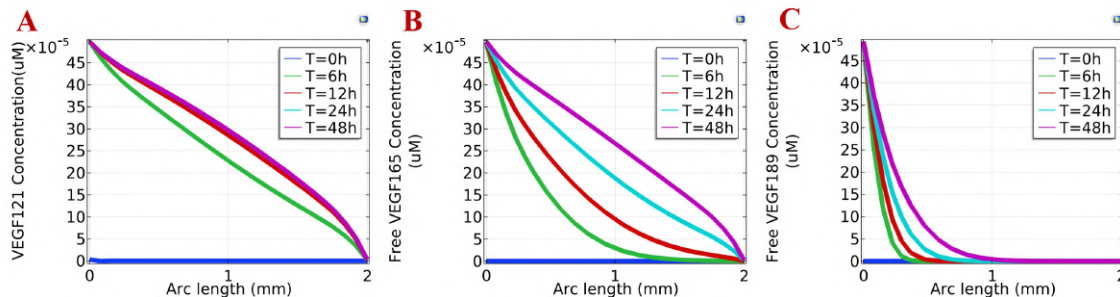
Figure 2-12: Free form concentration profile for A) VEGF121, B) VEGF165 and C) VEGF189.

Panel A in Figure 2-12 is the desired "quick" gradient formation profile after we optimized the geometry. Nonetheless, this is only valid for VEGF121. For VEGF165, the gradient formation is again slowed down approximately 4 times (12h vs. 48h). Moreover, for VEGF189, around 50% of the whole evaluation line is experiencing a zero-VEGF gradient as well as a zero-VEGF magnitude even at 48h (Figure 2-12C). The remarkable difference in Figure 2-12A/B/C is a result of their distinctive disassociation rates for the HSPG binding reaction: 165 nM and 8.5 nM are specified for VEGF165 and VEGF189, respectively, while no binding reaction is added to the VEGF121 simulation. Higher affinity for the ECM HSPG means that a longer time duration is required for VEGF to reach the opposite end of the VEGF source channel. It's evident that a linear profile cannot be easily assumed for every isoform of VEGF-A. Therefore, it is necessary to take the effect of matrix binding into consideration when designing device geometry or experimental protocol. What should also be noted is that the analysis here is also dependant on the relative amount of HSPG and VEGF. In our case, the HSPG concentration (0.75 μM) is around 1000 times the VEGF concentration (0.5 nM), and therefore the HSPG is far from saturated.

The HSPG-bound form of VEGF-A also plays an important role in VEGF/VEGFR signalling as investigated by previous works [84]. Therefore, we also evaluated the HSPG-bound form concentration. HSPG-bound VEGF189 demonstrates a much sharper gradient than VEGF165, also with 20 times higher concentration in the out-
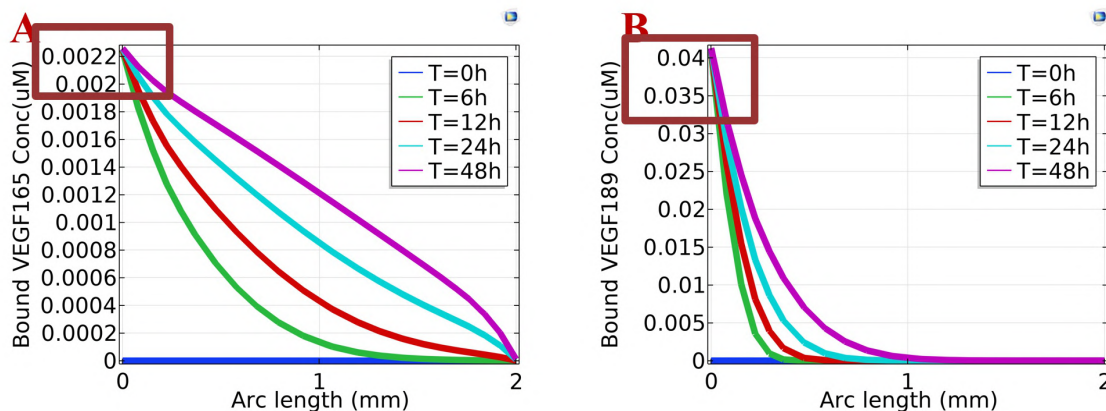
Figure 2-13: HSPG-bound form concentration profile for A) VEGF165 and B) VEGF189 with the concentration magnitude near the VEGF source channel highlighted.

lined region (near the VEGF source). This is sometimes referred as the VEGF reservoir [68, 69] and it has important underlying information. VEGF189 remains almost completely stored by HSPG in the ECM, but when needed, can be released quickly by the action of proteases to regulate many endothelial cell activities.

2.3.3 Proteolysis and interstitial flow

Binding to the ECM and proteolytic processing are believed to be two key mechanisms in regulating VEGF action [85]. Thus, we further take into account the action of proteases, with the medium cleavage rate by proteases chosen to be 631 $M^{-1}s^{-1}$ (a value estimated by fitting experimental data from a previous work [83]) and strong proteolysis is defined as 10 times of the medium proteolysis rate. Proteases can act both on the free form and the bound form [83]. Since proteases reaction cleaves the original form, it's not surprising that we are seeing the trend as shown in Figure 2-14. Figure 2-14 is evaluated at 48h for VEGF165. This study reveals that, even when HSPG-binding is considered and longer time window is given for the formation of a linear gradient, the existence of the proteolytic processing can still alter the gradient profile (from a linear profile throughout the evaluation line vs. 50% of the region not experiencing any VEGF and the other 50% experiencing a steep VEGF gradient) and make it harder for VEGF to penetrate the whole 3D cell culture region.
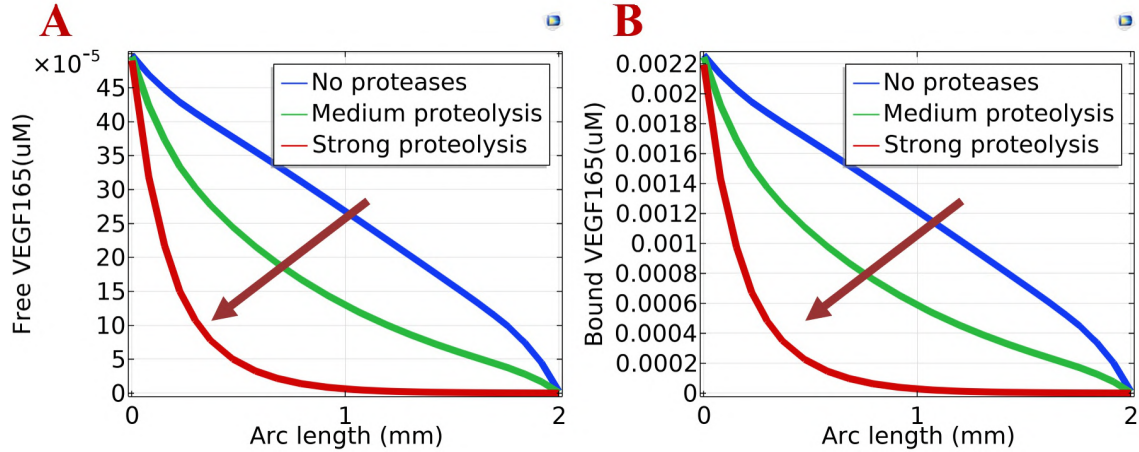
Figure 2-14: A) Free and B) HSPG-bound VEGF165 when 2 different degrees of proteases reaction are assessed. Time T = 48 h.

In our system, proteases transport by interstitial flow results in an opposite gradient compared with VEGF, which was mentioned in an early report as the skewing effects of convection on the VEGF-liberating proteases [72]. The degree of this effect was examined and shown in Figure 2-15. Panel A indicates that proteases form a gradient when the interstitial flow-driven convection is enabled. Panel B and C are the concentration profile of VEGF165 when the interstitial flow-driven convection for proteases is disabled. When we combine the effect of the proteases gradient on the concentration profiles, we obtained panel D and E, with the arrows indicating the effect of adding the proteases transport. It leads to a maximum 50% increase in the concentration of both forms (at around 0.3mm from the VEGF source) and helps the growth factor enter the 3D culture region and get closer to a linear profile in general.

2.4   Conclusions

In this section, we learned how various biochemical/biophysical factors can alter the gradient distribution in our device. Although microfluidic devices are facile tools for generating linear gradient profiles of VEGF (and other growth factor of interest), which are believed to be conducive to stable sprout formation. In this chapter we find that when the effect of HSPG-binding is taken into account, VEGF189 and
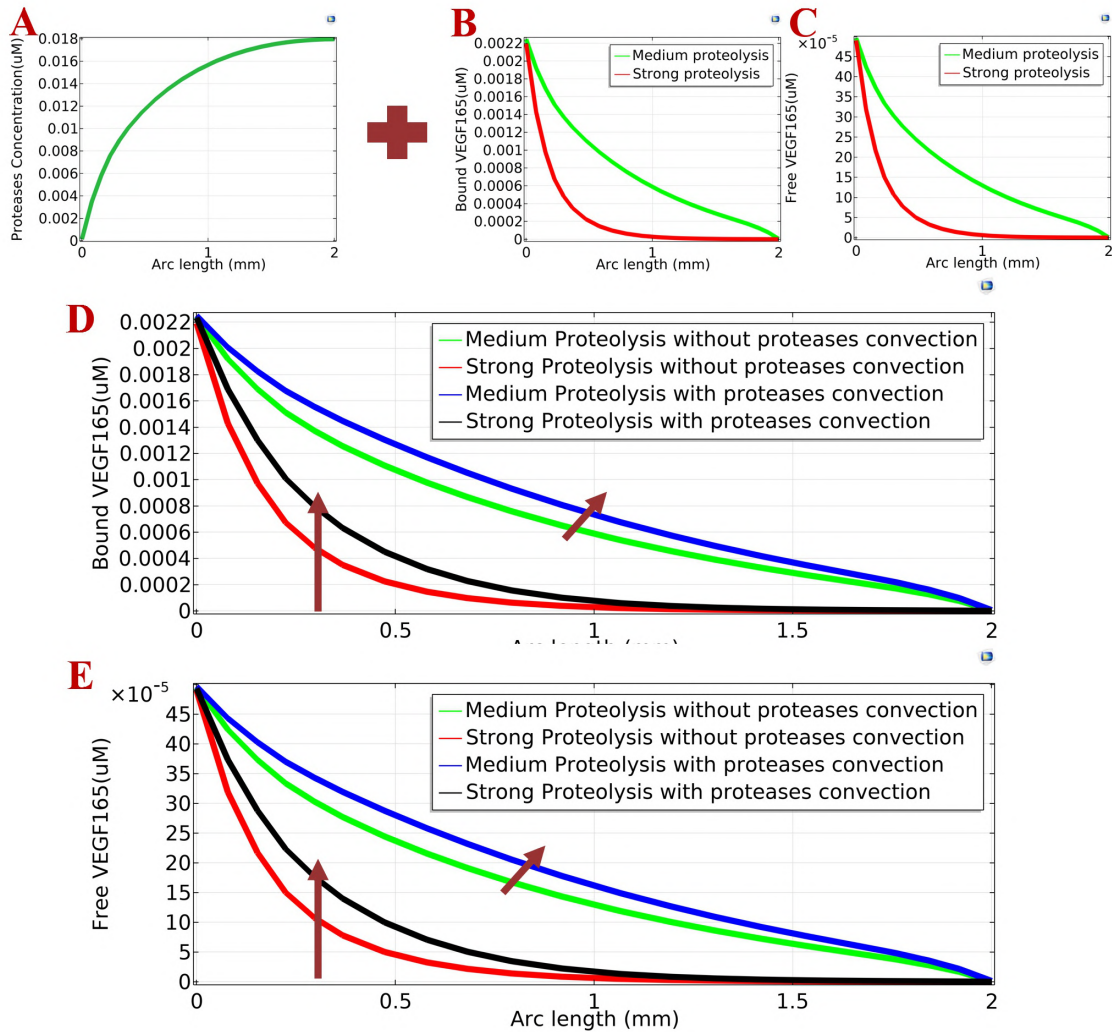
Figure 2-15: A) Proteolysis forms a gradient when the interstitial flow-driven convection is enabled. B) HSPG-bound VEGF165 and C) Free VEGF165 When proteolysis acts on both forms and interstitial flow-driven convection for proteases is disabled. D) HSPG-bound VEGF165 and E) Free VEGF165 when the proteolysis gradient is considered. Arrows showing the directional change after adding this effect. Time T=48 h.

VEGF165 display a steeper gradient but extend a shorter distance as compared with the non-HSPG-binding form when evaluated at the same time points. Non-HSPG binding form displays a linear profile within 12 h while 48h is needed for VEGF165 to establish a similar linear profile.

Commercially available VEGF-A usually contains predominately VEGF165. Although the HSPG binding of VEGF165 is not as strong as VEGF189, the concentra-

tion of the HSPG-bound VEGF165 is 5 times the free VEGF165. For VEGF189, this ratio is around 85. Research has reported that VEGF189 remains almost completely sequestered by HSPG [86]. Early *in vivo* studies have also shown that as much as 50-70% of VEGF165 could be released by heparin, which suggestions this substantial fraction can be bound to HSPG [68]. Therefore, the results from our simulation reflect a reasonable estimate of the effect of HSPG-binding.

The ability to control parameters precisely for tissue engineering is often mentioned as a major benefit of microfluidic OOC systems as compared to animal models. In our system, the flexibility to embed cells in a pre-selected gel material and to apply growth factor to induce a desirable experimental outcome actually complicates the problem. Furthermore, the effect of applied interstitial flow on enzyme distribution could also easily be neglected. Careful examination of all the possible interactions of various factors in the whole system is of vital importance to re-evaluate the device design, optimize experiment protocols and achieve unbiased experimental outcome.

Chapter 3

Experimental Validation of VEGF189 ECM Binding

3.1   Introduction

In Chapter 2, we discussed various factors that could have nonnegligible effects in shaping the VEGF gradient. In this chapter, we seek to verify one key aspect of it: VEGF binding with the ECM. VEGF189 was chosen as the target protein as it binds to HSPG in the ECM more strongly than VEGF121 and VEGF165. Fluorescently-labeled VEGF189 transport experiment was set up in a microfluidic device and its time dependent gradient formation was examined. In addition, we also applied heparinase to digest the binding domains in the ECM and then we compared the results under different experimental conditions and compared our results here with the simulation model.

3.1.1   Protein labeling

The binding between VEGF and the ECM could happen even in the absence of cell culture in the device, which could lead to a direct comparison with our ECM-binding-only data from simulation (Section 2.3.2). Although the ideal experimental readout would be the concentration profiles of both the original form and the matrix-bound

form for each specific isoform, at various time points or even a real-time readout. This is intrinsically hard to realize. To approach this goal, protein labeling is a convenient tool to facilitate detection of the protein of interest. The main types of labeling strategies available for use in most biological studies include biotinylation, enzyme conjugation and covalent attachment of fluorescent probes [87]. To enable direct detection of the protein of interest, we decided to directly use fluorescent probe labeling techniques in our application. The labeled protein solution will be applied to our microfluidic device and the fluorescence signal will be imaged every other hour to minimize the adverse effect pf photobleaching resulting from frequent exposure of the fluorophore to light.

Compared to traditional dyes, Alexa Fluor$^{\text{TM}}$ dyes are a series of brighter, more photostable, and more pH resistant dyes [87]. We utilized a commercially available microscale protein labeling kit that is based on a common NHS ester reaction chemistry. NHS ester-activated crosslinkers and labeling compounds react with primary amines in the protein of interest under physiologic to slightly alkaline conditions (pH 7.2 to 9) [88] to yield stable amide bonds, as shown in Figure 3-1. The merits of this method are that it is 1) quick, with labeled proteins typically ready to use in 2 hours, and 2) purified using convenient spin filters with yields between 60% and 90% [87]. Our protein of interest is VEGF189. As we discussed in Chapter 2, VEGF189 binds to HSPG in the ECM more strongly than VEGF121 and VEGF165, and therefore it is an ideal target protein to study the effect of ECM binding.
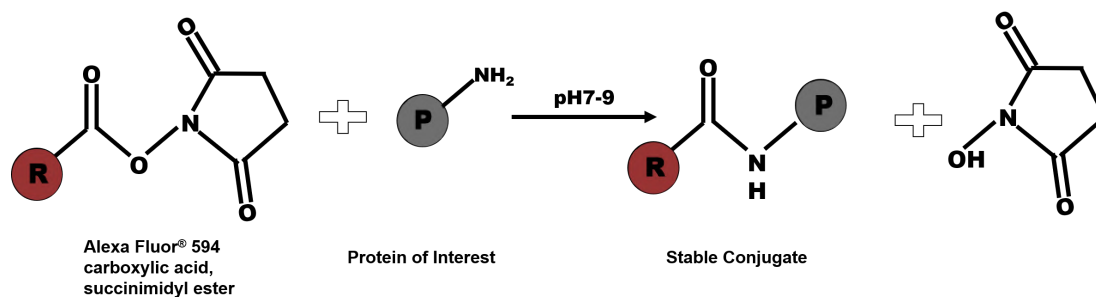
Figure 3-1: NHS ester reaction chemistry

3.1.2 Varying substrate specificity of heparinases towards heparan sulfate

Based on our hypothesis in Chapter 2, HSPG is the primary molecule that reacts with VEGF in our system, which has been supported by substantial experimental data [89, 90, 91]. Perlecan is major secreted type of HSPG family (as opposed to membrane-bound HSPG) [92] and is also believed to be a basement membrane-specific HSPG core protein [93]. It is the main HSPG form existing in Matrigel [94] and is composed of 5 distinct domains, as shown in Figure 3-2 [95]. Domains II-V share structural homologies with other protein modules while N-terminal domain I (PlnDI) is structurally unique. There are 3 heparan sulfate glycosaminoglycan (GAG) chains attached to domain I. Zoller et al. [96] discovered that perlecan binds VEGF-A via its heparan sulfate side chains and perlecan knockdown caused an abnormal increase and redistribution of total VEGF-A protein, which indicates that perlecan is required for the appropriate localization of VEGF-A. Muthusamy et al. [97] have shown that soluble forms of recombinant PlnDI bind to VEGF165 and further increase VEGF/VEGFR-2 interactions on human bone marrow endothelial cells *in vitro*, while heparinase treatment of PlnDI reduced the binding by 75%.
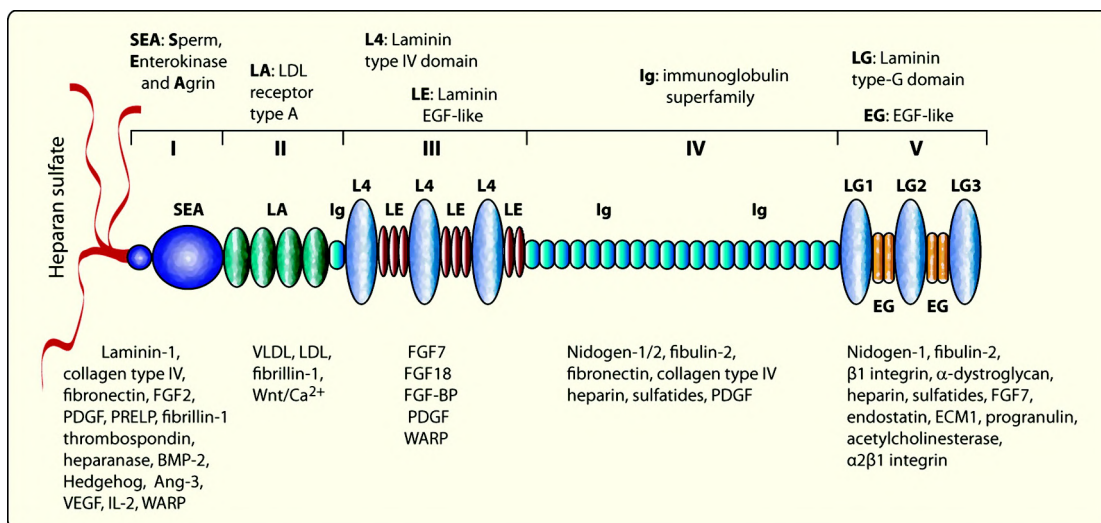
Figure 3-2: Schematic diagram of perlecan depicting the 5 domains with 3 heparan sulfate GAG chains attached to N-terminal domain I. Reproduced with permission from [95].
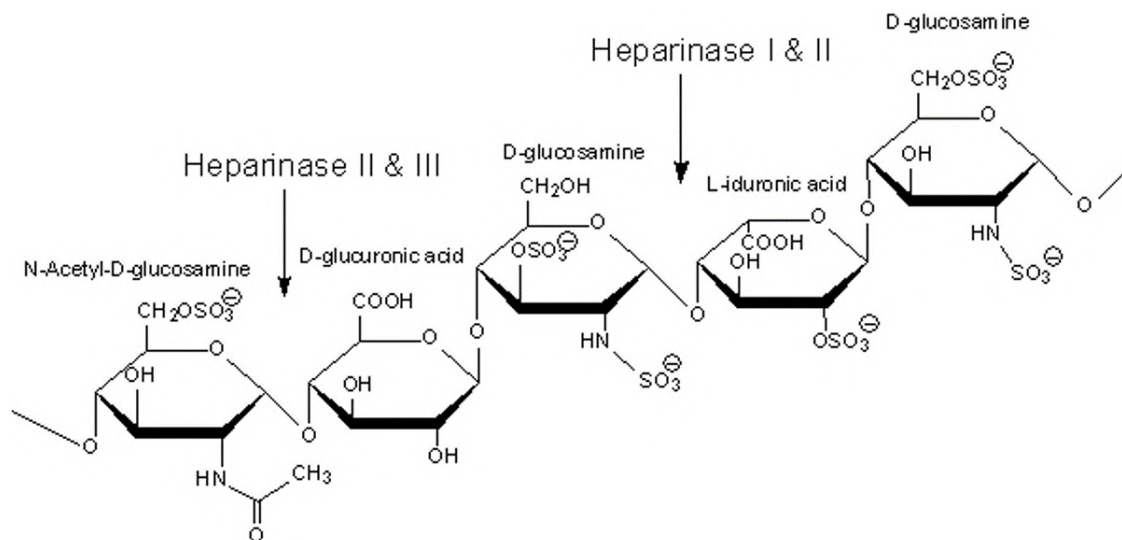
Figure 3-3: Varying substrate specificity of 3 heparinases with heparinase III having higher specificity targeting less sulfated chains in general. Reproduced with permission from [98].
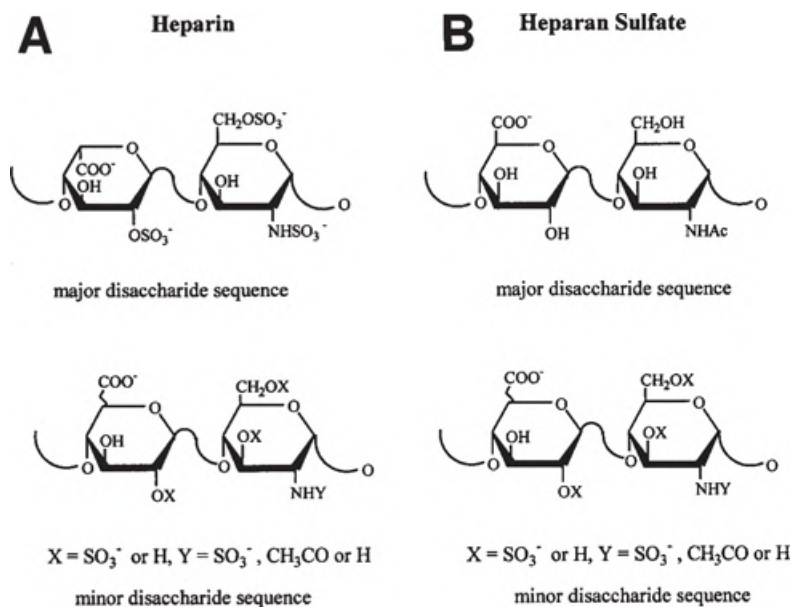
Figure 3-4: Major and minor disaccharide units of both heparin and heparan sulfate. In general, heparan sulfate is less sulfated than heparin. Reproduced with permission from [99].

Heparan sulfate can be degraded enzymatically by heparin lyases from various bacterial sources, from which heparin lyases isolated from *Flavobacterium heparinum* have been purified to homogeneity and studied extensively [100]. Three types of heparin lyases have been purified from *Flavobacterium heparinum* : heparinase I,

heparinase II and heparinase III. These 3 heparinases have varying substrate specificity, as shown in Figure 3-3. Heparan sulfate is a heterogeneous mixture of repeating disaccharide units. Various degrees of sulfation occur on each monosaccharide unit, as shown in Figure 3-4. For each disaccharide sequence, the sulfation level ranges from zero to tri-sulfation. In general, heparan sulfate is less sulfated than heparin. Heparan sulfate contains bigger amounts of the acetylated glucosamine residues than N-sulfated glucosamine, and greater content of glucuronic acid than iduronic acid [99], in contrast with heparin. Therefore, heparinase III is suitable for digesting heparan sulfate chains when you compare the molecular characteristics of heparan sulfate back to Figure 3-3.

In this chapter, we will first show both the the time dependent transport studies of a non-HSPG-binding protein (streptavidin) and one VEGF isoform which has very high affinity for the ECM (VEGF189). To test the hypothesis that HSPG is the binding site for VEGF in the ECM and have a better understanding of the VEGF gradient profile, we will introduce heparinase III (an enzyme which reacts very specifically towards HSPG) to digest the heparan sulfate side chains existing in ECM with the aim of removing the ECM binding domains for VEGF189. Then we will compare the time-dependent transport profile of VEGF189 under different experimental conditions and compare the results here with simulation as well.

3.2 Material and Methods

3.2.1 Protein labeling

Recombinant Human Vascular Endothelial Cell Growth Factor 189 (aa 27-215) from R&D Systems (catalog # 8147VE025CF) was labeled with Alexa Fluor^{TM} 594 dye using Alexa Fluor^{TM} 594 Microscale Protein Labeling Kit (ThermoFisher Scientific, catalog # A30008). We also labeled streptavidin (MilliporeSigma, catalog # S4762) using the same method. Lyophilized protein was reconstituted in PBS solution and the concentration was set to be 1 mg/ml, as suggested by the manufacture to be

a prerequisite for efficient labeling. Briefly, the reactive dye amount was calculated using the following formula and the manufacture's suggestion for the molar ratio (MR) for streptavidin and VEGF189 protein were 10 and 12, respectively.

$$\frac{[(ug\,\text{protein}/\text{protein MW}) \times 1000] \times MR}{12.2} = uL\,\text{reactive dye to add to sample} \quad (3.1)$$

in which we used 25 μg protein for both streptavidin (MW 52kDa) and VEGF189 (MW 42kDa) and the corresponding dye volume needs to be added are 0.39 μL for streptavidin and 0.59 μL for VEGF189. This small volume is very hard to pipette accurately so we instead diluted the reactive dye (from 12.2 nmol/μL) 4 times (which yields 3.05 nmol/μL) and the working dye volumn becomes 1.56 μL for streptavidin and 2.36 μL for VEGF189.

The protein solution (25 μL, concentration 1 mg/mL) and the calculated reactive dye (concentration 3.05 nmol/μL) were mixed together and pH-adjusted using sodium bicarbonate solution (2.5 μL , concentration 1 mol/L). The mixture was incubated at room temperature for 15 minutes.

To remove the unreacted dye and purify the conjugation, Bio-Gel P-6 resin (BIO-RAD, catalog # 1504134) was prepared in a Nanosep MF 0.2 μm centrifugation device (PALL, catalog # ODM02C33). The reaction mixture was transferred to the centrifugation device and centrifuged at 16000×g for 1 minute (Eppendorf 5417R). Labeled protein was collected in the collection tube and stored for further use.

The final protein and dye concentration was determined using Nanodrop 1000 (ThermoFisher Scientific) by measuring the absorption at 280 nm and 590 nm (A_{280} and A_{590}) and the protein molar concentration was determined by

$$\text{Protein concentration}(M) = \frac{[A_{280} - \text{correction factor} \times A_{590}]}{A_{280}\,\text{of protein at}\,1mg/mL \times MW} \quad (3.2)$$

in which the correction factor (the fluorophore's contribution to the A_{280}) used was 0.56 [87]. The A_{280} at 1mg/mL of a certain protein can be determined by

$$\varepsilon_{molar} = A_{280}\,\text{at 1mg/mL} \times MW \quad (3.3)$$

where ε_{molar} is defined as molar extinction coefficient at 280 nm and can be estimated via the protein's amino acid composition. We get ε_{molar} for streptavidin directly from literature, which is 41326 $M^{-1}cm^{-1}$ [101]. ε_{molar} for VEGF189 was estimated by the following formula [102]:

$$\varepsilon_{molar} = nW \times 5500 + nY \times 1490 + nC \times 125 \qquad (3.4)$$

where n is the number of each residue (W: tryptophan, Y: tyrosin, C: cysteine). For VEGF189, nW is 2, nY is 5 , and nC is 16 [103], which yields 29900 $M^{-1}cm^{-1}$.

Therefore the A_{280} at 1mg/mL used to calculate protein concentration after labeling is 0.78 for streptavidin and 0.71 for VEGF189.

3.2.2 Device fabrication

The device used in this set of experiment is a single unit from the simulation geometry in Chapter 2. The 2D geometry was generated in AutoCAD and the geometry and a photo of the device are shown in Figure 3-5:.

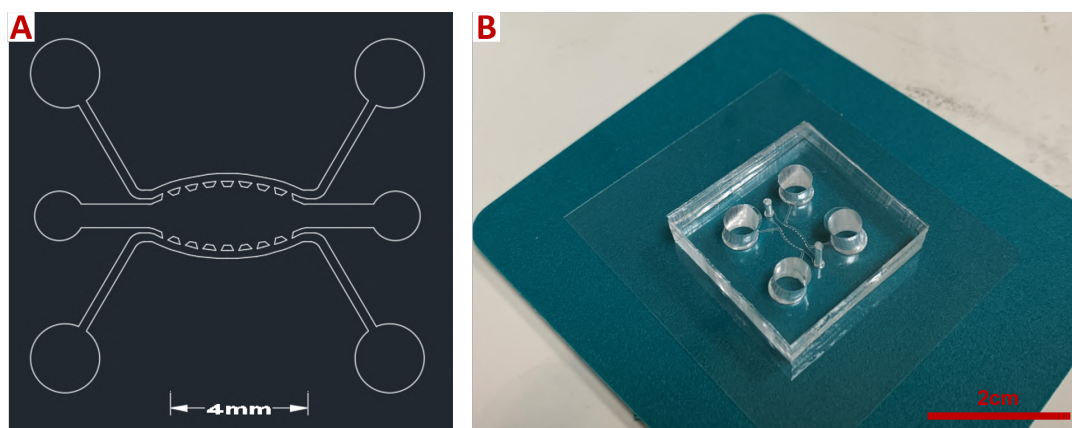Figure 3-5: A) Device 2D geometry. B) A photo of the device bonded on a coverglass.

In our experiment, we designed the desired 3D mold in SOLIDWORKS. We used the stereolithography service from Proto Labs Inc. and printed in 0.001-inch-thick layers (the actual channel height is 200 μm). A 10:1 PDMS ratio of elastomer to cross-linker (SYLGARD^{TM} 184 Silicone Elastomer Kit) was mixed, degassed and poured

into the mold. The PDMS was cured in an 80 °C oven for a minimum of 90 min. After peeling off the PDMS and punching holes for inlets and outlets, the device was plasma bonded to a clean coverglass (43mm x 55mm, NO.1, Thermo Scientific, catalog # 3329) using COVANCE plasma system (100W for 45s, Femto Science). After baking the bonded device at 80°C for 15 minute, ethanol (80% purity and 0.2 μm filtered) solution was manually introduced into the device for 5 minutes to sterilize the chambers. The device was washed with DI water for 5 times to remove ethanol solution and any residue. The device was stored in a sterile environment for later use. Importantly, we always use the device at least 24h after it was prepared and we will explain the reason in section 3.2.3.

3.2.3   Gel preparation

Matrigel® (Corning, catalog # 356231) was thawed overnight on ice in a 4°C fridge. Prior to the experiment, pipette tips and pipettes as well as the device were all pre-chilled in a -20°C fridge for 20 min. PBS solution which would be used to dilute the Matrigel® concentration by half was also pre-chilled on ice. After diluting the Matrigel® to the desired concentration, the device and other experiment supplies were taken out from the -20°C fridge and used immediately, as in experiment we found that strict control of the temperature helps increase the successful rate of gel loading, because low temperature also helps keep the gel viscosity low. A report has provided detailed analysis for the gel moving in the channel and pinning at the interface [104] and they also documented that viscosity played a crucial role in optimizing the interface between gel channels, with higher density hydrogels exhibiting higher viscosity and displaying an increased chance of leakage between adjacent channels. The other 2 critical factors in order to realize successful gel pinning include smaller gap spacing between posts and more hydrophobic surface. We followed these rules to prevent the gels from leaking into neighboring channels. For example, the device used was always prepared at least 24h ahead to allow for the PDMS hydrophobicity to recover after surface oxidization [105]. In our device design, we also tried to design a smaller gap spacing between the trapezoidal arrays in our device, but this was limited by the

resolution of our fabrication method.

Device was placed on ice and 8 uL gel solution was carefully pipetted into the device. The device was then put into a 37°C incubator. Matrigel® crosslinking occurs quickly at 37°C. After 15 minutes, the device was taken out and different desired solution was loaded in the 2 side channels.

3.2.4 Heparan sulfate digestion

Heparinase III (MilliporeSigma, catalog # H8891) was reconstituted in 100 μL PBS solution to yield 50 Sigma units/mL. Heparinase III was further diluted 4 times (which yields 12.5 Sigma units/mL or 0.02 IU/mL). Heparinase III solution was pre-chilled and mixed with equal volume of Matrigel®. The mixture was loaded into the device and incubated as described in section 3.2.3. The device was then kept in the incubator for 16h to allow for the digestion reaction to occur. After the digestion, labeled VEGF189 solution and plain PBS were introduced into 2 side channels, separately. Non-modified Matrigel® (but still diluted using the same buffer solution) served as the control.

3.2.5 Imaging

Images were captured on a Nikon microscope (Eclipse Ti-E) and a Texas Red™ filter cube set was used to capture fluorescent images. The images were captured at various time points and at each time point, a large image was scanned under 10x (4×5 field of view) via NIS Elements software. Typically 200ms or 500ms exposure time is able to obtain good signal-to-noise ratio in the images. Before introducing the fluorescently-labeled protein, the device (with gel in it) was always imaged using various exposure time durations in order to assess the influence of autofluorescence and to do the intensity normalization. The image intensity was normalized between the source channel and the gel autofluorescence intensity. The intensity was evaluated at a cutline. The cutline connects 2 edges of the gel (as shown in Figure 3-8A). The images were typically captured at T=0 h , T=1 h, T=3 h, T=5 h, T=7 h, T=9 h,

T=12 h.

3.3   Results and Discussion

3.3.1   Streptavidin transport experiment results

Streptavidin was chosen for the purpose of control experiment as it does not bind to HSPG in the ECM. Therefore, the time-dependent data from the streptavidin transport experiment corresponds to the case where only the Free and Porous Media Flow physics and the Transport of Diluted Species in Porous Media physics are solved (no reactions are involved). After inputting the diffusion coefficient of streptavidin in the simulation model, we can compare the simulation results and the experiment conducted in this section. To begin with, streptavidin was labeled successfully as determined by Nanodrop. As shown in Figure 3-6, the average of the A_{280} from 3 repeat measurements is 0.325 and the A_{590} from 3 repeat measurements is 0.311. After correcting for the dye's contribution to A_{280} as described in section 3.2.1, the protein and the dye concentration were determined to be 2.68 μM and 3.46 μM, respectively. The gel was loaded in the microfluidic device as depicted in section 3.2.3. The gel was successfully retained in the desired region with a clearly visible gel-air interface (Figure 3-7).

Before introducing the fluorescently-labeled protein, the device was imaged at various exposure times (100 ms, 200 ms, 500 ms and 1000 ms) to assess the effect of autofluorescence. The signal intensity evaluated at our specified cutline was plotted in Figure 3-8A. The labeled streptavidin solution was diluted 500 times and introduced into the source channel and pure buffer solution (PBS) was introduced in the sink channel (Figure 3-8A) and this time point is defined as T=0 h. The original intensity data from autofluorescence and data from T=1 h were also plotted (exposure time: 500 ms) in Figure 3-8B.

We are interested in how the intensity profile fits with the simulation data, so we first looked at T=1 h. To do this, we need to normalize the data from both
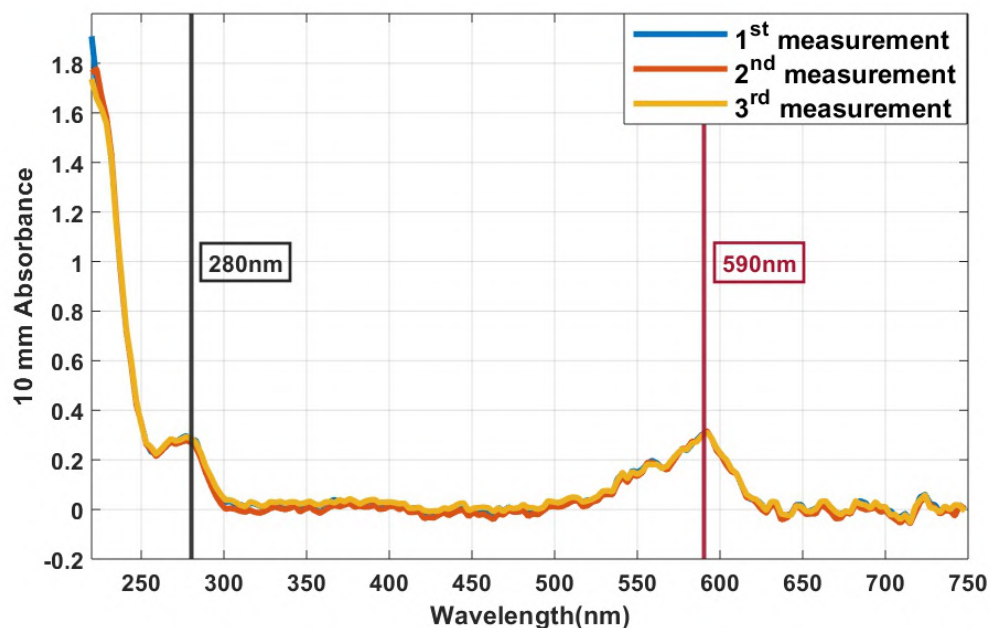
Figure 3-6: Streptavidin and dye concentrations determined by Nanodrop with two critical absorbance values at 280 nm and 590 nm.
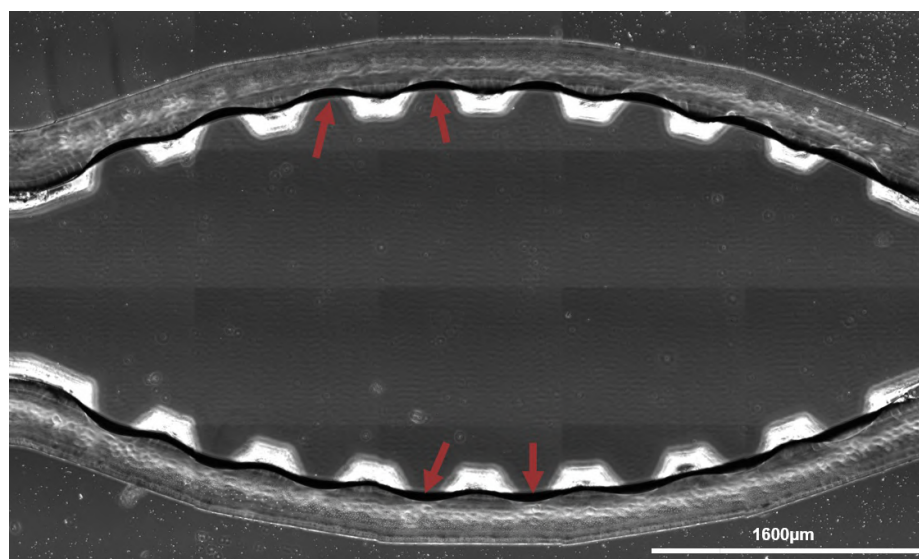
Figure 3-7: Gel loading into the microfluidic device with arrows pointing to the gel-air interface.

sources. Besides, to compare the results yielded from the simulation, we also changed the diffusion coefficient for streptavidin and re-did time dependant studies for the plain transport studies (no biochemical reaction was involved). The results from the simulation is plotted in Figure 3-9 along with the experiment data at T=1 h.

65
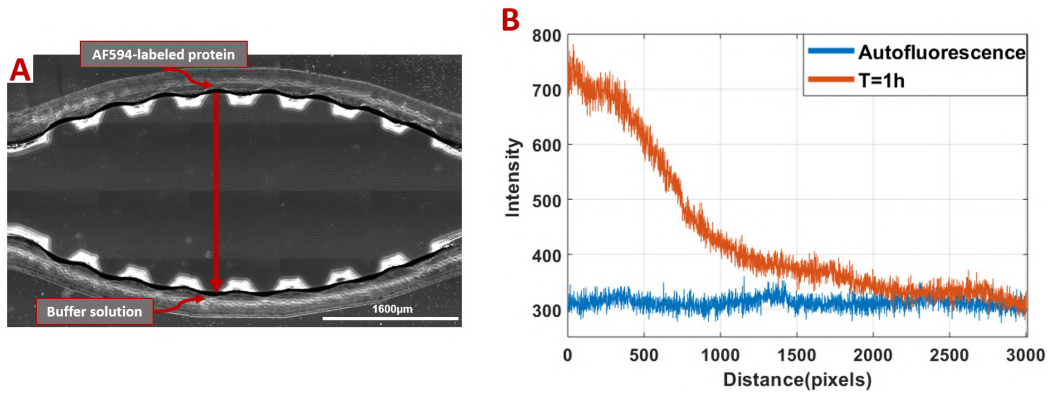
Figure 3-8: A) Signal intensity evaluation rule. B) Autofluorescence signal intensity and signal intensity at T=1 h. Intensity is not normalized.
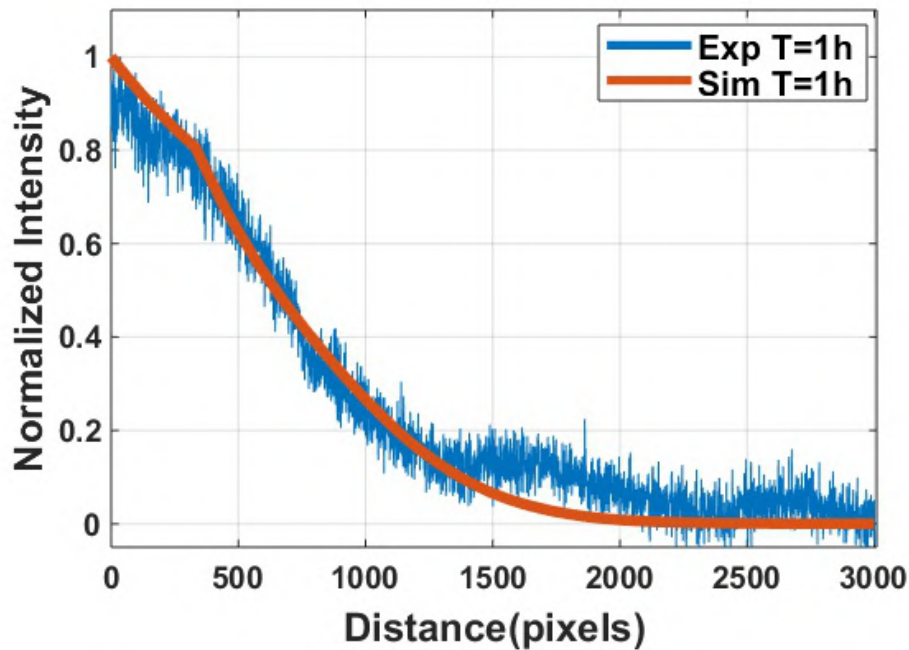
Figure 3-9: Normalized intensity profile for the streptavidin simulation and experiment at T=1 h.

From Figure 3-9, it is clear that the experiment data agrees well with simulation at T=1 h. Besides, not surprisingly, from the intensity gradient, a noticeable amount of streptavidin is able to transport into the gel in just 1 h. Then we took images at other time points (T=3 h, T=5 h, T=7 h, T=9 h, T=12 h) and the normalized image intensities are shown in Figure 3-10A.
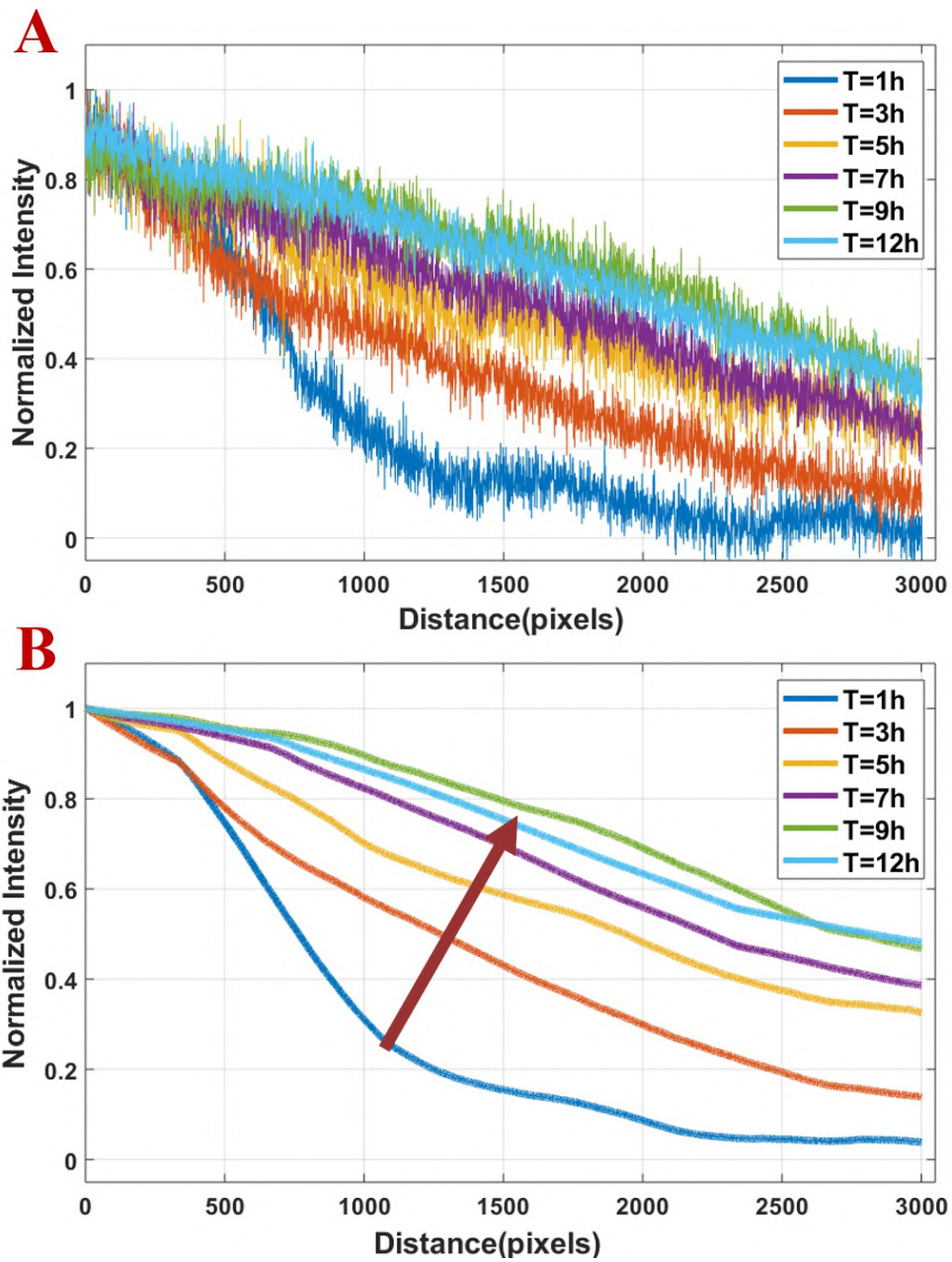
Figure 3-10: Normalized intensity profile for the streptavidin experiment from 1 h to 12 h. A) Raw data and B) Smoothed data for visualization with the arrow indicating the intensity evolution.
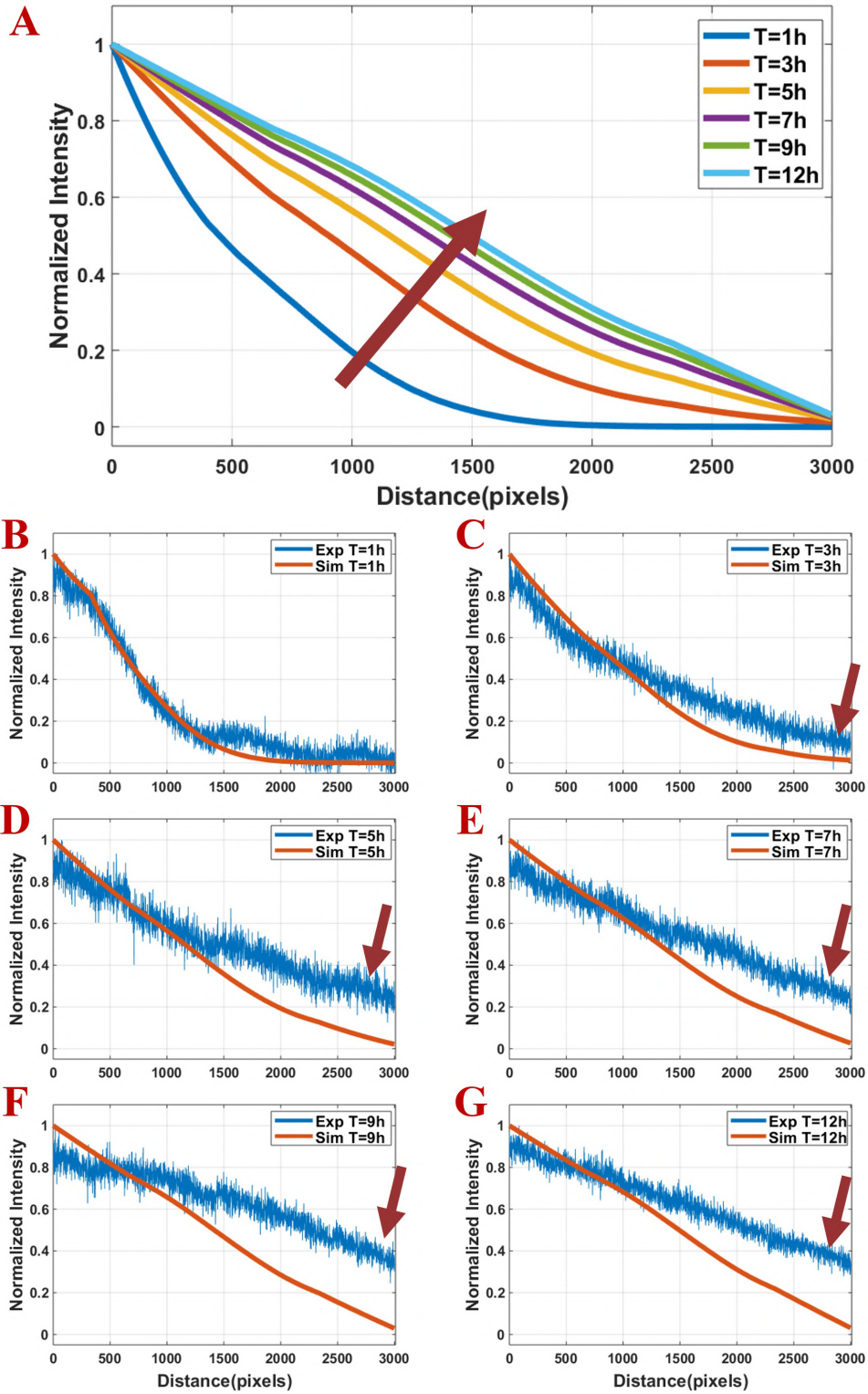
Figure 3-11: The streptavidin experiment and simulation data comparison for all time points. A) The streptavidin simulation data from 1 h to 12 h. Experimental and Simulation comparisons for B) 1 h, C) 3 h, D) 5 h, E) 7 h, F) 9 h, and G) 12 h. Arrows indicate the non-zero boundary condition in the experiment.

In Figure 3-11, we plotted the simulation data and compared simulation and experimental data for every time point. As noticed from Figure 3-10 and 3-11, the intensity near the buffer channel does not stay at zero in our experiment and only the 1 h and 3 h experimental data agree well with the simulation. This is possibly due to our experiment strategy. In simulation, as shown in Figure 2-6, the VEGF concentration at the low-concentration (LC) channels is set to zero and an infinite convective flow is needed to maintain the boundary condition. However, we simplified the experiment and used static incubation therefore there is no constraint for the boundary condition (the zero concentration) in the experiment. As a result, streptavidin molecules go through the whole gel and raise the fluorescence intensity value at the very end of our evaluation line.However, this is also the key information (and expected) from this experiment: AF-594 labeled streptavidin can easily go through the gel and form a linear intensity profile in as quick as 3 h (within 12 h) when there is no ECM-binding involved in the transport (consistent with the simulation). This serves as a control for our later VEGF189 experiment when the protein binds strongly to the ECM.

3.3.2   VEGF189 transport experiment results

We followed the same steps to label VEGF189 as described in section 3.2.1. Matrigel was prepared using the same procedure as section 3.3.1. After incubating the gel for 15 minutes, the AF594-labelled VEGF189 protein solution was pipetted in one side channel while PBS solution was pipetted in the other side (same as Figure 3-8A). Then images were taken at T=1 h, T=3 h, T=5 h, T=7 h, T=9 h, T=12 h. What should be noted is that, we won't be able to differentiate if the fluorescence is coming from free VEGF form or matrix-bound VEGF, so we changed the readout from the simulation. For VEGF189 experiment in this section and section 3.3.3, all simulation results were re-evaluated to give bound form plus free form. Similarly, the normalized intensity profile at various time points are shown in Figure 3-12. There is a substantial qualitative difference of this data as compared to Figure 3-10. First of all, the intensity profile implies a slow transport dynamics, which remains consistent with the simulation (Figure 3-13). In simulation, 12 h only allows VEGF189 to penetrate

25% of the evaluation line. In experiment, approximately 25% of the evaluation line is experiencing an noticeable intensity (normalized intensity > 0.1) while the intensity of rest 75% is within 0.1. In contrast, from Figure 3-10, 12 h allows the whole radial distance penetrated and the minimum normalized intensity at 12 h is 0.35. This clearly demonstrates that the VEGF189 is not able to diffuse deep into the gel.
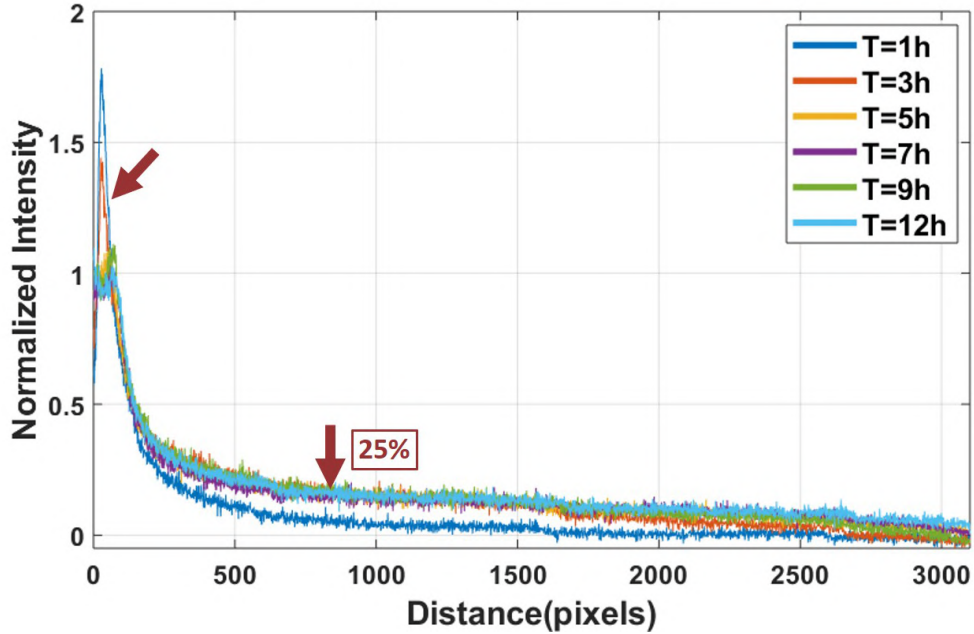
Figure 3-12: Normalized intensity profile for the VEGF189 experiment from 1 h to 12 h. Left arrow indicates the intensity focal region near the VEGF source.

Due to the minimal changes in the intensity profile, we picked 2 extreme time points (T=1 h and T= 12 h) and did the overlay for them (Figure 3-14). The data shows that at 1 h, for both experiment and simulation, only 15% of the specified line is having non-zero VEGF189 concentration. At 12 h, both data suggest that 25% of the specified line has a sharp VEGF gradient. From the experiment data, we observed another slight gradient (the right arrow in Figure 3-14) which causes the experimental intensity to be larger than the simulated intensity. We suspect that this is due to the existence of a small amount of free dye in the conjugation which can be transported freely.

What should also be noted is that the experimental intensity profile has some "spikes" near the source channel (Figure 3-15). We speculate that this spike is due
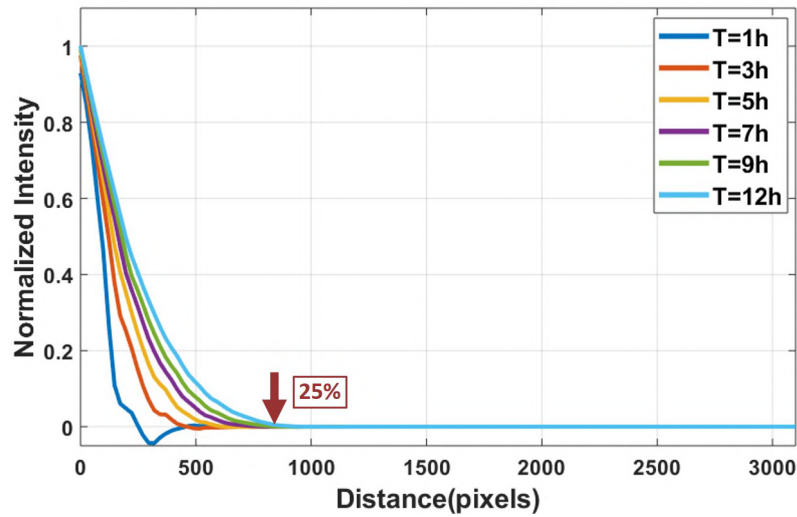
Figure 3-13: Normalized intensity profile from the VEGF189 simulations from 1 h to 12 h.
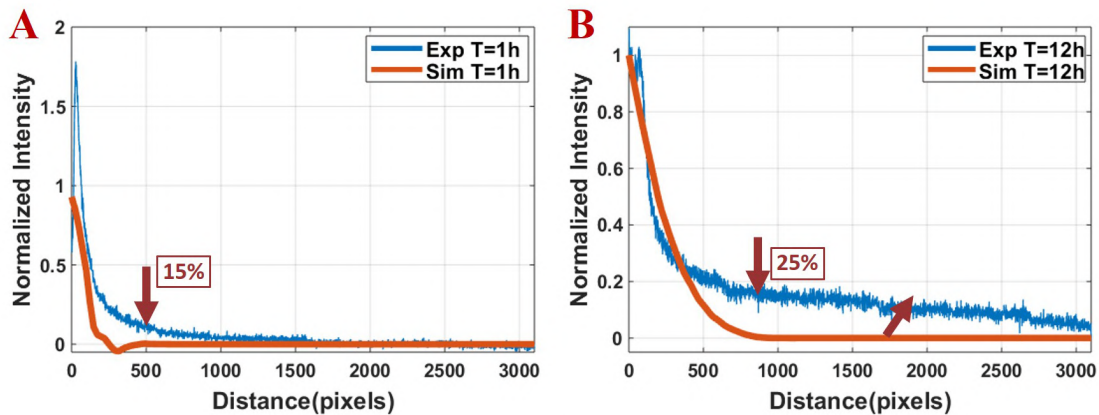
Figure 3-14: VEGF189 simulation and experiment data comparison for A) T=1 h and B) T=12 h.

to the air-gel interface, which is not captured in the simulation. In simulations, the gel has very smooth edges, but in the experiments, the edges actually have a wavy structure as shown in Figure 3-7. We can look at the actual experiment images right at this interface, which are shown in Figure 3-16. From these images, we can also find that within 12 h, the bright region of fluorescently labeled protein is diffusing into the gel, albeit slowly, with the rest of the gel being completely dark. This is the expected outcome if the protein binds very strongly with the ECM. In contrast to this, for a protein which does not bind to the ECM such as streptavidin, we have shown that it

71
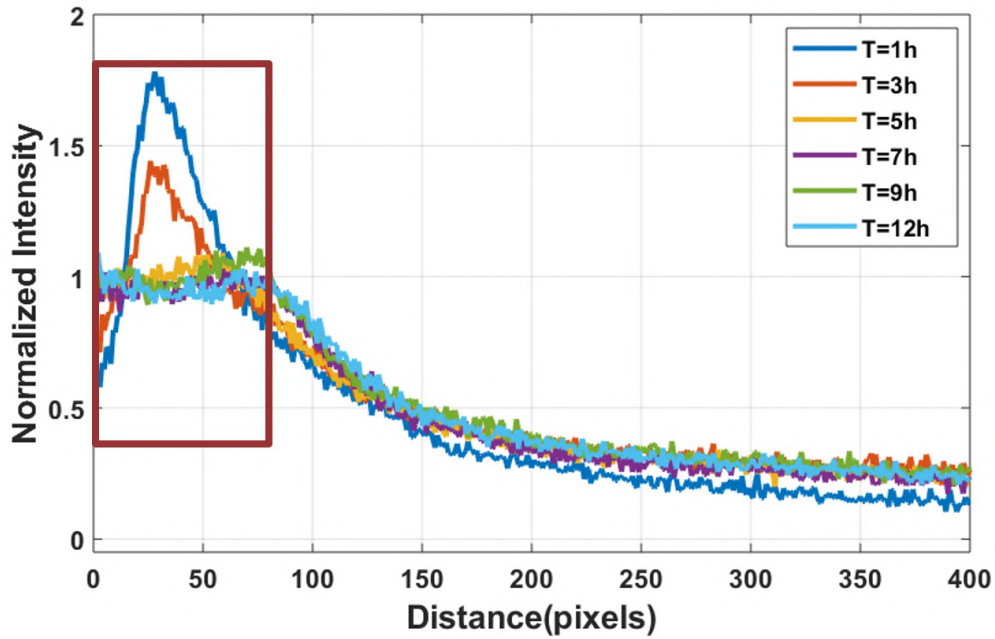
Figure 3-15: Zoom-in version of Figure 3-12, highlighting the intensity profile near the source channel.
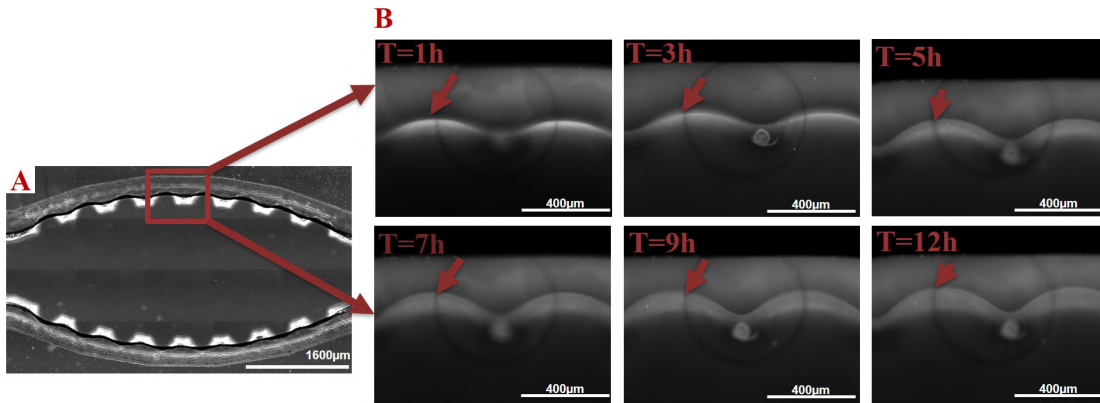
Figure 3-16: Images captured at the gel-liquid interface[1] at B) various time points after loading the fluorescently-labeled protein with arrows indicating the bright focal region. A) The capture FOV.

establishes a gradient across the whole specified line as quickly as 3 h (Figure 3-10). Whereas for VEGF189, approximately 25% of the line is experiencing a noticeable intensity (normalized intensity > 0.1) and consequently a 4 times steeper gradient while the normalized intensity of rest 75% is within 0.1. This drastic difference illustrates the significant impact on gradient profile that ECM binding reaction could

exert. If ECM binding exists during transport, it alters both the range and the gradient magnitude of the target protein in a time-dependent manner.

3.3.3   Heparinase III digestion experiment results

In chapter 3.3.2, we have shown that VEGF189 transport into Matrigel is reduced as compared to streptavidin. Based on our hypothesis, this is due to the high affinity of VEGF189 binding with HSPG in the ECM. To test this hypothesis, we used heparinase III to pre-digest the HSPG in the Matrigel® before introducing the fluorescently labeled protein solution. The resulting intensity profile is shown in Figure 3-17. We are only showing T=1 h and T=12 h because the rest time points lie between them and are too close to each other. Although we expect the result here to be the same as Figure 3-10 if the HSPG is completely removed, we observed a profile which is between Figure 3-10 and Figure 3-12. The plausible cause will be discussed in later part of this section.
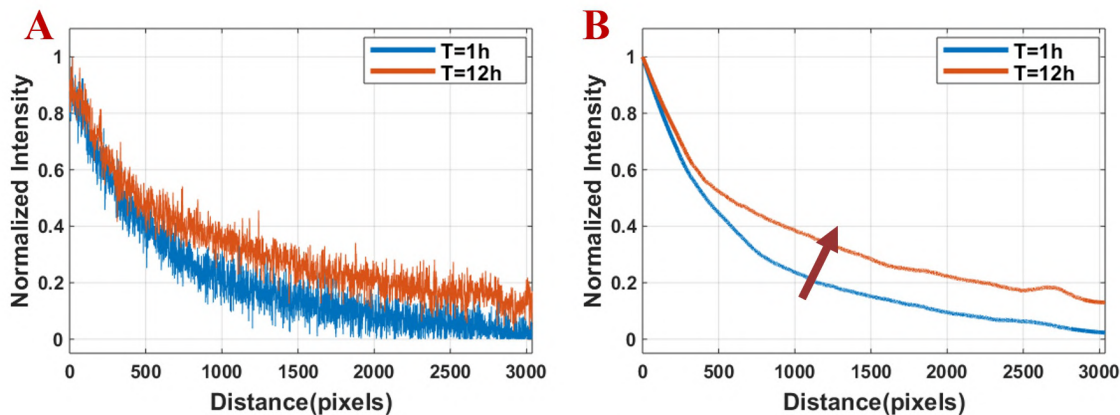
Figure 3-17: Normalized experimental intensity profile after pre-treatment with heparinase III. A) Raw and B) Smoothed data to show the trend.

One thing should be noted is that. In our VEGF189 experiment, we noticed a bright focal region near the interface, which indicates a strong binding reaction between VEGF189 and the gel. However, after we treated the gel with heparinase III, we no longer observe the strong signal accumulation in that region, which is also the evidence that HSPG is reacting with VEGF189 (Figure 3-18).
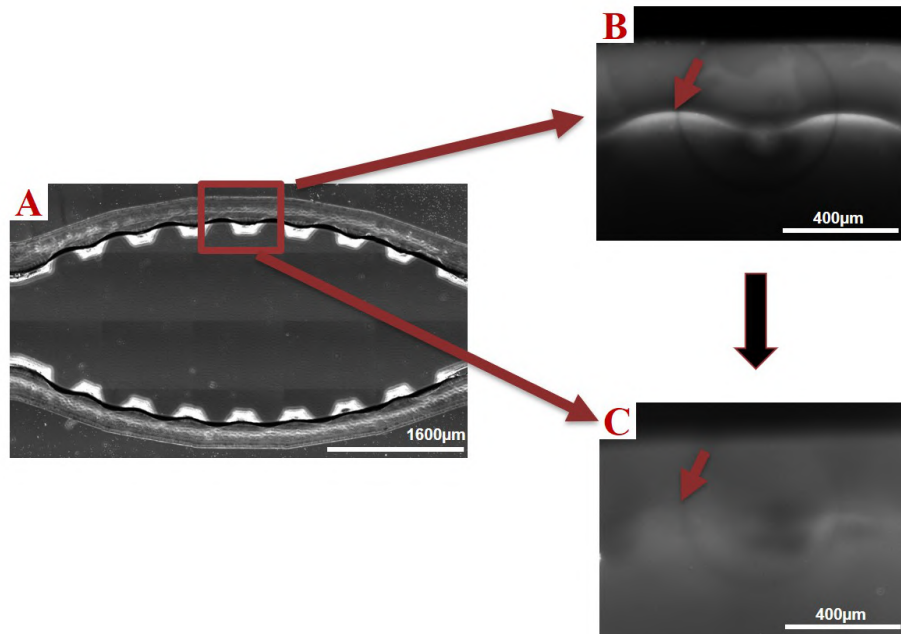
Figure 3-18: Comparison of heparinase III treatment with no treatment at the gel interface[2]. A) Imaging FOV. B) The gel is not treated. C) The gel is treated with heparinase III. Arrows pointing to the gel-liquid interface. T=12 h when images were captured.
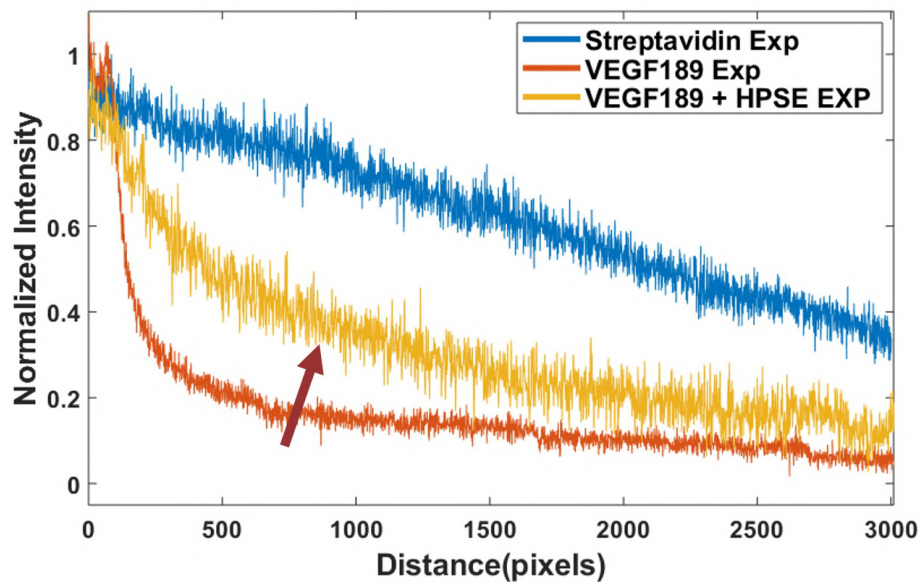
Figure 3-19: Comparison for all 3 cases. Heparinase III treatment (yellow) is changing the VEGF189 profile (orange).

In Figure 3-19, we are showing the normalized intensity profile for all 3 cases: 1) Streptavidin experiment when no ECM binding is expected. 2) VEGF189 experiment
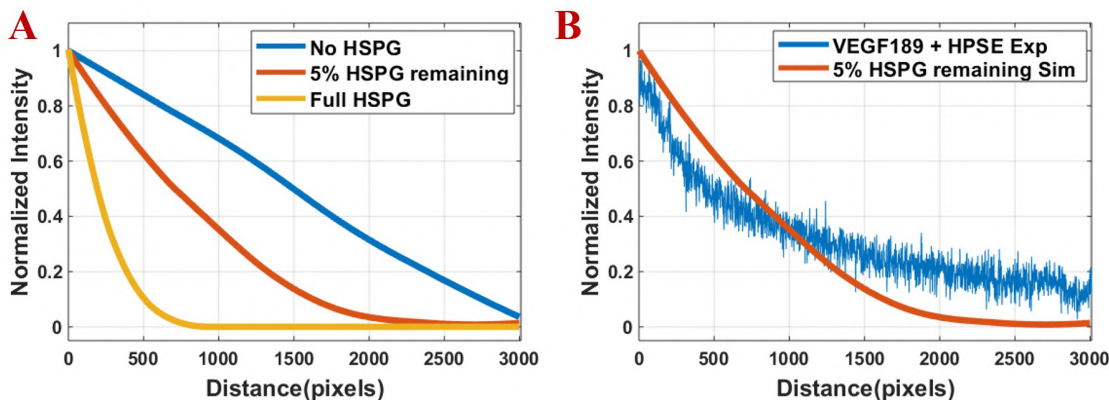
Figure 3-20: A) Simulation data when different degree of HSPG is present. B) The comparison between the simulation data when 5% HSPG is remained and the heparinase III experiment data.

and a strong binding reaction is supposed to happen between VEGF189 and HSPG. 3) The ECM was reacted with heparinase III to remove the binding cites before introducing VEGF189. The important message here is that the heparinase III digestion is changing the profile to a noticeable amount (Figure 3-19), although the heparinase III digestion experiment does not completely restore the concentration profile to a profile that is similar to section 3.3.1. One possible reason is that the HSPG in the gel was not completely digested. In our simulation, if we only let 5% of the original HSPG remain, the normalized VEGF189 profile is still not able to reach a linear profile after 12 h (Figure 3-20A). Furthermore, the images captured at the interface also demonstrate that the heparinase III is changing the VEGF189 binding behavior by making it no longer having a narrow bright band (Figure 3-18) right near the interface, which is also the VEGF source.

In brief, both the intensity data and the imaging at the interface indicate that the heparinase III treatment is effective at removing HSPG (although this might not be complete due to the abundance of HSPG in the ECM as we discussed in section 2.3.2) and allows more VEGF189 to enter the gel.

3.4 Conclusions

In this chapter, we investigated different cases of protein transport which yields valuable information for us to understand the VEGF profiles. Streptavidin is served as a control and the transport of streptavidin demonstrated that it could penetrate through the whole gel area in as quick as 3 h. In contrast, VEGF189 fluorescence intensity was retained mainly near the VEGF189 source, with a large percentage (75%) of the evaluated length remained close to the basal fluorescence level (normalized intensity within 0.1). Our simulation from Chapter 2 also predicted similar VEGF189 profile.

Based on our hypothesis, the existence of HSPG molecules in Matrigel® contains VEGF binding domains. We employed a lyase which could digest the binding domain specifically, in theory. We observed clear difference in the intensity profile after the lyase treatment as compared with no digestion. However, it was not able to fully bring it back to a linear intensity profile. It was postulated that HSPG was not completely digested and even a small portion of remaining HSPG could alter the VEGF189 concentration profile.

HSPG binds to large number of different proteins [106]. Therefore, not just for VEGF189, careful examination of the concentration profile is necessary when the distribution of the target protein in the microfluidic device has a significant effect on the experimental outcome. Using non-binding canonical molecules of similar molecular weight is not sufficient to reveal the important biochemical message behind it. Through experiments in this chapter, we also partially validated our simulation model in Chapter 2. As we will use our simulation model to perform optimization work for device design, the work here also builds our confidence on keeping using our simulation model.

Chapter 4

Preliminary Experiments for the Proposed System

4.1 Introduction

The development of our open-well system for engineering the blood brain barrier requires efforts in fabricating and characterizing the device as well as establishing BBB cultures *in vitro*. In this chapter, we will discuss the preliminary experiments towards these two aspects. On one hand, we investigated the method for the device bonding and achieved both quick and reliable results. On the other hand, we also performed vasculogenesis assay and observed capillary network formation in a microfluidic device. Once we have a fully functional and well-characterized device prototype, we will integrate these two aspects and perform further optimization work on the system.

4.1.1 Vasculogenesis and anastomosis

As discussed in Chapter 1, various methods have emerged for creating perfused vessels in microfluidic OOC systems. For our proposed system, we will use the "biology-directed" vasculogenesis method. This chapter demonstrates our initial efforts in realizing vascular network formation in a microfluidic channel. Cells were pre-encapsulated in the gel and loaded into the chip. By properly designing the

channel width and the spacing between the trapezoidal pillar array and control the surface properties of the device, and the viscosity of the hydrogel precursor solution as we talked in detail in section 3.2.3, the surface tension between the gel and air successfully pins the gel without leaking into the neighboring channels. To perfuse the formed vasculature and better mimic the vasculature *in vivo*, a common strategy is to line a monolayer EC in the neighboring channels and stimulate the fusion of cells near the interface via growth factor or/and flow [107] (Figure 4-1). This process is also called anastomosis. Anastomosis is a complex multistage process requiring cell contact, polarization, and apical membrane invagination [108] and it has been demonstrated in various microfluidic assays [107, 109].
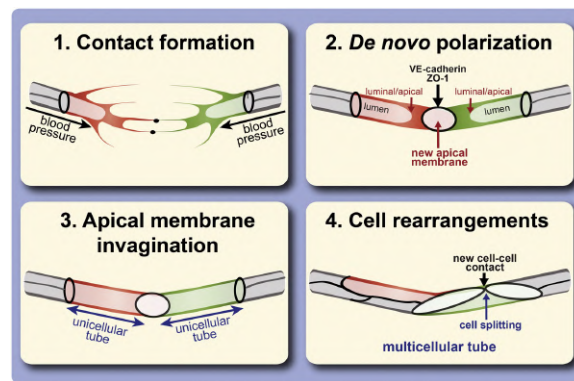
Figure 4-1: Multistage process during EC anastomosis. Reproduced with permission from [108].
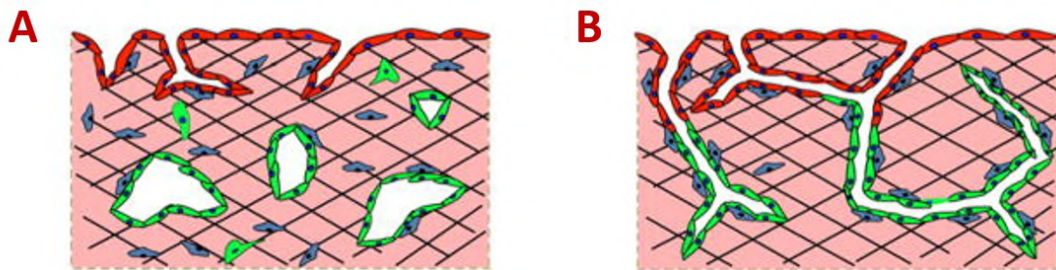
Figure 4-2: Anastomosis realizes the interconnection of the monolayer EC and the 3D EC network. Reproduced with permission from [110].

Sprouts formed by angiogenesis from an endothelium and tubes formed by vasculogenesis in the bulk of a 3-D matrix has been shown previously [110]. It leads to an intact and perfusable microvascular network which may have great usage in studying

the barrier properties of 3D vascular networks, and serve as a physiological system to deliver nutrients to other cells/tissues cocultured in the 3D scaffold. Therefore, in our assay, after formation of the capillary network inside the gel chamber via vasculogenesis, the adjacent microfluidic channels were then seeded with EC suspension. EC settles down and forms an intact monolayer and lines the whole channel. We will observe how these neighboring cells interact with each other.

4.1.2 Bonding of thermoplastics to PDMS

Our proposed system requires 3D culture of cells as well as fabrication of a hybrid device composed of different material (polystyrene and PDMS). Although PDMS can readily bond substantially with other silicon-based material such as glass, silicon wafer by simple surface oxidation and thermal curing, its ability to form robust and irreversible chemical bonds with non-silicon-based material such as thermoplastics and metals remains limited [111]. Compared with glass and silicon, thermoplastics offer several advantages including manufacturability, low-cost, and biocompatibility. However, PDMS has superior properties when fabricating microvalves. Therefore the bonding of silicon-based PDMS with non-silicon-based substrates could be beneficial in many ways as you can integrate benefits of both material. Therefore, various methods have been developed to realize the bonding. One report spin coated a silica sol (obtained by oligomerizing tetraethoxysilane monomers) on a thermoplastic plate and further polymerized to form a thin silica layer. The silica-coated surface could be covalently and strongly bonded with an plasma-activated PDMS [112]. This method involves slow curing at high temperature. Another group introduced a facile room temperature strategy, but it requires surface treatment of both surfaces by different chemicals ((3-aminopropyl)triethoxysilane (APTES) for thermoplastics and [2-(3,4-epoxycyclohexyl)ethyl]trimethoxysilane (ECTMS) for PDMS) [113]. Another instantaneous method for bonding was developed and it was mediated by one-step chemical modification using a mercaptosilane at room temperature [114].

Although all these bonding strategies appear very different at a first glance, all these mentioned bonding strategies have one similarity—they all utilized certain silane
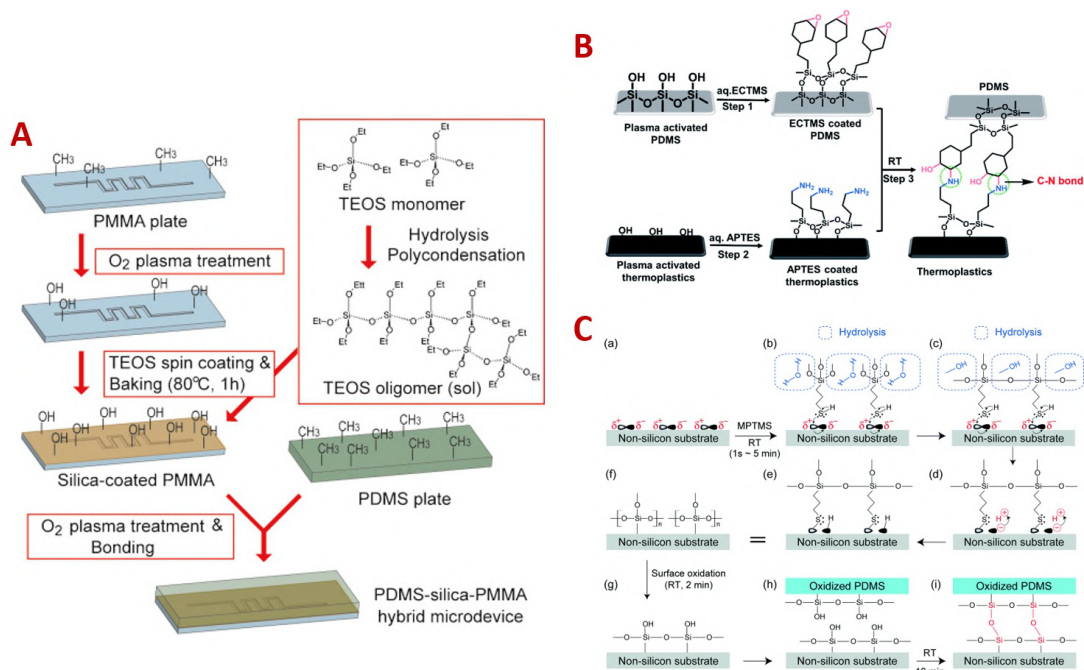
Figure 4-3: Various bonding methods. A) One method which requires high temperature curing. Reproduced with permission from [112]. B) One strategy applied separate linker molecules on both surfaces. Reproduced with permission from [113]. C) An instantaneous room temperature bonding mediated by a mercaptosilane. Reproduced with permission from [114].
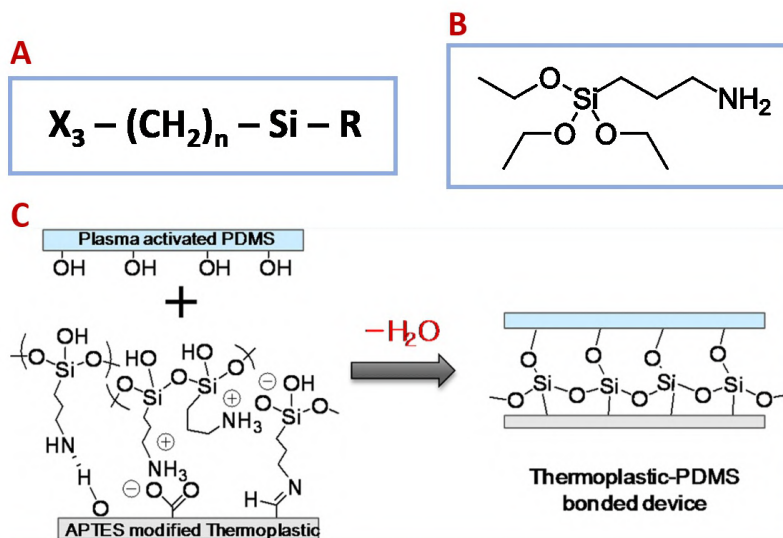
Figure 4-4: A) General formula of a silane molecule. B) Silane molecule used in our device fabrication. C) Principle of APTES-mediated bonding between thermoplastics and PDMS. Reproduced with permission from [115].

molecules as the linker or coupling reagent in between the two substrates. Silane is a large group of molecules and its general formula typically shows two classes of functionality (Figure 4-4A). X is a hydrolyzable group typically alkoxy, acyloxy, halogen or amine. Following hydrolysis, a reactive silanol group is formed, which can condense with other silanol groups to form siloxane linkages. The R group is a nonhydrolyzable organic radical that may posses a functionality that imparts desired characteristics [116]. In our case, we utilized APTES as it has been shown to bond with a variety of thermoplastics surfaces [115].

4.2   Material and Methods

4.2.1   Cell encapsulation in gel

Matrigel® (Corning) and other experimental supplies were prepared and temperature controlled similarly to what we've described in section 3.2.3. Device fabrication followed the same method as section 3.2.2. The device was adapted form an earlier idea [14]. Confluent iPSC-BEC was kindly provided by MIT Tsai Lab (Department of Brain and Cognitive Science). Cells were disassociated using TrypLE™ Express Enzyme (1X) (ThermoFisher Scientific, catalog # 12604013) and centrifuged at 1000 rpm for 5 min. The cell pellet was re-suspended in complete astrocyte medium (SciCell) supplemented with 20 ng/ml VEGF-A. The cell suspension concentration was prepared as either 12×10^6 cells/mL or 6×10^6 cells/mL. After very gentle mixing of equal volume of cell suspension (pre-chilled on ice) and Matrigel®, the device and other experiment supplies were taken out from the -20°C fridge and used immediately. Device was placed on ice and 15 μL cell-laden solution was carefully pipetted into the device. The device was then put into a 37°C incubator for 15 min. After that, the device was taken out and complete astrocyte medium was loaded in the 2 side channels.

4.2.2   iPSC-BEC direct seeding in a microfluidic channel

To coculture a monolayer EC in 2 neighboring channels, after we took out the solidified cell-laden gel from the incubator, laminin (1 mg/mL, ThermoFisher Scientific, catalog # 23017015) was introduced through the loading port to coat the inner surface of the side channels for 15 minutes, which serves as the basement membrane. This is a necessary step before loading the BEC suspension as it helps the BEC attach to the surface. In some other studies, it has also been shown that laminin coating helps EC migration outward from the tissue chamber during vasculogenesis [107].

We also did a simple perfusion experiment while the monolayer cells are present. To perfuse these cell, we blocked 2 ports via homemade plugs and the inlet was connected to a syringe pump and flow rate set to 5 μL/min, which corresponds to a velocity of 26.7 mm/min in the microfluidic channel and a shear stress of 0.15 dynes/cm^2 acted on the EC. We observed proliferation rate of BEC at different locations in the channel.

4.2.3   Bonding of polystyrene plate and PDMS

A 95% ethanol solution (v%) was prepared in DI water in a large crystallizing dishes (diameter 190 mm to fit in a wellplate). APTES (MilliporeSigma, catalog # 440140) was then added to yield a final 2% (v%) concentration. Once the APTES is added, the time was recorded as T=0. The solution was stirred briefly then let it sit at room temperature for 5 min (hydrolysis happens during this time). We also tried longer hydrolysis time but it didn't improve the bonding quality. At T=1 min, a bottomless 96 wellplate (GREINER BIO-ONE, catalog # 655000-06) was put into a plasma cleaner and treated at 200W for 30s (Femto Science). At t=5 min, the plate was taken out and immediately put into the dish with APTES solution. At t=7 min, the plate was taken out and washed for 30 seconds using ethanol solution to remove any excess APTES and dried under room temperature. At t=8 min, a thin PDMS sheet was plasma treated at 100W for 45s (Femto Science) and then brought into contact with the APTES-treated plate. We also found curing the APTES layer on

the thermoplastic plate is not necessary, which helps speed up the whole bonding process.

4.3 Results and Discussion

4.3.1 iPSC-BEC vascular network formation in a microfluidic device

After successfully loading the cell-laden gel and subsequent media on both sides, the microfluidic device is properly kept and imaged every 24 h or 48 h. The comparison between 2 seeding densities are shown here (Figure 4-5). For the high seeding density case $(12 \times 10^6$ cells/mL) , BEC started to show very clear network structure beginning on day 5. In contrast, for the low seeding density $(6 \times 10^6$ cells/mL), the cells were less interconnected and their morphology also displayed very irregular perimeter which might be an indicator of cell stress. From this experiment, we get a better sense of the right seeding density which will promote the vasculogenesis process. We also learned the time dynamics of this process, which will facilitate the process of more complex cell/tissue culture on our proposed system in the future.

4.3.2 Integrating iPSC-BEC vasculogenesis and lining in a microfluidic device

Besides vasculogenesis, to realize direct perfusion of the formed 3d vascular network, the vasculature in the 3D culture region needs to form a tight connection at the interface with the EC monolayer in the perfusion channels (Figure 4-6A W1). Therefore, we also performed the EC lining experiment in the neighboring channels after the 3D culture is initiated.
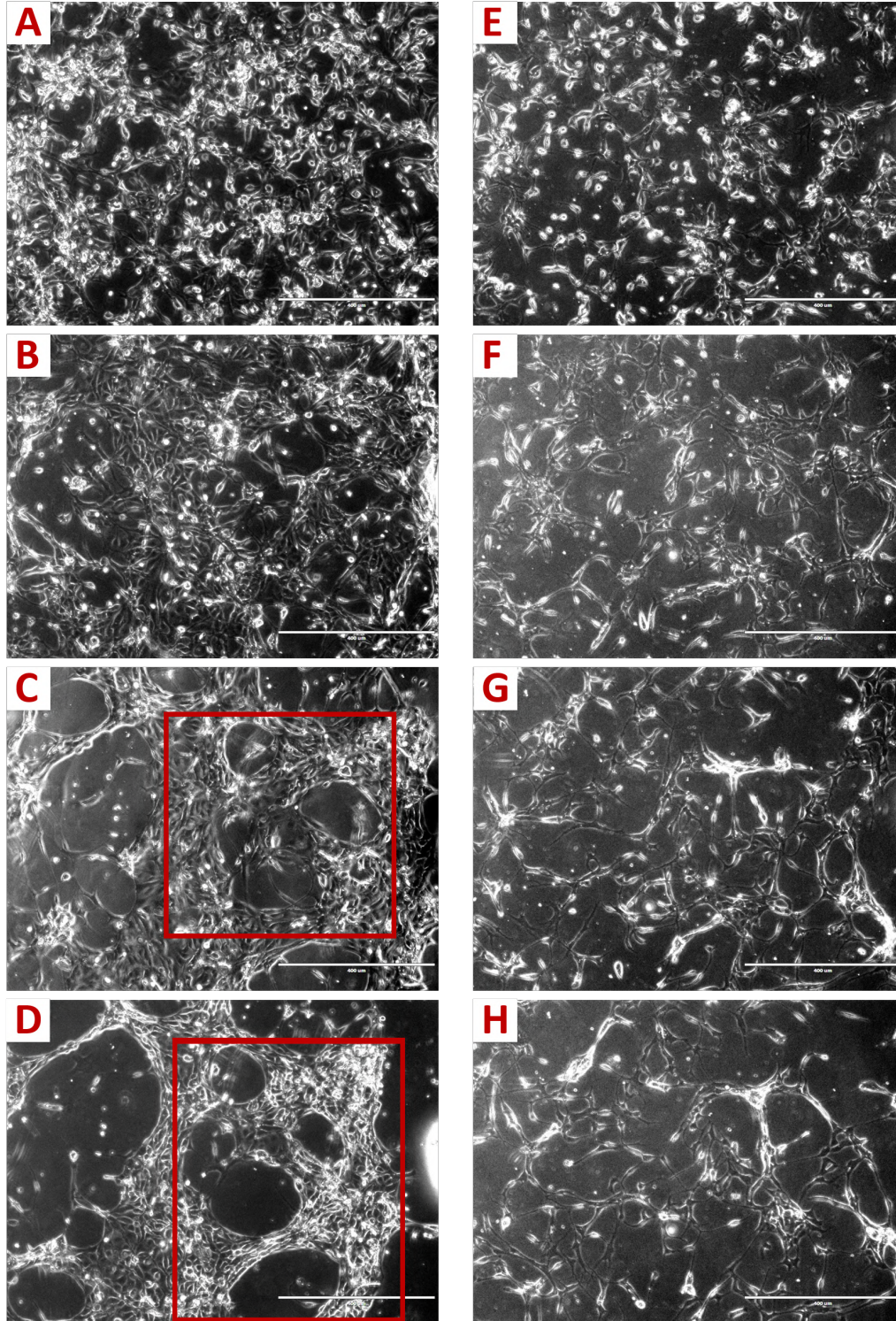
Figure 4-5: Comparison of 2 different seeding densities for iPSC-BEC vasculogenesis with the network structure highlighted in red. A) Day 1 B) Day 3 C) Day 5 and D) Day 7 after high-density seeding. E) Day 1 F) Day 3 G) Day 5 and H) Day 7 after low-density seeding with seeding day being day 0. Scale bar: 400 μm.
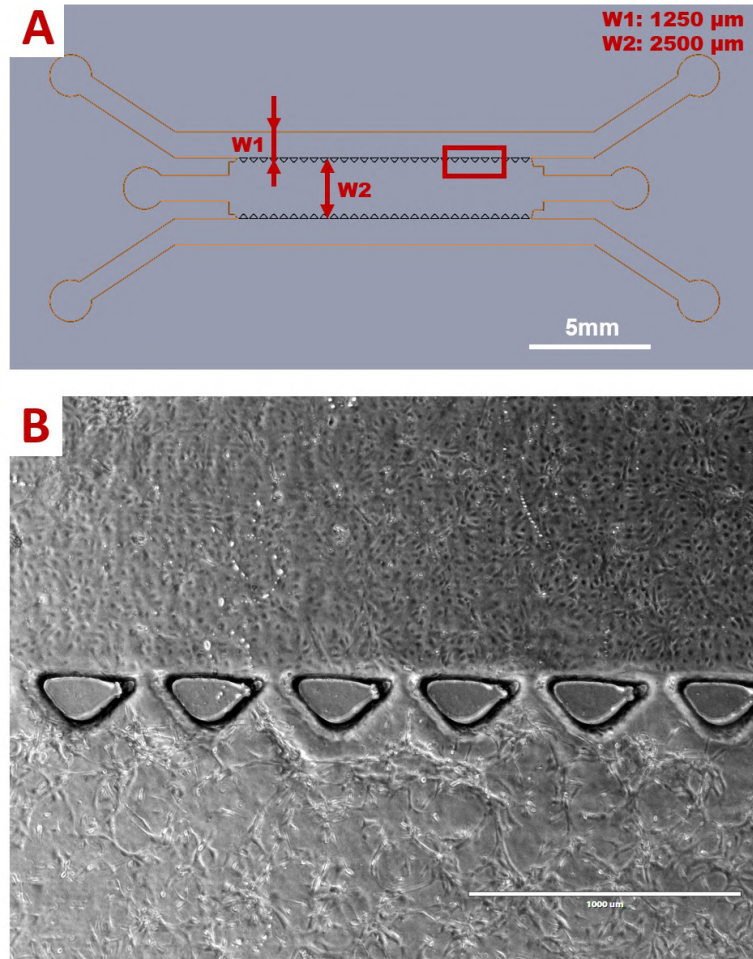
Figure 4-6: A) The device we used in this experiment and its key dimensions. The image was taken at the specified FOV. Scale bar: 5 mm. B) Image at this FOV showing the successful attachment of a confluent EC monolayer in the side channel as well as 3D vasculature structure in the center gel channel. Image was taken 24 h after seeding. Scale bar: 1000 μm.

As shown in Figure 4-6B, there is an intact monolayer BEC layer in the neighboring channel of the 3D vasculature channel. We further incubated the device with daily media change and imaging. After 48 h, we observed some BEC extending longer branches in the 3D channel to the monolayer channel. However, as a control, when the monolayer is not present, this behaviour and morphology is not observed. The trapezoidal posts array region usually has few cells.

We also did a simple perfusion experiment and our main observation target is the BEC-lined channel. The perfusion strategy is shown in Figure 4-8. 2 ports were

blocked and the theoretical flow direction is also shown in the figure. Point 1 is more affected by the flow as it is right near the inlet. We images at both point 1 and point 2 after 5 days of perfusion (flow rate: 5 μL/min, which corresponds to 0.15 dynes/cm^2 acted on the EC layer).
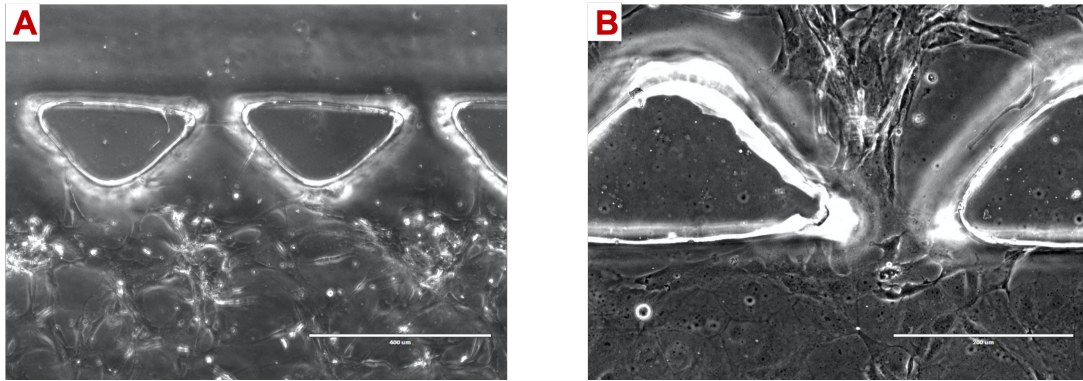
Figure 4-7: A) Control experiment without monolayer on the side. Scale bar: 400 μm. B)Monolayer BEC is present in the neighboring channel. Scale bar: 200 μm.
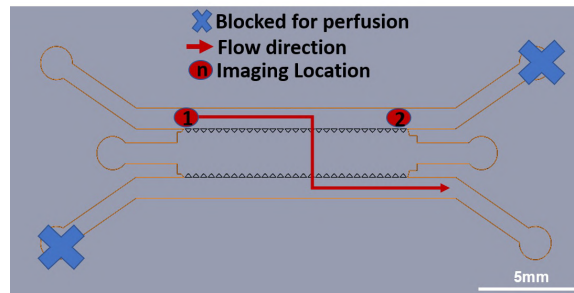
Figure 4-8: Perfusion strategy with 2 imaging locations

For each imaging points, there were 2 focus (channel bottom and channel ceiling). In Figure 4-9, A and C were from point 1, bottom and ceiling, respectively. B and D were from point 2, bottom and ceiling, respectively. Since cells at point 1 are experiencing a slow flow rate, it has a high proliferation rate so both A and C are more confluent than B and D. As a control, we can also show a monolayer morphology in which the device was kept under static incubation for 5 days with daily media change (Figure 4-10). It is obvious that such a slow flow rate perfusion results in a more confluent monolayer than our control experiment (Figure 4-10), which is the expected behaviour for endothelial cells and we have also observed similar behaviour
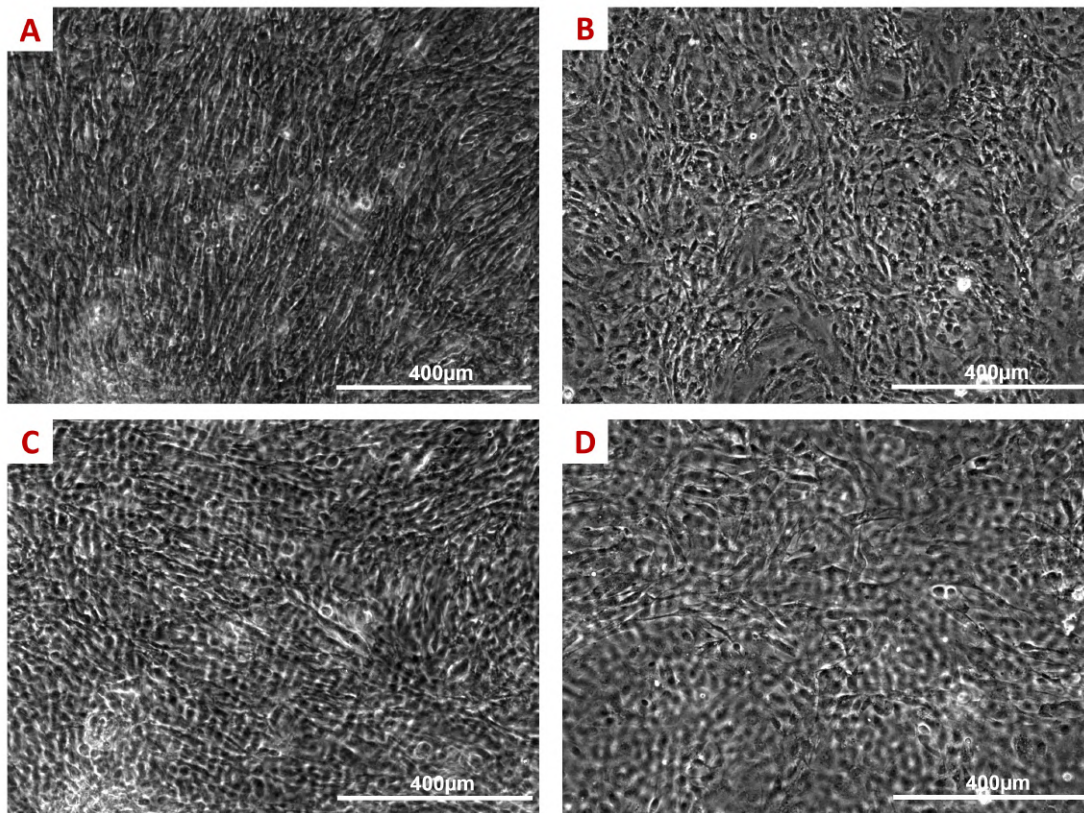
Figure 4-9: iPSC-BEC different proliferation rates at different points A) Device bottom at point 1. B) Device ceiling at point 1. C) Device bottom at point 2. D) evice ceiling at point 2. Scale bar: 400 μm.
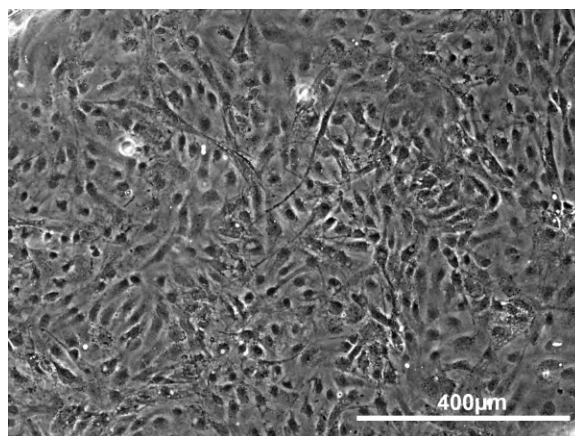
Figure 4-10: iPSC-BEC monolayer morphology after 5 days of static incubation with daily media change. Scale bar: 400 μm.

with HUVEC before. This simple perfusion experiment is an initial test on how to set up perfusion when there are multiple channels with gel in it as we ultimately want

to perfuse our gel culture system in a high throughput manner.

4.3.3 Bonding of polystyrene plate to PDMS

Bonding of the polystyrene plate and PDMS is one critical step in the fabrication of the proposed device. We investigated the silane-based bonding strategy and optimized the choice of the silane type, the reaction parameters such as the chemical treatment duration, the oxidization power and duration and the post-curing necessity. Eventually we are able to obtain a strong bonding between these 2 layers. The bottomview of the bonded polystyrene plate and PDMS layer is shown in Figure 4-11. We usually perform a peeling-off test to assess the bonding stability between layers. PDMS layer coming off completely usually indicates reversible and bad-quality bonding. We performed a peeling-off test for the device shown here. The red outline displays the effective bonding area. From the image, a large portion of the PDMS material (compared with the total outlined area) remained attached to the the plate bottom with only some PDMS on the edge being peeled off. Empirically, this is a sign of reliable bonding.
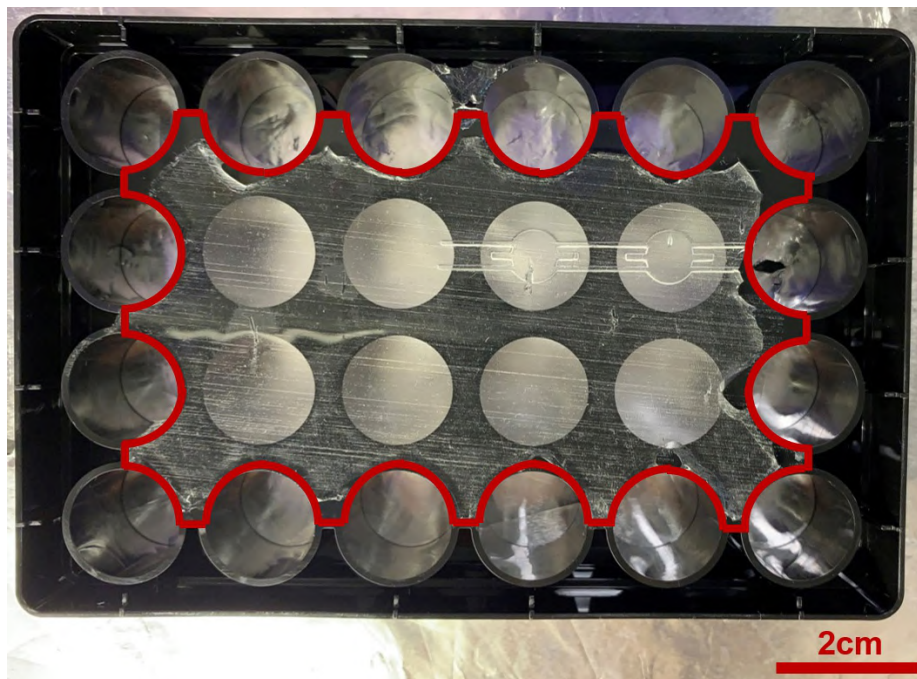
Figure 4-11: Peeling off test performed to assess the reliability of the bonding method.
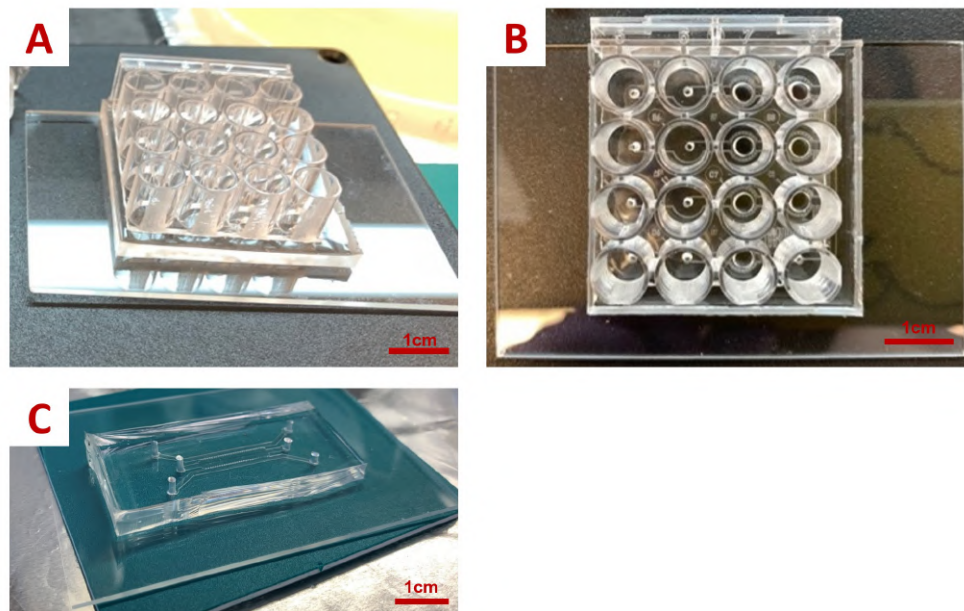
Figure 4-12: A) Side view and B) Top view of our fabricated multilayer device using the bonding method described here . C) Image of the device used in section 4.3.1 and 4.3.2.

We are also able to further bond the polystyrene-PDMS assembly on another substrate (here a glass slide is shown in panel A and B of Figure 4-12) using plasma bonding). We used 1/6 of one wellplate here and this is exactly the simulation unit in Chapter 2 and it also represents partially of our proposed device (except the lid and the media reservoir). As a contrast, in panel C, we also showed our current way of achieving vasculogenesis and EC lining. Moving from C to a fully working A/B still requires a considerable amount of efforts such as realizing the reliable sealing of the open top, designing ease-of-use perfusion system. But it will be a promising system which will make it easy to instantiate and assay a multicellular model.

4.4 Conclusions

We have made initial efforts towards our proposed system. The work discussed in this chapter is mainly 2 parts. First of all, we did a vasculogenesis assay using a traditional enclosed microfluidic device and tested tested two different seeding concentrations. They yielded distinct results, of which the high seeding density showed the expected

vasculature network formation. This will guide us to decide a proper cell concentration when we have more complex cell/tissue culture. Utilizing a traditional low-throughput device, we also tested other elements such as realizing a 2D lining in a microfluidic channel and perfuse the monolayer channel with a low shear stress while the 3D culture is present. Secondly, we successfully fabricated a hybrid device which is composed of a thermoplastics wellplate and a PDMS layer, which can be further bonded with another substrate. The bonding method described here is quick, although it requires more steps compared with direct plasma bonding. We will keep using/optimizing this binding strategy while we are testing and adding other key elements as proposed in Chapter 1. We aim to eventually translate all the protocol/knowledge learned from all these preliminary experiments to our proposed system so these are integral parts of the whole project.

Chapter 5

Conclusions and Future Directions

In this thesis, we proposed a system which allows for ease-of-use when instantiating the culture and analyzing the samples at the end-point, while maintaining the high physiological relevance it can model. We first performed finite element analysis to get a comprehensive understanding of the important physical/biochemical fields in the platform and then experimentally validated one key aspect of the modeling work. To demonstrate the feasibility of the platform, we also performed initial vasculogenesis study and device fabrication study. In this chapter, we discuss the improvement that could be made to the current work and envision future endeavor to realize the open-well system for engineering the blood-brain-barrier.

5.1 Transport and biochemical reactions regulate VEGF gradient in the microenvironment

For the purpose of designing the channel dimensions for our proposed device, to begin with, we visualized the velocity field in our media channel through simulation as it helps us estimate the amount of media needed when setting up the perfusion experiment. In addition, it will also be utilized to estimate the interstitial flow field across each culture unit in our system. Besides, we also get the pressure distribution information in the system, as that is a parameter that we can control and tune exter-

nally to a desired state. Although we encountered some problems such as severe back flow and nonuniform pressure driven force for the cell culture units at the beginning, they were solved by tuning the channel dimensions in the device. In addition, we also identified various plausible combinations of channel dimensions which could help eliminate the backflow and pressure inconsistency problems.

The original 3D culture unit was designed to be circular (to conform to the open shape of a single well) with a characteristic length of 5mm, we observed non-ideal VEGF penetration (of the 3D culture region) time dynamics therefore we switched to another optimized oval geometry for simulation and for later experimental validation. When we only give consideration to convection and diffusion, the optimized geometry should reach a linear VEGF gradient within 12 h, which is considered to be a critical signal for the sprout formation of endothelial cells [55].

The proposed system allows facile introduction of chemical stimulus to the 3D culture. It also allows flexibility in 3D cell-embedded gel culture as well as perfusion. This is typical in microfluidic OOC systems—there are a wide range of engineered parameters. One key point we illustrated in this work is that, these manually introduced factors 17 could have interactions which would have a large deviation from the 'intuition' hypothesis. If that's a vital signal, it could have a large impact on the experimental outcome. Specifically, in our case, VEGF is a critical signal in vasculogenesis and angiogenesis. A linear VEGF gradient can be directly assumed if only physical reactions are considered. Nonetheless, the applied VEGF could bind tightly to HSPG in the ECM. Even for the dominant form—VEGF165, which doesn't bind as strongly as VEGF189, a much longer time window (48 h) is needed for VEGF165 to reach a linear profile compared with the result from transport-only model (12 h). Moreover, it's also likely the externally-provided physical force could change the degree of biochemical chemical reactions spatially as it could redistribute the reactants. To be specific, the impact of proteases transported by interstitial flow was discussed through simulation in this thesis. For a physiological proteases digestion reaction rate, it could change the local VEGF concentration as much as 20%.

HSPG binds with a variety types of proteins [106]. In a wider context, many

biochemical reactions, for instance, enzyme degradation and hydrolysis, happen in extracellular environment ubiquitously. Depending on the specific problem under investigation, careful examining how the engineered factors could interact, how these factors would affect the cell/tissues is an indispensable step for the initial stage of the microfluidic OOC platform development. It guides the device design, it helps form unbiased hypothesis and aids in the analysis of the experiment results.

5.2 Experimental proof that matrix-binding could greatly alter VEGF distribution

We chose to verify one prominent aspect in our modeling—the altered VEGF distribution caused by HSPG binding. Three cases: 1) No binding, only transport by diffusion and convection 2) Very strong ECM binding 3) Binding domain removed were investigated in the experiment and the trend from our experiment is consistent with the simulation (Figure 3-19), although the quantitative value from the simulation may not be predictive since the simulation is always set at an ideal condition which is hard to implement in reality. Specifically, under case 3), the gradient profile is not the same as case 1) and we speculate that this is due to the HSPG not being completely digested. Given that the HSPG concentration is much higher than VEGF concentration typically used in an *in vitro* assay (the median effective dose of the VEGF protein is usually at ng/mL while the HSPG concentration could be at the order of ug/mL), it is important to evaluate whether the VEGF could reach the desired dose in the HSPG-containing ECM.

As we will keep using our simulation model to perform optimization work for device design, the work here absolutely builds our confidence on continue using our simulation model. Besides, the experiment result again reminds us that using non-binding canonical molecules of similar molecular weight might not be accurate in predicting the concentration profile of the target protein as it ignores the unique biochemical properties of the target protein. In a broader sense, it also teaches us

we should engineer the OOC systems properly—not only focus on the high-level functionality, analyzing and understanding the role of every small factor and their interactions is also indispensable and would be worthwhile for the overall system development.

5.3   Future work towards our proposed system

The initial vasculogenesis assay utilizing the self-assembly ability of brain EC was demonstrated in this thesis. We explored 2 distinct seeding concentrations with the higher one achieved the interconnected network structure. We believe the learning from this assay (seeding concentration, surface coating strategy, cell maintenance etc.), which was done in an enclosed system, could be translated directly to the open-well system once it becomes functional. We also realized that more characterization work needs to be done to the formed capillary network here. So far, we are mainly monitor the vasculogenesis process via phase contrast imaging. More stringent assays such as permeability measurement assay, tight junctions staining, and BEC-specific transporter expression will be performed in the future to validate the barrier properties of the capillaries formed in the microfluidic device.

The molecular permeability measurement assay requires direct perfusion to the 3D vascular network, which relies on the anastomosis between the EC lining in the perfusion channel and the 3D EC network. Although we observed the trend for anastomosis in our experiment (cell migration at the interface as shown in Figure 4-7), there is a lot of optimization work to do to form a tight connection at the interface. But it can be anticipated that, if the capillary network formed in the 3D culture region is intact without appreciable leakage and if the capillary network also anastomoses with the monolayer ECs in the perfusion channels, this tissue construct could enable a wide range of studies. For instance, besides assessing BBB permeability level to the specific molecule, it could also serve as a physiologic barrier to deliver nutrients/chemical cues to other cells/tissues cocultured in the 3D scaffold as well as being used in disease models for screening drugs that can cross the BBB.

It is also worth mentioning that in our future vasculogenesis/anastomosis assay, we should always note if there is any spatially-heterogeneous vessel morphology and density. On one hand, this is the lesson from our chapter 2) that VEGF may not penetrate the whole device for the first 24h unless the non-binding VEGF isoform is used. On the other hand, VEGF promotes tip cells sprouting towards the positive VEGF gradient direction [55]. To achieve the tight connection at the interface, ECs on both sides have to move in the opposite directions, which means we might need to reverse the VEGF gradient if necessary. One earlier worked have used the bidirectional VEGF gradient stimulation strategy to form tight EC connection at the communication pores [107].

Our initial device fabrication has proved that the chemical-assisted bonding can be both quick and reliable. The remaining two layers (the releasable lid and the media reservoir) remain to be fabricated and tested. By having the simulation model and initial experimental exploration in two critical aspects separately, we believe the direction of our next-stage work for developing the platform is clear. After we have the device prototype, we will first technically validate the device by demonstrating its ability to stably and independently perfuse the individual units. We will perform gel loading (just with cell lines) experiments using multichannel pipettes and carefully record the success rate of gel pinning and as well as the long-term (2 week) culture. We will eventually incorporate the vasculogenesis assay in the open-well system, starting by culture iPSC-BEC in the platform in a high-throughput manner and then place iPSC-derived BEC, pericytes and astrocytes into the hydrogel scaffold to create a dynamic BBB model *in vitro*. Importantly, we will also promote the usage of our platform by biological researchers who have zero experience in the microfluidic field and keep improving the system towards easy operation and high reproducibility.

5.4   Contributions

Microfluidic OOC technology has great potential for advancing the study of tissue development, organ physiology, disease pathology as well as drug discovery [8].]. How-

ever, this technology has yet to overcome many technical challenges, which hinder its adoption beyond the traditional engineering community. The system proposed in this thesis is aimed at solving one preeminent technical challenge—the complex operation (typically during sample loading and flow initiation), which results in low-throughput workflow, lack of reproducibility and unfriendliness to non-experts. The simulation model developed here allows us to optimize the device design and predict the distribution of the critical VEGF signal. The experimental validation work presents a simple but effective way to visualize the VEGF profile. Both the simulation and the experimental methodology is applicable to many OOC systems in which the engineered mechanical and chemical stimuli are critical for the desired cellular response. It might be also beneficial to expand the scope of the simulation, for instance, by incorporating more cellular responses such as receptor activation and internalization, considering a more complex ECM environment such as the existence of the soluble inhibitors depending on the problems under investigation. As we have illustrated through our simulation and the validation work, the fundamental notion is still to form unbiased hypothesis when engineering OOC systems by having a comprehensive understanding of the complex interactions in the whole platform.

The initial experimental work performed in this thesis proves feasibility of the proposed system, with a few elements remain to be constructed. The simple bonding strategy used in our preliminary experiments could potentially be applied to bond PDMS with other thermoplastic material, therefore it provides flexibility in our material choices when we further optimize the system. Our preliminary experimental work, both technically and biologically, will be combined once we have the open-well device prototype. We will leverage the robustness and ease-of-access of the system to recreate an in vitro model of BBB or even more sophisticated vascularized models. We are also greatly excited by the prospect of easy adoption of the platform by biological researchers as we believe a technology will have its largest impact once it becomes robust, reproducible, and readily accessible to the individual investigator in various research fields.

Bibliography

[1] Maoz, B. M. *et al.* A linked organ-on-chip model of the human neurovascular unit reveals the metabolic coupling of endothelial and neuronal cells. *Nature Biotechnology* **36**, 865–874 (2018).

[2] Shin, Y. *et al.* Blood-Brain Barrier Dysfunction in a 3D In Vitro Model of Alzheimer's Disease. *Advanced Science* **6** (2019).

[3] Esch, M. B. *et al.* Multi-cellular 3D human primary liver cell culture elevates metabolic activity under fluidic flow. *Lab on a Chip* **15**, 2269–2277 (2015).

[4] Jang, K. J. *et al.* Human kidney proximal tubule-on-a-chip for drug transport and nephrotoxicity assessment. *Integrative Biology* **5**, 1119–1129 (2013).

[5] Kim, H. J., Huh, D., Hamilton, G. & Ingber, D. E. Human gut-on-a-chip inhabited by microbial flora that experiences intestinal peristalsis-like motions and flow. *Lab Chip* **12**, 2165–2174 (2012).

[6] Falanga, A. P. *et al.* Shuttle-mediated nanoparticle transport across an in vitro brain endothelium under flow conditions. *Biotechnology and Bioengineering* **114**, 1087–1095 (2017).

[7] Shin, Y. *et al.* In vitro 3D collective sprouting angiogenesis under orchestrated ANG-1 and VEGF gradients. *Lab on a Chip* **11**, 2175–2181 (2011).

[8] Bhatia, S. N. & Ingber, D. E. Microfluidic organs-on-chips. *Nature Biotechnology* **32**, 760–772 (2014).

[9] Deosarkar, S. P. *et al.* A Novel Dynamic Neonatal Blood-Brain Barrier on a Chip. *PLOS ONE* **10**, e0142725 (2015).

[10] Kim, S., Chung, M., Ahn, J., Lee, S. & Jeon, N. L. Interstitial flow regulates the angiogenic response and phenotype of endothelial cells in a 3D culture model. *Lab on a Chip* **16**, 4189–4199 (2016).

[11] Miller, J. S. *et al.* Rapid casting of patterned vascular networks for perfusable engineered three-dimensional tissues. *Nature Materials* **11**, 768–774 (2012).

[12] Prabhakarpandian, B. *et al.* SyM-BBB: a microfluidic blood brain barrier model. *Lab on a Chip* **13**, 1093–1101 (2013).

[13] Huh, D. *et al.* Reconstituting Organ-Level Lung Functions on a Chip. *Science* **328**, 1662–1668 (2010).

[14] Zervantonakis, I. K. *et al.* Three-dimensional microfluidic model for tumor cell intravasation and endothelial barrier function. *Proc. Natl. Acad. Sci. U.S.A.* **109**, 13515–13520 (2012).

[15] Miller, P. G., Chen, C. Y., Wang, Y. I., Gao, E. & Shuler, M. L. Multiorgan microfluidic platform with breathable lung chamber for inhalation or intravenous drug screening and development. *Biotechnol Bioeng* **117**, 486–497 (2020).

[16] Herland, A. *et al.* Quantitative prediction of human pharmacokinetic responses to drugs via fluidically coupled vascularized organ chips. *Nature Biomedical Engineering* 1–16 (2020).

[17] Novak, R. *et al.* Robotic fluidic coupling and interrogation of multiple vascularized organ chips. *Nature Biomedical Engineering* 1–14 (2020).

[18] Probst, C., Schneider, S. & Loskill, P. High-throughput organ-on-a-chip systems: Current status and remaining challenges. *Current Opinion in Biomedical Engineering* **6**, 33–41 (2018).

[19] Liu, L. *et al.* Three-dimensional brain-on-chip model using human iPSC-derived GABAergic neurons and astrocytes: Butyrylcholinesterase post-treatment for acute malathion exposure. *PLoS One* **15** (2020).

[20] Petrosyan, A. *et al.* A glomerulus-on-a-chip to recapitulate the human glomerular filtration barrier. *Nat. Commun.* **10**, 1–17 (2019).

[21] Phan, D. T. T. *et al.* A vascularized and perfused organ-on-a-chip platform for large-scale drug screening applications. *Lab on a Chip* **17**, 511–520 (2017).

[22] Tan, K. *et al.* A high-throughput microfluidic microphysiological system (PREDICT-96) to recapitulate hepatocyte function in dynamic, re-circulating flow conditions. *Lab on a Chip* **19**, 1556–1566 (2019).

[23] van Duinen, V. *et al.* Robust and Scalable Angiogenesis Assay of Perfused 3D Human iPSC-Derived Endothelium for Anti-Angiogenic Drug Screening. *Int. J. Mol. Sci.* **21**, 4804 (2020).

[24] Berry, S. B. *et al.* Upgrading well plates using open microfluidic patterning. *Lab on a Chip* **17**, 4253–4264 (2017).

[25] Berthier, E., Dostie, A. M., Lee, U. N., Berthier, J. & Theberge, A. B. Open Microfluidic Capillary Systems. *Anal. Chem.* **91**, 8739–8750 (2019).

[26] Zhang, B., Korolj, A., Lai, B. F. L. & Radisic, M. Advances in organ-on-a-chip engineering. *Nature Reviews Materials* **3**, 257–278 (2018).

[27] Yu, Y. J. *et al.* Hydrogel-incorporating unit in a well: 3D cell culture for high-throughput analysis. *Lab on a Chip* **18**, 2604–2613 (2018).

[28] Park, D. *et al.* High-Throughput Microfluidic 3D Cytotoxicity Assay for Cancer Immunotherapy (CACI-IMPACT Platform). *Frontiers in Immunology* **10** (2019).

[29] Feigin, V. L. *et al.* Global, regional, and national burden of neurological disorders, 1990–2016: a systematic analysis for the Global Burden of Disease Study 2016. *The Lancet Neurology* **18**, 459–480 (2019).

[30] Kinch, M. S. An analysis of FDA-approved drugs for neurological disorders. *Drug Discovery Today* **20**, 1040–1043 (2015).

[31] Banks, W. A. From blood–brain barrier to blood–brain interface: new opportunities for CNS drug delivery. *Nature Reviews Drug Discovery* **15**, 275–292 (2016).

[32] Chow, B. W. & Gu, C. The Molecular Constituents of the Blood–Brain Barrier. *Trends in Neurosciences* **38**, 598–608 (2015).

[33] Nation, D. A. *et al.* Blood–brain barrier breakdown is an early biomarker of human cognitive dysfunction. *Nature Medicine* **25**, 270–276 (2019).

[34] Murphy, M. P. & Harry Levine, I. Alzheimer's Disease and the β-Amyloid Peptide. *Journal of Alzheimer's disease : JAD* **19**, 311 (2010).

[35] Drummond, E. & Wisniewski, T. Alzheimer's Disease: Experimental Models and Reality. *Acta neuropathologica* **133**, 155–175 (2017).

[36] Esch, M., King, T. & Shuler, M. The Role of Body-on-a-Chip Devices in Drug and Toxicity Studies. *Annual Review of Biomedical Engineering* **13**, 55–72 (2011).

[37] Stone, N. L., England, T. J. & O'Sullivan, S. E. A Novel Transwell Blood Brain Barrier Model Using Primary Human Cells. *Front. Cell. Neurosci.* **13** (2019).

[38] Hatherell, K., Couraud, P.-O., Romero, I. A., Weksler, B. & Pilkington, G. J. Development of a three-dimensional, all-human in vitro model of the blood-brain barrier using mono-, co-, and tri-cultivation Transwell models. *J. Neurosci. Methods* **199** (2011).

[39] Siddharthan, V., Kim, Y. V., Liu, S. & Kim, K. S. Human astrocytes/astrocyte-conditioned medium and shear stress enhance the barrier properties of human brain microvascular endothelial cells. *Brain research* **1147**, 39–50 (2007).

[40] Griep, L. M. *et al.* BBB on chip: microfluidic platform to mechanically and biochemically modulate blood-brain barrier function. *Biomedical Microdevices* **15**, 145–150 (2013).

[41] Cucullo, L. *et al.* Immortalized human brain endothelial cells and flow-based vascular modeling: a marriage of convenience for rational neurovascular studies. *Journal of cerebral blood flow & metabolism* **28**, 312–328 (2008).

[42] Chen, S., Einspanier, R. & Schoen, J. Transepithelial electrical resistance (TEER): a functional parameter to monitor the quality of oviduct epithelial cells cultured on filter supports. *Histochem. Cell Biol.* **144**, 509 (2015).

[43] Park, T.-E. *et al.* Hypoxia-enhanced Blood-Brain Barrier Chip recapitulates human barrier function and shuttling of drugs and antibodies. *Nature Communications* **10** (2019).

[44] Booth, R. & Kim, H. Characterization of a microfluidic in vitro model of the blood-brain barrier (BBB). *Lab on a Chip* **12**, 1784–1792 (2012).

[45] Adriani, G., Ma, D., Pavesi, A., Kamm, R. D. & Goh, E. L. K. A 3D neurovascular microfluidic model consisting of neurons, astrocytes and cerebral endothelial cells as a blood–brain barrier. *Lab on a Chip* **17**, 448–459 (2017).

[46] Herland, A. *et al.* Distinct Contributions of Astrocytes and Pericytes to Neuroinflammation Identified in a 3D Human Blood-Brain Barrier on a Chip. *PLOS ONE* **11**, e0150360 (2016).

[47] Campisi, M. *et al.* 3D self-organized microvascular model of the human blood-brain barrier with endothelial cells, pericytes and astrocytes. *Biomaterials* **180**, 117–129 (2018).

[48] Wevers, N. R. *et al.* A perfused human blood–brain barrier on-a-chip for high-throughput assessment of barrier function and antibody transport. *Fluids and Barriers of the CNS* **15** (2018).

[49] Lee, S., Chung, M., Lee, S. R. & Jeon, N. L. 3D brain angiogenesis model to reconstitute functional human blood-brain barrier in vitro. *Biotechnology and Bioengineering* (2019).

[50] Lee, Y. *et al.* Microfluidics within a well: an injection-molded plastic array 3D culture platform. *Lab on a Chip* **18**, 2433–2440 (2018).

[51] Moya, M. L., Hsu, Y.-H., Lee, A. P., Hughes, C. C. & George, S. C. *In Vitro* Perfused Human Capillary Networks. *Tissue Engineering Part C: Methods* **19**, 730–737 (2013).

[52] Wang, Y. I., Abaci, H. E. & Shuler, M. L. Microfluidic blood–brain barrier model provides in vivo-like barrier properties for drug permeability screening. *Biotechnology and Bioengineering* **114**, 184–194 (2017).

[53] Wang, X. L. *et al.* A hydrostatic pressure-driven passive micropump enhanced with siphon-based autofill function. *Lab on a Chip* **18**, 2167–2177 (2018).

[54] Gattazzo, F., Urciuolo, A. & Bonaldo, P. Extracellular matrix: A dynamic microenvironment for stem cell niche. *Biochim. Biophys. Acta* **1840**, 2506 (2014).

[55] Geudens, I. & Gerhardt, H. Coordinating cell behaviour during blood vessel formation. *Development* **138** (2011).

[56] Whitaker, S. Flow in porous media i: A theoretical derivation of darcy's law. *Transport in porous media* **1**, 3–25 (1986).

[57] Durlofsky, L. & Brady, J. F. Analysis of the Brinkman equation as a model for flow in porous media. *Phys. Fluids* **30**, 3329–3341 (1987).

[58] Le Bars, M. & Worster, M. G. Interfacial conditions between a pure fluid and a porous medium: implications for binary alloy solidification. *J. Fluid Mech.* **550**, 149–173 (2006).

[59] COMSOL Multiphysics Application Library. Forchheimer flow (2019). [Online]. `https://www.comsol.com/model/download/656391/models.porous.forchheimer_flow.pdf`. [Accessed 5. Aug. 2020].

[60] Amiri, A. & Vafai, K. Transient analysis of incompressible flow through a packed bed. *Int. J. Heat Mass Transfer* **41**, 4259–4279 (1998).

[61] Ferrara, N., Gerber, H.-P. & LeCouter, J. The biology of VEGF and its receptors. *Nature Medicine* **9**, 669–676 (2003).

[62] Harper, S. J. & Bates, D. O. VEGF-A splicing: the key to anti-angiogenic therapeutics? *Nature Reviews Cancer* **8**, 880–887 (2008).

[63] Shamloo, A. & Heilshorn, S. C. Matrix density mediates polarization and lumen formation of endothelial sprouts in VEGF gradients. *Lab on a Chip* **10**, 3061–3068 (2010).

[64] Jeong, G. S. *et al.* Sprouting angiogenesis under a chemical gradient regulated by interactions with an endothelial monolayer in a microfluidic platform. *Anal. Chem.* **83**, 8454–8459 (2011).

[65] Ellis, L. M. & Hicklin, D. J. VEGF-targeted therapy: mechanisms of anti-tumour activity. *Nat. Rev. Cancer* **8**, 579–591 (2008).

[66] Peach, C. J. *et al.* Molecular Pharmacology of VEGF-A Isoforms: Binding and Signalling at VEGFR2. *International Journal of Molecular Sciences* **19**, 1264 (2018).

[67] Ferrara, N. Vascular Endothelial Growth Factor: Basic Science and Clinical Progress. *Endocrine Reviews* **25**, 581–611 (2004).

[68] Houck, K. A., Leung, D. W., Rowland, A. M., Winer, J. & Ferrara, N. Dual regulation of vascular endothelial growth factor bioavailability by genetic and proteolytic mechanisms. *Journal of Biological Chemistry* **267**, 26031–26037 (1992).

[69] Vempati, P., Popel, A. S. & Mac Gabhann, F. Extracellular regulation of VEGF: Isoforms, proteolysis, and vascular patterning. *Cytokine & Growth Factor Reviews* **25**, 1–19 (2014).

[70] Vempati, P., Popel, A. S. & Mac Gabhann, F. Formation of VEGF isoform-specific spatial distributions governing angiogenesis: computational analysis. *BMC Systems Biology* **5**, 59 (2011).

[71] Lee, S., Jilani, S. M., Nikolova, G. V., Carpizo, D. & Iruela-Arispe, M. L. Processing of VEGF-A by matrix metalloproteinases regulates bioavailability and vascular patterning in tumors. *The Journal of Cell Biology* **169**, 681–691 (2005).

[72] Helm, C.-L. E., Fleury, M. E., Zisch, A. H., Boschetti, F. & Swartz, M. A. Synergy between interstitial flow and VEGF directs capillary morphogenesis in vitro through a gradient amplification mechanism. *Proceedings of the National Academy of Sciences* **102**, 15779–15784 (2005).

[73] Song, J. W. & Munn, L. L. Fluid forces control endothelial sprouting. *Proceedings of the National Academy of Sciences* **108**, 15342–15347 (2011).

[74] Jackson, G. W. & James, D. F. The permeability of fibrous porous media. *Can. J. Chem. Eng.* **64**, 364–374 (1986).

[75] McCarty, W. J. & Johnson, M. The Hydraulic Conductivity of Matrigel^{TM}. *Biorheology* **44**, 303–317 (2007).

[76] Happel, J. Viscous flow relative to arrays of cylinders. *AIChE Journal* **5**, 174–177 (1959).

[77] Paulsson, M. *et al.* Purification and structural characterization of intact and fragmented nidogen obtained from a tumor basement membrane. *Eur. J. Biochem.* **156**, 467–478 (1986).

[78] Corning Life Sciences. Corning Matrigel® matrix FAQ. [Online]. `https://www.corning.com/catalog/cls/documents/faqs/CLS-DL-CC-026.pdf`. [Accessed: 5 Aug. 2020].

[79] Fischer, H., Polikarpov, I. & Craievich, A. F. Average protein density is a molecular-weight-dependent function. *Protein Sci.* **13**, 2825 (2004).

[80] Zaman, M. H. *et al.* Migration of tumor cells in 3D matrices is governed by matrix stiffness along with cell-matrix adhesion and proteolysis. *Proc. Natl. Acad. Sci. U.S.A.* **103**, 10889–10894 (2006).

[81] Lam, N. T., Lam, H., Sturdivant, N. M. & Balachandran, K. Fabrication of a matrigel–collagen semi-interpenetrating scaffold for use in dynamic valve interstitial cell culture. *Biomedical Materials* **12**, 045013 (2017).

[82] Anguiano, M. *et al.* Characterization of three-dimensional cancer cell migration in mixed collagen-Matrigel scaffolds using microfluidics and image analysis. *PLoS One* **12**, e0171417 (2017).

[83] Vempati, P., Mac Gabhann, F. & Popel, A. S. Quantifying the Proteolytic Release of Extracellular Matrix-Sequestered VEGF with a Computational Model. *PLoS ONE* **5** (2010).

[84] Park, J. E., Keller, G. A. & Ferrara, N. The vascular endothelial growth factor (VEGF) isoforms: differential deposition into the subepithelial extracellular matrix and bioactivity of extracellular matrix-bound VEGF. *Mol. Biol. Cell* (2017).

[85] Ferrara, N. Binding to the Extracellular Matrix and Proteolytic Processing: Two Key Mechanisms Regulating Vascular Endothelial Growth Factor Action. *Molecular Biology of the Cell* **21**, 687–690 (2010).

[86] Robinson, C. J. & Stringer, S. E. The splice variants of vascular endothelial growth factor (VEGF) and their receptors. *J. Cell Sci.* **114**, 853–865 (2001).

[87] Spence, M. T. Z. & Johnson, I. D. The molecular probes handbook : a guide to fluorescent probes and labeling technologies. *Live Technologies Corporation* (2010).

[88] Grabarek, Z. & Gergely, J. Zero-length crosslinking procedure with the use of active esters. *Anal. Biochem.* **185**, 131–135 (1990).

[89] Lee, T.-Y., Folkman, J. & Javaherian, K. HSPG-Binding Peptide Corresponding to the Exon 6a-Encoded Domain of VEGF Inhibits Tumor Growth by Blocking Angiogenesis in Murine Model. *PLoS ONE* **5** (2010).

[90] Chiodelli, P. *et al.* Heparan Sulfate Proteoglycans Mediate the Angiogenic Activity of the Vascular Endothelial Growth Factor Receptor-2 Agonist Gremlin. *Arterioscler., Thromb., Vasc. Biol.* (2011).

[91] Goerges, A. L. & Nugent, M. A. Regulation of vascular endothelial growth factor binding and activity by extracellular pH. *J. Biol. Chem.* **278**, 19518–19525 (2003).

[92] Condomitti, G. & de Wit, J. Heparan Sulfate Proteoglycans as Emerging Players in Synaptic Specificity. *Front. Mol. Neurosci.* **11** (2018).

[93] Wikipedia contributors. Perlecan (2020). [Online]. `https://en.wikipedia.org/w/index.php?title=Perlecan&oldid=945711781`. [Accessed 25. Jul. 2020].

[94] Patel, V. N. *et al.* Heparanase cleavage of perlecan heparan sulfate modulates FGF10 activity during ex vivo submandibular gland branching morphogenesis. *Development* **134**, 4177–4186 (2007).

[95] Whitelock, J. M., Melrose, J. & Iozzo, R. V. Diverse Cell Signaling Events Modulated by Perlecan. *Biochemistry* **47**, 11174–11183 (2008).

[96] Zoeller, J. J., Whitelock, J. M. & Iozzo, R. V. Perlecan regulates developmental angiogenesis by modulating the VEGF-VEGFR2 axis. *Matrix Biology: Journal of the International Society for Matrix Biology* **28**, 284–291 (2009).

[97] Muthusamy, A., Cooper, C. R. & Gomes, R. R., Jr. Soluble perlecan domain i enhances vascular endothelial growth factor-165 activity and receptor phosphorylation in human bone marrow endothelial cells. *BMC Biochem.* **11**, 43 (2010).

[98] Sigma-Aldrich. Key resources: Carbohydrate analysis, enzyme explorer (2020). [Online]. `https://www.sigmaaldrich.com/life-science/metabolomics/enzyme-explorer/learning-center/carbohydrate-analysis/carbohydrate-analysis-iii.html`. [Accessed 25. Jul. 2020].

[99] LeBrun, L. A. & Linhardt, R. J. Degradation of Heparan Sulfate with Heparin Lyases. *Proteoglycan Protocols* 353–361 (2001).

[100] Lohse, D. L. & Linhardt, R. J. Purification and characterization of heparin lyases from Flavobacterium heparinum. *J. Biol. Chem.* **267**, 24347–24355 (1992).

[101] Biotin binding proteins (2020). [Online]. `https://www.abcam.com/index.html?pageconfig=resource&rid=12723`. [Accessed 28. Jul. 2020].

[102] Gill, S. C. & von Hippel, P. H. Calculation of protein extinction coefficients from amino acid sequence data. *Anal. Biochem.* **182**, 319–326 (1989).

[103] Vascular endothelial growth factor [homo sapiens] - protein - NCBI (2020). [Online]. `https://www.ncbi.nlm.nih.gov/protein/AAA36804`. [Accessed 28. Jul. 2020].

[104] Huang, C. P. *et al.* Engineering microscale cellular niches for three-dimensional multicellular co-cultures. *Lab on a Chip* **9**, 1740–1748 (2009).

[105] Bodas, D. & Khan-Malek, C. Hydrophilization and hydrophobic recovery of PDMS by oxygen plasma and chemical treatment—An SEM investigation. *Sens. Actuators, B* **123**, 368–373 (2007).

[106] Whitelock, J. M., Melrose, J. & Iozzo, R. V. Diverse Cell Signaling Events Modulated by Perlecan. *Biochemistry* **47**, 11174–11183 (2008).

[107] Wang, X. *et al.* Engineering anastomosis between living capillary networks and endothelial cell-lined microfluidic channels. *Lab on a Chip* **16**, 282–290 (2016).

[108] Lenard, A. *et al.* In Vivo Analysis Reveals a Highly Stereotypic Morphogenetic Pathway of Vascular Anastomosis. *Dev. Cell* **25**, 492–506 (2013).

[109] Paek, J. *et al.* Microphysiological Engineering of Self-Assembled and Perfusable Microvascular Beds for the Production of Vascularized Three-Dimensional Human Microtissues. *ACS Nano* **13**, 7627–7643 (2019).

[110] Diaz-Santana, A., Shan, M. & Stroock, A. D. Endothelial cell dynamics during anastomosis in vitro. *Integr. Biol. (Camb).* **7**, 454–466 (2015).

[111] Sunkara, V. *et al.* Simple room temperature bonding of thermoplastics and poly(dimethylsiloxane). *Lab on a Chip* **11**, 962–965 (2011).

[112] Suzuki, Y., Yamada, M. & Seki, M. Sol–gel based fabrication of hybrid microfluidic devices composed of PDMS and thermoplastic substrates. *Sens. Actuators, B* **148**, 323–329 (2010).

[113] Sivakumar, R., Trinh, K. T. L. & Lee, N. Y. Heat and pressure-resistant room temperature irreversible sealing of hybrid PDMS–thermoplastic microfluidic devices via carbon–nitrogen covalent bonding and its application in a continuous-flow polymerase chain reaction. *RSC Adv.* **10**, 16502–16509 (2020).

[114] Wu, W., Wu, J., Kim, J.-H. & Lee, N. Y. Instantaneous room temperature bonding of a wide range of non-silicon substrates with poly(dimethylsiloxane) (PDMS) elastomer mediated by a mercaptosilane. *Lab on a Chip* **15**, 2819–2825 (2015).

[115] Sunkara, V. & Cho, Y.-K. Investigation on the Mechanism of Aminosilane-Mediated Bonding of Thermoplastics and Poly(dimethylsiloxane). *ACS Applied Materials & Interfaces* **4**, 6537–6544 (2012).

[116] Xie, Y., Hill, C. A. S., Xiao, Z., Militz, H. & Mai, C. Silane coupling agents used for natural fiber/polymer composites: A review. *Composites Part A* **41**, 806–819 (2010).